ELECTRONIC NOISE STUDIES OF UNDERDOPED HIGH TEMPERATURE SUPERCONDUCTORS

BY

DAVID CAPLAN

B.Sc., University of British Columbia, 2002
M.S., University of Illinois at Urbana-Champaign, 2005
M.S., University of Illinois at Urbana-Champaign, 2007

DISSERTATION

Submitted in partial fulfillment of the requirements
for the degree of Doctor of Philosophy in Physics
in the Graduate College of the
University of Illinois at Urbana-Champaign, 2009

Urbana, Illinois

Doctoral Committee:

Professor Michael Weissman, Chair
Professor Dale Van Harlingen, Director of Research
Associate Professor Karin Dahmen
Professor David Hertzog

Abstract

We use electronic transport noise measurements in order to probe normal state properties of high temperature superconductors with the goal of providing further detail about the environment in which the necessary pairing of electrons occurs. We observe an unusual noise component near and below about 200 K in the normal state of underdoped YBCO and Ca-YBCO films. We use several experimental noise-transport techniques in order to elucidate dynamic, thermodynamic and symmetry properties of the underlying fluctuations that cause this excess noise. We have found that this region of noise displays many features, such as large fluctuators, aging effects and a complicated magnetic sensitivity, that one would expect for symmetry-breaking collective electronic state.

To my wife, Charmaine and son, Emmanuel.

Acknowledgments

The work presented in this thesis would not have been possible without the help and support from a number of people. I would first like to thank my collaborator Vladimir Orlyanchik, an excellent experimentalist and good friend from whom I learned much about experimental physics during my final year of graduate school. I leave the continuation of this project in competent hands and I wish him much success in his career as a scientist. The work in this thesis would not have been possible without the guidance of my advisor, Dale Van Harlingen; I greatly appreciate his insight, patience and support despite his trepidations of entering the morass of yet another noise experiment. Michael Weissman has been an invaluable source of help, both physical (for the use of his laboratory) and intellectual, throughout my graduate career. This work would not be possible without his expertise and sharp insight. I would also like to thank Jim Eckstein and Eduardo Fradkin for many fruitful discussions as well as Tom Lemberger for supplying several samples necessary for this research. Much of the fabrication work would not be possible without the technical support of Tony Banks.

I am grateful to the training that I received from Tony Bonetti when I first arrived in the DVH research group. I am also thankful for the help and support I received from other DVH group members, these include: Trevis Crane, Sergey Frolov, Francoise Kidwingira, Micah Stoutimore, Madalina Colci-O'Hara, Dan Bahr, Martin Stehno, Joel Strand and Juan Atkinson. I wish much success to the new graduate students Adam Weis and Chris Nugruho.

Finally, my deepest debt of gratitude is for my dear wife Charmaine Armitage-Caplan for her unconditional love and support.

This work was supported by the U.S. Department of Energy, Division of Materials Sciences, under grant DE-FG02-07ER46453.

Table of Contents

List of Figures

Chapter 1

Cuprate Superconductors

1.1 Introduction

In 1911, three years after he first liquified helium at 4.2K, the Dutch physicist Kamerlingh Onnes discovered a precipitous drop to zero resistivity in mercury [1] – the trademark feature of superconductivity. The second prominent feature of superconductivity, perfect diamagnetism (for relatively small magnetic fields) known as the Meissner effect, was not discovered until 1933 by Meissner and Oschenfeld [2]. The work of Bardeen, Cooper, and Schriefer in 1957 [3, 4], known as BCS theory, provided a thorough understanding of the macroscopic properties of superconductivity derived from a microscopic picture based on the pairing of electrons below T_c. The basic idea of BCS theory is that the electrons can form a collective state via the condensation of electron pairs, commonly referred to as Cooper pairs. The attractive potential necessary for overcoming Coulomb repulsion is due to coupling between the electrons and excitations in the lattice structure known as phonons.

The scientific community considered BCS theory an overwhelming success based on numerous verified theoretical predictions. Among these predictions, derived a decade after BCS and based on the electron-phonon coupling strength, was that superconductivity should not be possible above a maximum superconducting critical temperature of $T_{cMax} \approx 28K$ [5]. The suprise discovery in 1986, by Bednorz and Muller of a ceramic, transition metal oxide $La_{2-x}Ba_xCuO_4$ (LBCO), with a superconducting transition, T_c, above 30K [6] suggested that there may be a cause for

superconductivity not explained by BCS theory.

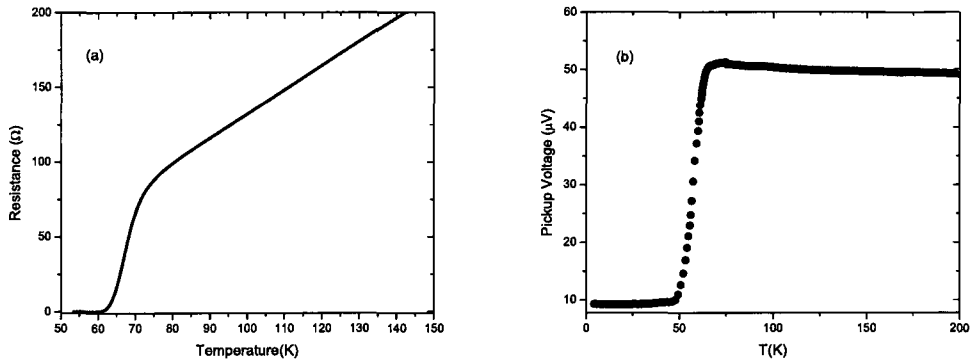

(a) (b)

Figure 1.1: (a) Resistance vs Temperature for a YBCO film demonstrating a transition to perfect conductivity at T_c. (b) Data from a two-coil measurement of T_c wherein a YBCO film is placed between a driving and a pick-up coil. At the superconducting transition the Meissner effect sets in drastically reducing the mutual inductance between the two coils.

LBCO belongs to a family of materials known as the cuprates. More of these high-T_c cuprates were discovered with T_c's well above the boiling temperature of liquid nitrogen. Similar to conventional superconductors, the high-temperature superconductors (HTSC) display both of the representative phenomena of superconductivity below T_c, perfect conductivity and the Meissner effect (examples of these are shown in Figure 1.1). Nevertheless, cuprates cannot be fully explained in a BCS framework and despite over 20 years of intensive research, a microscopic understanding of the mechanism behind high-T_c superconductivity remains one of the most elusive problems in condensed matter physics. Ultimately, the solution must come from incorporating the superconductivity as part of a unique and complex phase diagram. One of the major impediments to a full understanding of HTSC is a lack of experimental answers to several key questions regarding the phase diagram. This experimental techniques used in this thesis serve as an experimental probe of one of these complex parts of the

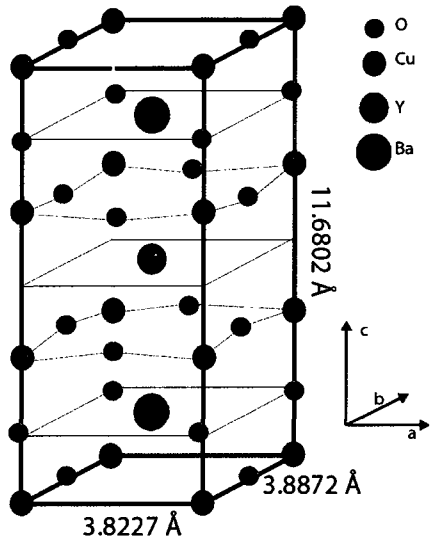

Figure 1.2: The basic crystalline structure of YBCO. The structure shown is for higher doping as evident by the orthorhombic symmetry and the oxygen ordering in Cu-O chains in the basal CuO_y planes, preferentially along the b axis.

cuprate phase diagram known as the pseudogap (PG) phase. The goal of this thesis is to use noise transport measurements to search for a relationship between previously unlinked experimental observations within the pseudogap phase and to give further detail about the environment in which the necessary pairing of electrons occurs. The rest of this chapter will introduce in more detail the properties of the cuprates and serve as background for the motivation of the research presented in this thesis.

1.2 Cuprate Structure

Unlike the single elements or simple compounds that compose the conventional superconductors, the cuprates belong to a class of complex layered structures categorized as perovskites. The term cuprate is the namesake of CuO_2 planes that are interjacent to layers of other various oxide building blocks. In the case of the materials studied in this thesis, Ca-YBCO and YBCO (see Fig. 1.2), there are two CuO_2 units per unit

cell alternating with layers of Y/Ca, Ba-O and the basal CuO_y planes. The CuO_y planes are where the most common type of doping, adding or removing oxygen, occurs. At little to no doping, the oxygen can be found in two locations in the CuO_y planes, in either the a or b crystal direction. For higher doping, these locations are not equivalent and the extra oxygen is preferably added along the crystallographic b axis forming Cu-O-Cu chains. The structure itself changes as the doping changes [7] (as seen in Fig. 1.3(a)). In $YBa_2Cu_3O_{7-\delta}$ with $\delta = 1$, the structure of YBCO is tetragonal (i.e. $a = b$) and there is no oxygen in the CuO_y planes. Initially, with added oxygen, there is no distinguishing between oxygen sites on the CuO_y planes, or the a and b lattice parameters. Eventually, when $\delta \sim 0.6$, there is a structural phase transition from tetragonal to orthorhombic with full oxygen doping occurring at $\delta = 0$. The transition between tetragonal and orthorhombic structure is the major source of a phenomenon known as twinning. At the high temperatures necessary to grow YBCO, the structure is tetragonal, however at low temperatures and higher doping, the material transitions to orthorhombic symmetry – the internal stresses cause the formation of twins boundaries [8]. In the case of YBCO, twinning involves a tweed-like pattern of alternating orientation in the (110) direction, between the a and b crystal axes. Figure 1.3 (b) shows the twinning of an $La_{2-x}Sr_xCuO_4$ (LSCO) crystal seen with a polarized light microscope. This twinning is common to both crystals and thin films of YBCO and macroscopic measurements averaged over both lattice directions. Growing twin-free crystals or thin films is difficult, however possible, yielding important experimental results such as measuring the anisotropy of the YBCO gap symmetry [9].

The layered aspect of the cuprates give rise to the quasi two-dimensional properties where the electronic behavior occurs in the CuO_2 planes. This 2-D property is evident in transport measurements where a large anisotropy exists in the resistivity between the a/b crystal directions (in the CuO_2 planes) and the c direction (perpendicular to

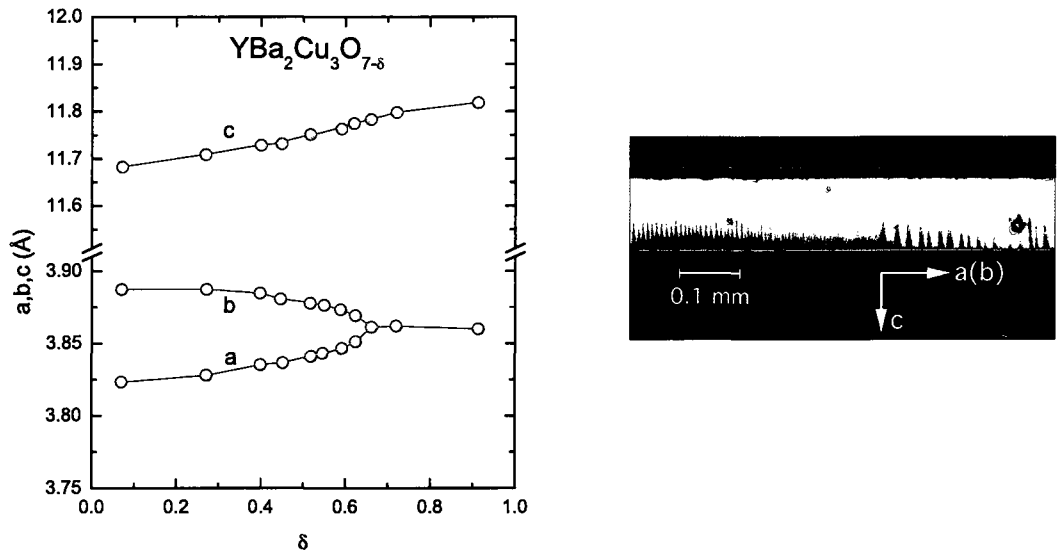

(a) (b)

Figure 1.3: (a) YBCO lattice parameters for different doping. (b) Twinning in an LSCO crystal observed with a polarized-light microscope.

the plane)[10].

1.3 Doping and the Phase Diagram

In order for the cuprates to become conducting or superconducting, they must be doped; specifically, the CuO_2 planes must be doped by changing the number of electronic carriers (see Fig. 1.4). Doping can be done by one of three ways: changing the oxygen content, by cation doping in which one cation is substituted for another, and by applying strain. In all cases, the doping serves to increase the density of electronic carriers. In this thesis, I focus on YBCO and Ca-YBCO which are doped via hole doping either by changing oxygen content or by cation doping where Ca is substituted for Y.

Before we go into more detail about doping, it is necessary to introduce the 'parent'

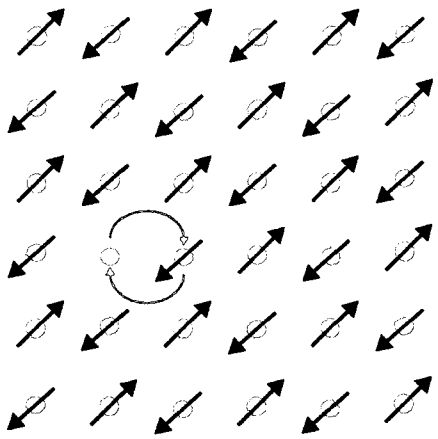

Figure 1.4: The effect of hole doping in the AF lattice. Electrons (blue dots) are free to hop in and out of vacancies (holes). The holes can be treated as charge carriers.

material of YBCO, $YBa_2Cu_3O_6$. With no added dopants, YBCO has one electron per Cu site and is classified as a Mott insulator. A Mott insulator is a material which should be metallic as predicted by standard band theory however is insulating due to strong electron-electron repulsion [11]. The material is also an antiferromagnet (AF) when undoped [12]. Antiferromagnetism occurs because it is energetically favorable in a Mott insulator; the system can gain energy if oppositely aligned electrons jump back and forth between neighboring sites in a process known as virtual hopping [13]. Most theories that deal with the cuprates begin with an AF Mott insulator [13, 14] and attempt to explain what happens when the doping is increased.

Oxygen Doping

Oxygen doping is the most common type of doping used in $YBa_2Cu_3O_{7-\delta}$ where $0 < \delta < 1$. When doping YBCO via oxygen, the added oxygen sit in the basal CuO_y planes and serve as charge reservoirs to the CuO_2 planes [15]. With added oxygen, YBCO eventually becomes underdoped at $\delta \sim 0.7$; it begins to conduct (poorly) in the 'normal' (i.e. non-superconducting) state and superconducts at very low temperatures. With low doping, the oxygen sits in the CuO_y planes with no

preference to the a or b lattice direction until $\delta \sim 0.6$ when this symmetry is broken and oxygen preferentially sits in Cu-O chains along the b axis. At $\delta \sim 0.05$, YBCO is optimally doped with a maximum T_c of 92K. It should be noted that adding excess oxygen puts YBCO into a non-stoichiometric state and the oxygen has the tendency to slowly diffuse out of the material via long range hopping. In thin films and wires of YBCO this effect can be exacerbated by the shorter length scales for oxygen to diffuse out of the system.

Cation Doping

In YBCO, cation doping can be done by one of three ways: substituting a Cu in the CuO_2 plane, substituting a Cu in the CuO chains or by replacing the Y^{3+} cation. In the case of Cu, they can be replaced with Zn (which sits in the CuO_2 planes) or Co, Fe or Al (which sit in the CuO_y planes / CuO chains) [16, 17]. In each case of replacing the Cu cations, the superconducting properties of the material decreases. The Y^{3+} cation can be replaced by either Ca^{2+} or $Pr^{4+,3+}$. Substituting Ca^{2+} for the trivalent Y has been shown to add extra holes to the CuO_2. Doping with Ca^{2+} along with oxygen can be advantageous since it can make the material more stable by precluding the diffusion of oxygen. Pr^{3+} substitution for Y^{3+} eventually suppresses superconductivity and the compound can become insulating.

The Phase Diagram

The phase diagram of the cuprates as a function of temperature and doping can be seen in Figure 1.5. Depending on the doping and temperature, the HTSC can be AF insulators, metal-like or superconductors. With very little doping, the AF insulating properties remain intact, even up to very high temperatures (> 400K). The dome shaped superconducting region of the phase diagram is common to all cuprate superconductors. The maximum T_c varies from ~ 40K in the LBCO family to above

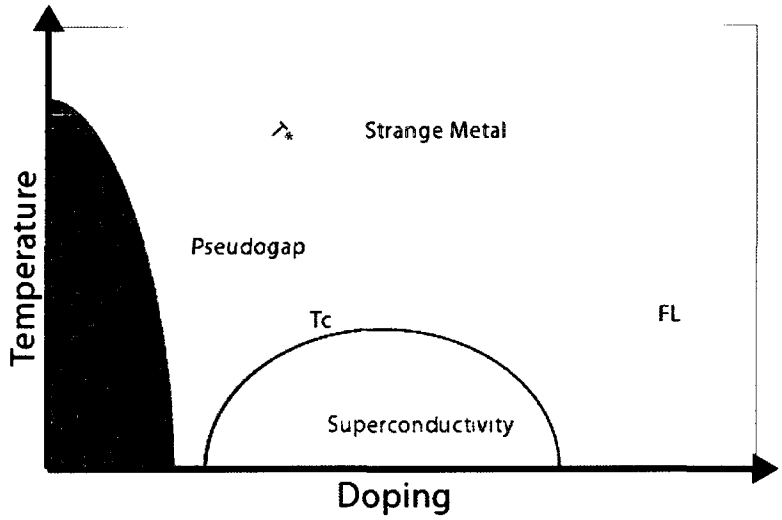

Figure 1.5: Phase diagram of Temperature vs Doping for the hole doped cuprates.

$90K$ in YBCO and $Ba_2Sr_2CaCu_2O_{8+y}$ (BSCCO). The superconducting dome region in YBCO goes from approximately $\delta \sim 0.7$ to $\delta = 0$. While it is possible to slightly overdope YBCO past the optimal doping at $\delta = 0.05$, in general, overdoping is only possible through cation doping, usually by substituting Ca for Y. The two regions of the phase diagram with lower and higher doping than maximum T_c are known as the underdoped and overdoped regions respectively. The overdoped region of the phase diagram has electronic properties similar to most metals in that the resistivity is proportional to T^2 in agreement with Fermi-liquid theory. The metallic region above the superconducting dome, known as the strange metal region, and for lower doping, known as the pseudogap region, shows peculiar properties that are unlike any other known metal. For example, it is generally agreed that both regions shows non-Fermi liquid behavior due to the Hall coefficient being temperature dependent and resistivity being linear (or sublinear in the case of the pseudogap) in temperature [18]. Since the pseudogap region of the phase diagram is the focus of study for this thesis, I will describe its properties in greater detail in the following chapter.

The Superconducting State

Superconductivity is perhaps the most studied phase of the cuprates; initial experiments were designed to compare and contrast the superconducting properties with materials that were well understood by BCS theory. Similar to BCS theory, the cuprates form Cooper pairs at the onset of T_c. This was confirmed shortly after the discovery of the HTSC by magnetic flux measurements in a ring of YBCO where the quantized flux, $\phi_0 = h/2e$, depends on twice the electron charge [19]. However, many of the other superconducting properties are quite different from conventional superconductivity. For example, YBCO is strongly type II (characterized by a gradual transition from purely superconducting to normal with applied magnetic field at much higher fields than conventional superconductors), with a very high upper critical field of $H_{c2} > 100T$. The anisotropy of the material is manifest in the characteristic length-scales associated with the superconductivity. YBCO has relatively very short coherence lengths ($\xi_{ab} \approx 2$ nm and $\xi_c \approx 0.4$ nm) and long London penetration depths ($\lambda_{ab} \approx 150$ nm and $\lambda_c \approx 800$ nm).

It is clear that HTSC have a different pairing mechanism than what would be expected from BCS theory. Interestingly, the symmetry of this pairing is much more complex than the s-wave, isotropic order parameter for conventional superconductors. The order parameter that describes the superconducting state has a $d_{x^2-y^2}$ symmetry [20, 21]. This results in an anisotropic pairing gap, $\Delta_{\vec{k}}$, in k space with the same symmetry characterized by four lobes with alternating sign of the phase and four nodes where the order parameter, and pairing gap vanishes.

Despite a thorough understanding of the superconducting properties of the HTSC, there is still a mystery about what occurs at T_c that causes electrons to pair up. A large part of the difficulty in understanding the superconducting state is lack of understanding of the normal state from which it condenses. The next chapter will include a survey of the normal properties of the HTSC for lower doping.

Chapter 2

Normal Properties of Underdoped Cuprates

2.1 The Pseudogap Regime

As mentioned in Chapter 1, superconductivity occurs when electron pairs, just above and below the Fermi energy, feel an attractive potential and form Cooper pairs of opposite spin and momentum and condense into a collective state. This process of pairing electrons lowers the energy of the system. The superconducting energy gap, manifest as a gap in the density of states surrounding the Fermi energy, refers to the energy required to break up a Cooper pair and create quasiparticle excitations. In a conventional superconductor, the gap begins to form at exactly T_c, the temperature that Cooper pairs and the corresponding long range order begin to form. In the underdoped HTSC, however, a phenomenon known as the pseudogap (PG) arises as the gap persists above T_c well into the normal state, up to a temperature referred to as T*. This region of the phase diagram, known as the pseudogap, is an integral part of the puzzle of high temperature superconductivity. In this chapter I will discuss the various experimental observations, their common phenomenology and theoretical models of high temperature superconductivity that attempt to incorporate the PG. I will also introduce other properties that have been observed in this region of the phase diagram, specifically charge and spin ordering known as stripes.

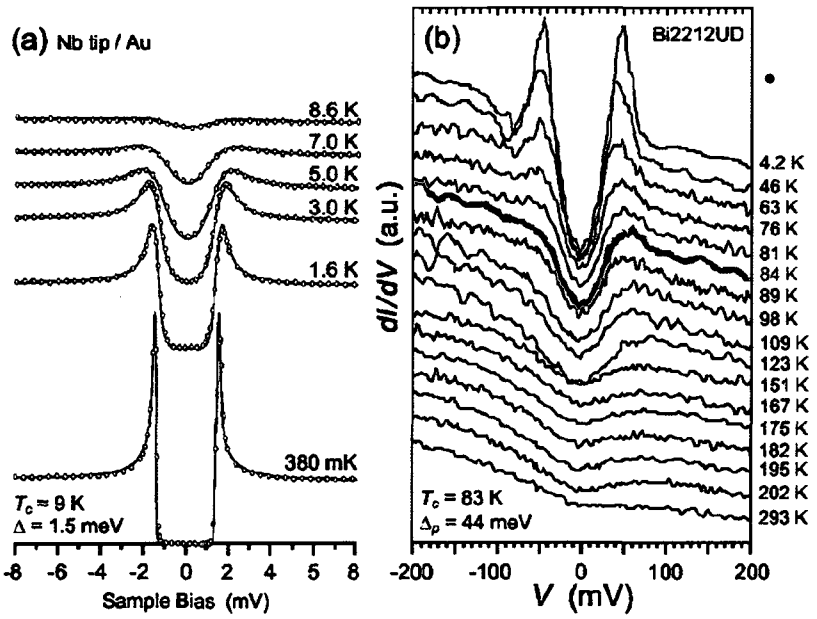

Figure 2.1: STM measurements of temperature dependent density of states. (a) Gap of a conventional superconductor, Nb with a $T_c \approx 9$. (b) Underdoped Bi2212 with $T_c \approx 84$. Note how the gap in the density of states persists above T_c. [22]

2.1.1 Pseudo-Gap Observations

Tunneling spectroscopy, is one of the most direct measures of the magnitude of the superconducting gap. The typical procedure is to grow a superconductor/insulator/normal junction and measure the current flowing as a function of bias voltage. When no current flows at thermal equilibrium and T=0, the fermi level equilibrates and is the same throughout the system, cutting halfway through the energy gap in the superconductor. This energy gap represents a lack of states where electrons can exist; current can only flow when the voltage is raised or lowered sufficiently outside of the energy gap such that electrons (or quasiparticles) can tunnel into empty states. Figure 2.1 illustrates the superconducting gap for both conventional and high-T_c superconductors. Experiments using nuclear magnetic resonance (NMR) spectroscopy [23], performed just over 20 years ago, were the first to reveal the existence of a gap in the electronic density of states above T_c. NMR makes use of two different techniques

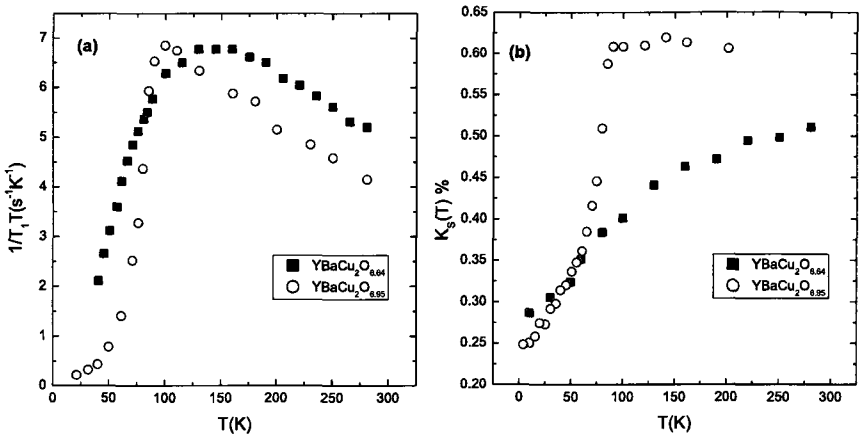

Figure 2.2: (a) The planar ^{63}Cu spin lattice relaxation rate [23]. The characteristic temperature T_{SL} is derived from the doping and temperature dependence on the peak in $1/T_1T$. (b) Knight shift of planar ^{63}Cu measured in optimal and underdoped YBCO [24]. Spin susceptibility is temperature independent until the pseudogap temperature T^0.

that are sensitive to the density of states. Interestingly, NMR was the first technique to find two characteristic temperatures in the pseudogap. The first technique, known as the Knight shift (K_s), measures the spin susceptibility, due to interactions with the spin orientations of the conducting electrons in an external field. This effective field couples to the ^{63}Cu nuclei in the CuO_2 planes. Normally, in a metal with a broadly distributed and featureless density of states, the K_s is temperature independent and in a Fermi liquid, is directly proportional to the density of states at the Fermi surface. The second technique is the measurement of the spin-lattice relaxation rate, $1/T_1$, which can detect a second, lower crossover temperature T_{SL}. The NMR community usually refers to this second crossover as T^*, however, the higher crossover temperature T^0 has the same values and doping dependence as the pseudogap temperature, T^*, measured by other techniques. Both K_s and the $1/T_1$ rate are sensitive to the density of states, however $1/T_1$ is also influenced by AF fluctuations. For optimally doped samples, as the temperature is lowered, AF spin coherence increases

causing an increase in $1/T_1$ until T_c. In underdoped samples, due to the influence of the pseudogap, $1/T_1$ decreases well below T_c. The characteristic temperature due to the spin lattice relaxation, T_{SL} is observed as a peak in $1/T_1T$ as a function of temperature shown in Fig. 2.2(a). Both crossover temperatures can be observed for underdoped samples in K_s. K_s is temperature independent at high temperatures but begins to drop linearly once the temperature goes below T^0 and then decreases faster than linear with temperature at T_{SL} as seen in Fig. 2.2(b). Interestingly, the NMR characteristic temperature, T_{SL} does not merge with the superconducting dome like most other measurements, but instead continues towards the overdoped region of the cuprate phase diagram. An experimental phase diagram of these two crossover temperatures is shown in Fig. 2.3. T^0 and T_{SL} are distinct crossover temperatures and it has been suggested by cation substitution experiments that they are caused by different phenomena [25]; T^0 probes the density of states while the source of T_{SL} is referred to as the spin gap and is magnetic in nature.

The resistivity, $\rho(T)$, of the normal phase of the cuprate phase diagram has been studied in great detail and also indicates the opening of the pseudogap. In general, for low doping the resistivity increases; this is expected since doping effectively raises the number of charge carriers. In the cuprates, ρ is highly anisotropic between the ab and c directions. In YBCO $\rho_c \approx 10\rho_{ab}$ and can be as high as 10^5 in BSCCO. As shown for YBCO in Fig. 2.4(a), $\rho_{ab}(T)$ changes markedly as a function of doping. For overdoped samples, $\rho_{ab}(T)$ approaches quadratic behavior signifying electron-electron scattering as predicted by Fermi-liquid theory. Near optimal doping, $\rho_{ab}(T)$ is linear from high temperatures down to T_c. Interesting behavior in the slope of $\rho_{ab}(T)$ begins to emerge at lower doping. At higher temperatures, $\rho_{ab}(T)$ is supralinear until $T<T^*$ when the slope changes exhibiting an S-shaped behavior. By comparison with other spectroscopic techniques, this change in behavior of the resistance is attributed to the opening of the pseudogap. Ando *et al.* have used a resistivity curvature

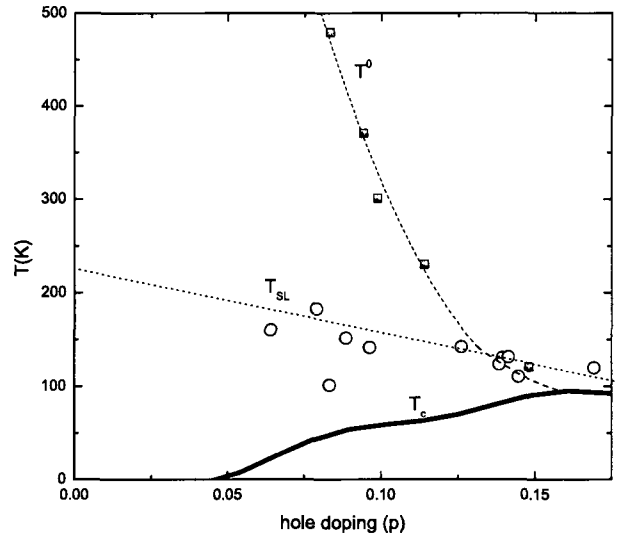

Figure 2.3: Experimental phase diagram of NMR crossover temperatures. T^0 (blue squares) for YBCO and T_{SL} (usually T* in NMR) for YBCO (green circles) and La-YBCO (red circles) as a function of holes per unit cell of CuO_2. The data is deduced from susceptibility measurements and T_1 measurements on ^{63}Cu in the CuO_2 planes. . Lines are used as guides for the eye. Data is adapted from [26].

mapping technique to plot the evolution of ρ_{ab} as a function of temperature and doping [27]. Figure 2.4(b) shows a plot of the resistivity curvature for YBCO. The underdoped S-shape in the resistivity is represented by the crossover from sublinear (negative derivative, shaded blue) to linear ($d^2\rho_{ab}/dT^2 = 0$, shaded white). Eventually the curvature goes to supralinear (positive derivative, shaded red) in the overdoped, Fermi liquid-like regime. This transport property is similar in LSCO and BSCO, demonstrating the universality of the transport property across the phase diagram,

The pseudogap has been observed by a variety of other experiential probes. These include: inelastic neutron scattering which observes a gap around the Fermi energy in the dynamic spin susceptibility [29], specific heat measurements, [30], Raman spectroscopy which observes a loss of spectral weight [31] and angle resolved photoemission spectroscopy (ARPES) which directly observes the energy gap [32, 33]. To summarize some of the more relevant observations of the pseudogap: The pseudogap appears to evolve into the superconducting gap (see Fig. 2.1(b)), both the pseudogap

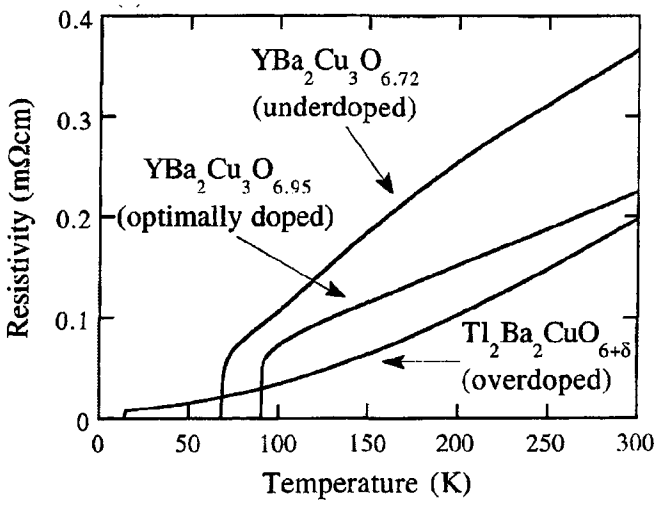

(a)

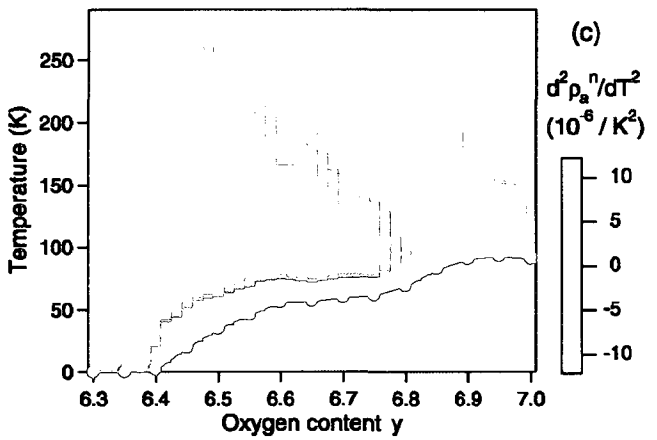

(b)

Figure 2.4: (a) $\rho(T)$ data representing underdoped, optimally doped and overdoped cuprates [28]; (b) $d^2\rho_{ab}/dT^2$ for YBCO as a function of hole-doping p. [27].

and the superconducting gap have a similar d-wave symmetry, T^* (though with some magnitude dependence in the normal state) generally merges with T_c in the slightly overdoped region of the phase diagram, and the gap in the pseudogap is nearly temperature independent.

2.1.2 Models of the Pseudogap

Any theory that attempts to understand HTSC must be able to incorporate the pseudogap and explain the relationship (or lack thereof) between the pseudogap and superconductivity. There are two classes of models that attempt to understand the pseudogap in the context of superconductivity. The first attempts to explain the pseudogap as being a precursor superconductivity; since, the pseudogap and superconductivity occur at the same doping level many theorists believe there must be a relationship between the two. The second group of models explain the pseudogap as a phenomenon that is separate and competes with superconductivity for the same electrons. Not surprisingly, due to the enigmatic nature of high temperature superconductivity, there are experimental results that seem to lend credence to both models.

Phase Fluctuation Models

The first class of models are based on the notion of phase fluctuations. Many of these have at least some similarity to P.W. Anderson's resonating valence bond (RVB) model [34]. The basic idea behind the original theory is that we begin with an undoped, antiferromagnetic (AF) Mott insulator consisting of a spin liquid. This spin liquid is an ensemble of spins in a superposition of all possible antiparallel spin pair configurations. Until the material is doped, the pairs are trapped since no site can have double occupancy. Once the material is doped, the spin pairs can move. Excitations in the material can then be described by two types of particles: holons, which are spinless bosons, and spinons which are chargeless, spin 1/2 fermions. According to this model, the PG forms via a magnetic transition when the spinons pair, and the SC transition occurs when the holons Bose condense.

A similar model to the RVB model, is the idea of precursor pairing [35, 36, 37]. In order for bulk superconductivity to exist, the phase of the order parameter needs to be

continuous and slowly varying across the material. This occurs in conventional superconductivity; the order parameter is uniformly suppressed to zero as the temperature decreases to T_c. This is due to the long coherence length and strong phase stiffness in conventional superconductors, making phase fluctuations energetically costly. The precursor superconductivity models focus on the fact that the order parameter in cuprates does not have much phase stiffness, therefore phase fluctuations can occur relatively easily at higher temperatures. While locally, between temperatures T_c and T^*, there may be some phase coherence, phase fluctuations destroy the overall phase coherence and hence destroy the superconductivity. These models argue that the pseudogap is a signature of this precursor superconductivity. The idea of precursor pairing has been used in a number of models. One of the more popular models of precursor pairing has been combined with the concept of charge stripes (for a review see [38]) whose appearance seem to coexist with other pseudogap properties. Much of the research in this thesis has been devoted to searching for stripe-like behavior in the pseudogap regime, hence I will deal with the models and experimental observations of charge and spin ordering in greater detail in the following section.

There are several experimental results that have been cited to support this view of precursor pairing. Among the first of these results are conductivity measurements [33]. These measurements show a gap in the c-axis conductivity that fills up as T^* is approached while the planar conductivity shows that charge transport becomes more coherent (as evident narrower Drude peak) below T^*. These results have been argued to be evidence of the "spin singlet" picture in the pseudogap phase [13]. In this picture, the spins pair into a singlet state below T^* resulting in a spin gap. This gap then reduces the scattering between the carriers in the CuO_2 planes resulting in a narrower Drude peak. The gap in the c-axis response is then as a result of the reduction in the density of states due to the combining of spin and charge degrees of freedom of the electrons that tunnel between the CuO_2 planes. ARPES measurements

[39], showing more detail of the gap, have been used to corroborate the conductivity results [40]. Nernst effect measurements seem to further corroborate this picture [41]. The Nernst effect measures a component of the transport corresponding to the transverse electrical conduction response to a thermal gradient in the presence of a magnetic field. While this effect is relatively small in normal metals it can produce a large effect in superconductors when vortices are present. This result in the cuprates has been interpreted as vortex-like excitations within the pseudogap phase. This interpretation has been recently challenged [42] since there are three plausible sources of pairing fluctuations that cause the large Nernst effect: quasiparticles with a small Fermi energy, amplitude fluctuations manifest as short-lived Cooper pairs, and the original interpretation of phase fluctuations due to vortices. As seen in Fig. 2.5, the Nernst effect follows the doping trend of T_c more than the dependence of T^*; it has been interpreted to be a precursor to superconductivity that occurs within the pseudogap phase. The fact that the pairing fluctuation onset occurs at temperatures below T^* implies that perhaps preformed pairs are not the sole cause of the pseudogap.

Competing Order Models

Based on arguments of continuity, it appears reasonable that the pseudogap and the superconducting gap arise from the same phenomenon. It is supposed that the glue for electron pairing, necessary for superconductivity, arises from fluctuations around an instability analogous to the instability caused by phonon-electron interactions in conventional superconductors. However, there could be several types of electronic instabilities each of which would lead to an energy gap and hence a gap in the density of states [40]. There are several models which posit that the pseudogap arises from a separate phenomenon than superconductivity. These include the circulating current phase proposed by Varma [43] and a d-density wave ordering model by Chakravaty *et al.*[44] based on a hidden d-wave symmetry. These models predict a separate phase

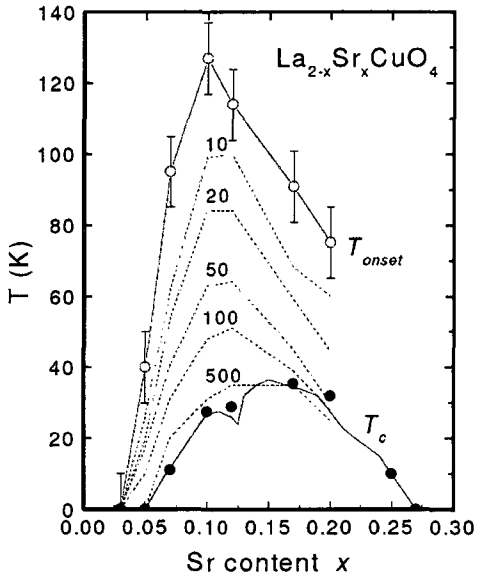

Figure 2.5: The Nernst signal as a function of doping in LSCO. The signal is believed to be due to the motion of vortices when a temperature gradient is applied to the sample. White circles indicate the onset of the Nernst signal while the contours indicate how the value of the Nernst coefficient changes with temperature and doping [41].

transition than the superconducting one and expect a gap in the density of states separate from the gap caused by superconductivity [40, 45].

There have been several conflicting recent experiments that argue whether or not there is one gap. Valla *et al.* [46] conclude that there is only one gap. They used ARPES for a study of LBCO at a 1/8th filled doping, where superconductivity is strongly suppressed but shows an underlying charge and antiferromagnetic order. They observe a gap with the same d-wave symmetry and magnitude as the gap in the superconducting state at higher dopings. They conclude that they see a non-superconducting state based on pairing, that either coexists with antiferromagnetism or is itself antiferromagnetic. Somewhat conflicting interpretations come from ARPES [47], Raman scattering [48], and STM data [49, 50] which show evidence for two gaps measured in the density of states. Based on STM measurements, the first gap is the larger of the two, it is spatially inhomogeneous, exists both above and below T_c

and follows the doping dependence of T^*. The second smaller gap, is much more homogeneous, it exists only below T_c and follows the same doping dependence as T_c. These results suggest that the pseudogap corresponds to a state that is distinct from the superconducting gap, it extends from the superconducting region to the pseudogap region of the phase diagram and is a separate, possibly competing, order. It should be noted that there are many who are skeptical about this interpretation. These materials are notoriously inhomogeneous and the STM technique samples several gaps at various locations along the surface. The two gaps could be caused or influenced by sample inhomogeneity at different locations rather than separate energy gaps.

2.2 Stripes

When AF Mott insulators are doped with holes, there is a competition between the AF lattice wanting to eject these holes, and a Coulomb repulsion that prevents total phase separation. As a result, these materials are believed to form a real-space pattern (either static or dynamic) of a micro-phase separation known as stripes [35, 51, 38]. These stripes consist of $1 - D$ metallic rivers of the doped holes, flanked by the AF correlations from the original insulator [38].

The existence of stripes in cuprates has provoked a debate over the role of stripes with respect to superconductivity. There are those who believe that stripes are detrimental to superconductivity as the stripe state is in direct competition with superconductivity [13]. While there is another school of thought that holds that fluctuating stripes is responsible for the pseudogap and its behavior [38]. In this latter model, the stripes serve as a basis for a model of precursor superconductivity. Around T^*, AF correlations begin and the holes begin to separate from AF regions. At this temperature, the phase separation results in AF insulating regions surrounded by charge stripes, however it is not yet globally superconducting. According to these models,

with lower temperatures, a spin gap would begin to open up well above T_c [52] based on the reduced dimensionality from the confinement of AF correlations. The charge stripes are then subject to the same gap coupled by a magnetic proximity effect. This proximity effect would be caused by pair hopping of holes between the charge-stripe and the surrounding AF regions. Bulk superconductivity would then occur when the local spin gaps along each charge stripe Josephson couple, acquiring long-range phase coherence. The existence of stripes is no longer in question as they have been observed directly and indirectly in a number of experiments. Investigating stripes may play a key part in understanding high temperature superconductivity since the pairing inevitably occurs in this background of inhomogeneous charge and magnetic order.

2.2.1 Spin and Charge Ordering in the Cuprates

Charge and magnetic order, incommensurate with the lattice spacings, have been observed in several experiments. Most of the information about charge and spin order come from neutron and x-ray scattering and STM. Static linear order, fluctuating order and nematic order, all attributed to stripes have been seen in a variety cuprates. Further ordering effects attributed to stripes have been seen in transport, ARPES, muon spin resonance (μSR) and NMR experiments. The rest of this section will deal with experimental observations of charge and stripe order in the cuprates. It is generally agreed that this ordering is in fact a signature of stripes, however, there are several conflicting interpretations of the data.

Scattering Experiments: Static and Fluctuating Order

The first evidence for static magnetic order was first seen in 1995 by Tranquada *et al.* in Nd doped LSCO (LNSCO) [53, 54]. At a doping level of 0.12 LNSCO has a low T_c of 5 K, and at around 55 K neutron scattering detect the onset of

static spin correlations. Using elastic neutron scattering, the AF order of the parent Mott antiferromagnet shows peaks in the corner of the Brillouin zone at wavevector $\vec{Q}= (\pi, \pi)$. The spin correlations are detected as Bragg peaks centered at wavevectors $\vec{Q_{sx}}= 2\pi(0.5 \pm \epsilon_s, 0.5)$ and $\vec{Q_{sy}}= 2\pi(0.5, 0.5 \pm \epsilon_s)$. A static spin density wave order, however, has only been seen in a handful of La-based cuprates known as the 214 cuprates, including $La_2CuO_{4+\delta}$ and LBCO at 1/8 doping. The correlation lengths of in-plane static spin order in these compounds are at least $200\AA$ ($\approx$ 50 lattice spacings). Static charge order in 1/8 doped LBCO was first directly seen much more recently in 2005 by Abbamonte *et al.* [55]. The charge order is also peaked in both lattice directions centered at $\vec{Q}= (0, 0)$ with wavevectors $\vec{Q_{cx}}= 2\pi(\pm\epsilon_c, 0)$ and $\vec{Q_{cy}}= 2\pi(0, \pm\epsilon_c)$. The charge order correlation length is at least $480\AA$ (about 125 lattice spacings) in the 214 cuprates. The charge order also sets in at slightly higher temperatures than the spin order.

Combining the results of x-ray and elastic neutron scattering gives important details about underlying translational symmetry breaking. The reciprocal lattice wavevectors for magnetic and charge ordering are related by $\epsilon_s \approx 2\epsilon_c$ meaning that the spin ordering length (with period 8) is roughly double the charge ordering length spin order (with period 4). Furthermore the fact that order in the plane is seen in both lattice directions means that these materials do not have unidirectional order throughout. The measured Bragg peaks are consistent with either alternating, orthogonal regions or layers of unidirectional order or a checkerboard like order (a superposition of spin and charge order in the same layer). Figure 2.6, shows a cartoon of uni-directional charge and spin stripe ordering domains.

While elastic neutron scattering can measure static order based on the location of the Bragg peaks, inelastic neutron scattering can provide complementary information based on the characteristics of fluctuations in the ordering. In YBCO, the original experiments were focused on a commensurate (at $\vec{Q}= (\pi, \pi)$) resonant peak at 41meV

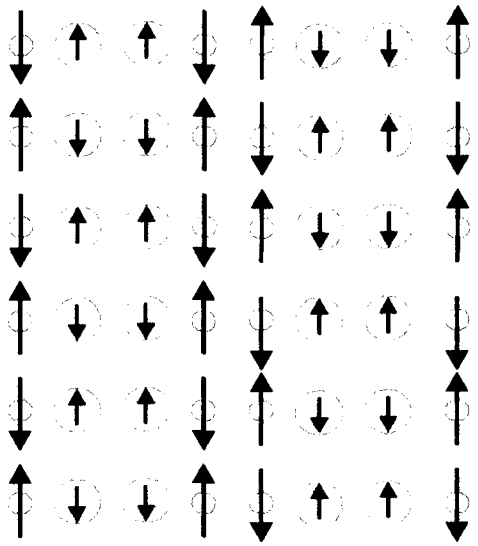

Figure 2.6: Cartoon of static stripe order observed in several cuprates. The spin ordering length is twice that of the charge order. The charge density is one hole for every two units of length along the stripe.

that grows in intensity and shifts in energy as the sample is cooled to T_c. In LSCO, the focus was originally on incommensurate peaks at low energies (< 20 meV) [56]. Subsequently, Mook *et al* discovered that the commensurate peaks in YBCO disperse towards incommensurate peaks at lower energies [57]. Eventually, the dispersion relations for YBCO and several other cuprates were mapped out. Figure 2.8 shows the location of maximum intensities of constant energy slices from inelastic neutron scattering in 1/8 doped LBCO. The excitations in LBCO can be described by using a stripe model consisting of AF ladders with a similar structure to the schematic in Fig. 2.6 [14]. The results of calculations based on this model are shown in Fig. 2.8 showing a good agreement with the data. Even in the absence of static order, this model of fluctuating order fits well to other cuprates. The universal hourglass curve of dispersion, below and above a resonance energy shown in Figure 2.9, is one of the strongest cases for the fluctuating stripe order model. The lower part of the hourglass is interpreted to be due to the result of spin waves within the stripe regions while the upper part of the dispersion curve is believed to be due to antiferromagnetic

regions which can be modeled with a two-leg spin ladder. The fact that this hourglass dispersion has been seen in both superconducting [58] and non-superconducting [59] samples serves to further support the stripe picture.

Inelastic neutron scattering is also useful for studying the rotational symmetry of fluctuations, since an anisotropic fluctuating structural state should give rise to an anisotropic excitation spectrum. Such a signature of rotation symmetry breaking has been identified in highly untwinned YBCO crystals. Hinkov *et al* studied the spin excitation spectra in underdoped untwinned YBCO crystals [60, 61]. The spectrum displays the expected hourglass shape with higher energy fluctuations above the resonance having roughly the symmetry of a square lattice. However, below the resonance where the dispersion is believed to be due to spin density waves, the intensities are quite anisotropic. The spectrum shows intense incommensurate peaks along the a axis with much weaker order shown along the b axis indicating an asymmetry. The lack of incommensurate static order along with an anisotropic fluctuating order is consistent with a fluctuating nematic phase in untwinned YBCO. In slightly underdoped YBCO, the anisotropic spectra change smoothly with no sign of a nematic ordering transition. However, strongly underdoped YBCO with T_c=35 K [62] has been interpreted to display a spontaneous onset of spin anisotropy and magnetic incommensurability around 150 K, strongly suggestive of a nematic phase transition. This type of order had been predicted by Kivelson *et al.* [63]; schematics of various types of stripe order can be seen in Figure 2.7.

The observation of incommensurate fluctuations in the microscopic magnetic ordering forms a strong experimental support for the models based on stripe formation [35, 51, 38].

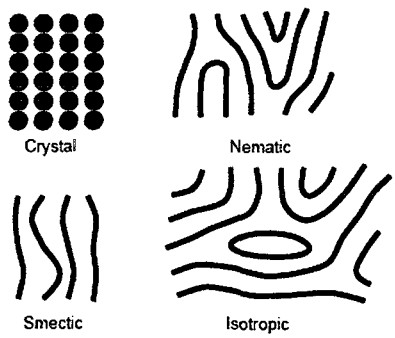

Figure 2.7: Schematic view of various types of stripe order predicted in [63].

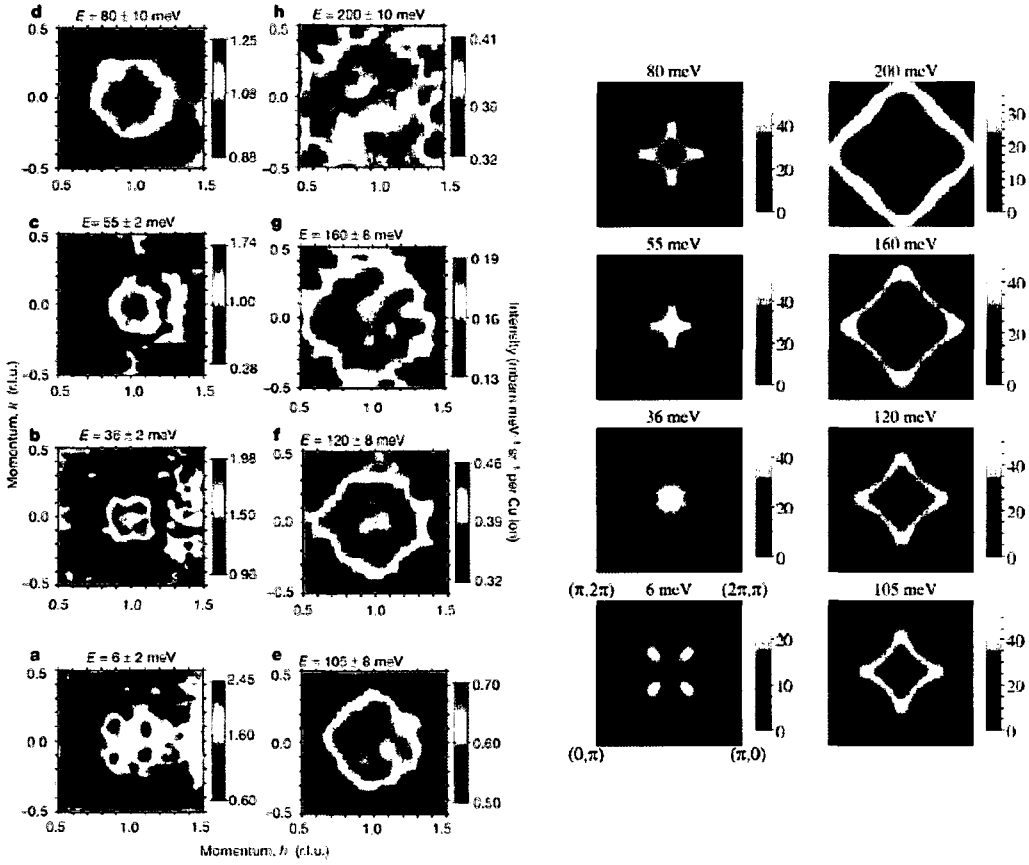

Figure 2.8: Magnetic Brillouin zone data for Neutron Scattering Left: Constant energy slices of the magnetic excitation spectrum of 1/8 doped LBCO [59]. Right: Simulation results using a coupled spin ladder model [14].

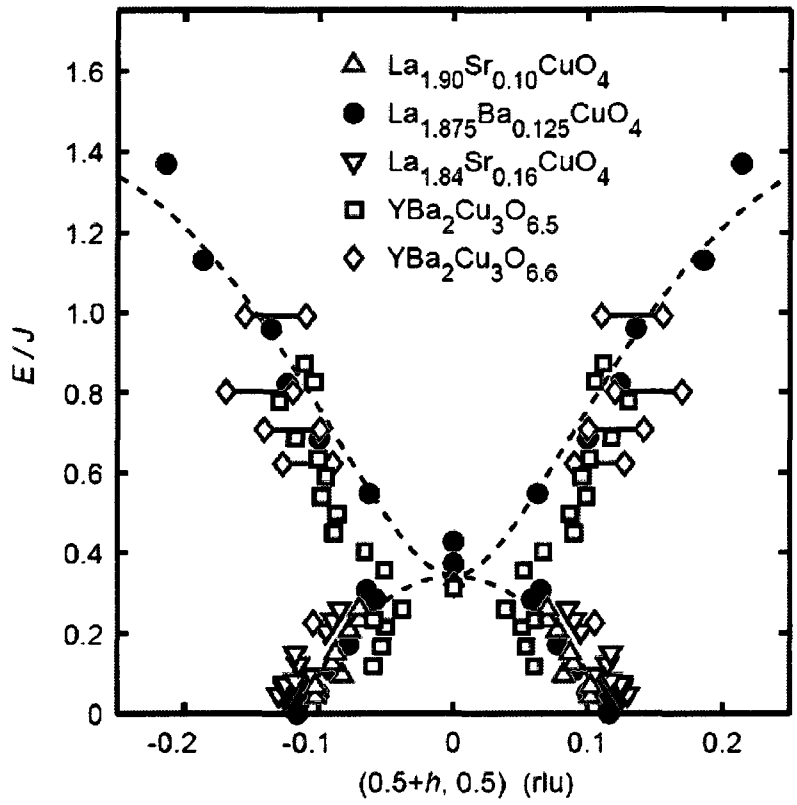

Figure 2.9: Hour glass dispersion of magnetic excitations in cuprates [56] scaled by the superexchange energy J (energy of exchanging spins at neighboring sites) of the parent AF insulator. The dispersions are centered at $\vec{Q}= (\pi, \pi)$. They are measured along the y direction for LSCO and LBCO and YBCO with δ=0.5 and low energy results for YBCO with $\delta = 0.4$. High energy results for YBCO $\delta = 0.4$ were measured along the diagonal of the Brillouin zone; the double symbols for YBCO are the result of two ways of interpolating the low energy and high energy results. The dashed curve is a theoretical fit for the dispersion due to a two-leg ladder model of stripe ordering [56].

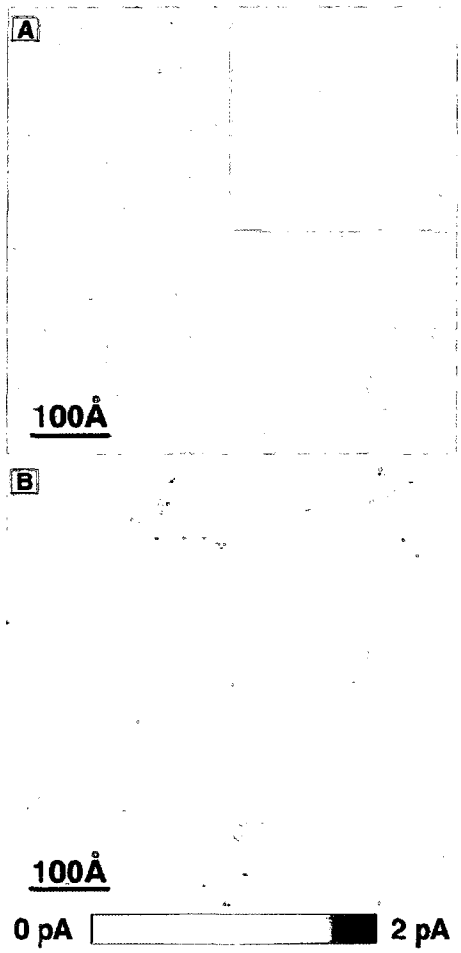

Figure 2.10: STM images of charge modulation at the cleaved surface of a BSCCO crystal with T_c=89K for the same 560 Å field of view. (A) The bare field of view used for vortex study showing an electronic modulation (the modulation is 45° to the CU-O chains) and the effects due to electronic inhomogeneities. The inset shows a 140 Åsquare field of view. (B) A view showing additional local density of states induced within 7 vortices. The checkerboard pattern of charge modulation can be seen within each vortex [64].

STM Experiments

While STM measurements have their limits since they are a surface probe which can only look at static features, they can reveal much information about real-space order in cuprates. The STM experiments that attempt to measure high resolution ordering have focused mainly on BSCCO and $Ca_{2-x}Na_xCuO_2Cl_2$ (CCOC) which meet the requirement for very high-quality sample surfaces once cleaved. Weak charge modulation with a very short correlation was first observed by scanning inside vortex cores [64] (See Fig. 2.10). A possible source for observed modulation is from quasiparticle interference, however when taking a Fourier transform of the modulation, the wavevectors are shown to be non-dispersive in energy in the pseudogap [65]. This result has been cited as unambiguous evidence for charge order [14]. There have been conflicting reports about whether or not the incommensurate wavevector is dispersive in the superconducting state [66, 67].

Neutron and x-ray scattering measurements allow for a possible checkerboard pattern instead of orthogonal domains or layers of uni-directional stripes. The observed STM patterns appears to agree with the checkerboard-like interpretation. However, since the correlation length of the ordering is short, the checkerboard pattern has been argued to be due to pinning of finite sized domains of stripes in the presence of disorder [38].

Transport Experiments

Transport measurements can also be used to search for signatures of charge ordering; if the ordered state breaks rotational symmetry, as is to be expected with uni-directional charge stripes, then the resistivity will become anisotropic in the plane. Ando *et al.* [68] studied resistivity anisotropy in un-twinned YBCO samples with δ's from 0.65 to 0 (see Figure 2.11). There is an anisotropy for every doping range. However at higher dopings, this is most likely due to ordering of CuO chains. As explained in Chapter 1,

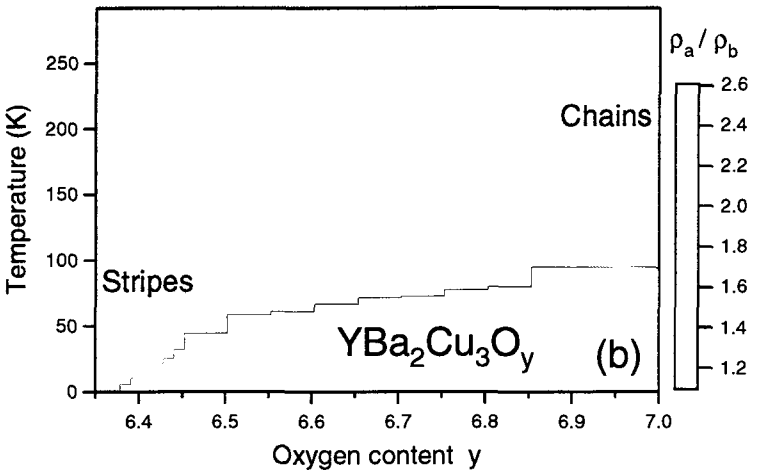

Figure 2.11: Phase diagram showing the evolution of the ratio of orthogonal resistivities ρ_a/ρ_b. The lower white region is the superconducting state. The anisotropy at higher dopings, which is due toe the CuO chains, decreases with doping. The increase of anisotropy at even lower doping signifies the onset of charge stripe ordering [68].

YBCO has an intrinsic anisotropy below $\delta \sim 0.4$. Above this doping, the CuO chains prefer to align along the b direction as the lattice symmetry changes from tetragonal to orthorhombic. At the higher dopings, the anisotropy decreases as temperature decreases. However the opposite occurs at lower dopings of $\delta = 0.55$ and 0.65 where the anisotropy decreases from 1.3 at room temperature to 2.5 at low temperature. The onset of low doping anisotropy suggests the onset of nematic order and agrees with the onset from neutron scattering experiments. The underlying structural anisotropy makes it difficult if not impossible to detect a nematic ordering temperature.

2.2.2 YBCO Resistance Fluctuations

Experiments proposed by Bonetti *et al* [69, 70], were initially designed to study transport properties of YBCO nanowires (100-300 nm) in order to investigate the possible formation of precursor superconductivity above T_c on mesoscopic length scales. During the characterization of the samples a fluctuating resistivity was discovered, with fluctuations much greater than the level of thermal noise [69, 70] (see Figure 2.12). As

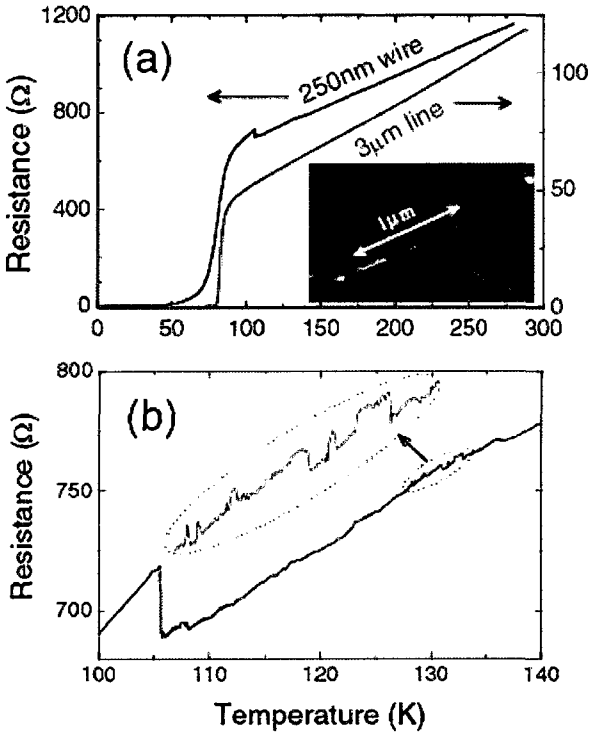

Figure 2.12: (a) Comparison of resistance vs temperature for 500 nm segments of a 250 nm and a 3 μm wide sample (b) Expanded view of the resistance vs temperature of the 250nm wide wire showing telegraph-like switching fluctuations. The fluctuations begin below ~150 K

seen in Fig. 2.13 for successive temperature sweeps, the resistance jumps occurred at different temperatures. The fluctuations were only seen in narrow wires (<500 nm). The fluctuations occur in the range T_c <T<220 K suggesting that the fluctuations are related to the pseudogap phase.

At fixed temperature, real time fluctuations were occasionally observed (see Fig. 2.14(a)) Taking a histogram of the resistance states, shown in Fig. 2.14(b), indicates that there is a bimodal distribution. This indicates that the fluctuator prefers two states, however there also appears to be a continuum of intermediate states.

It has been shown via neutron scattering [71, 72], that the correlation length, ζ, for charge stripes is on the order of 35-40nm. Hence, if stripes were present, fluctuations should be more pronounced on the length scale of these wires. The

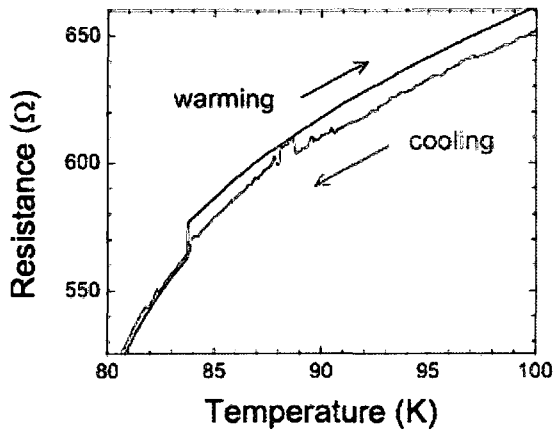

Figure 2.13: Successive cooling and warming runs measuring resistance vs temperature for a 250 nm wide wire. Between 85 and 90 K, the cooling sweep exhibits multiple-level switching, with the high resistance state having the same value as the resistance during warming.

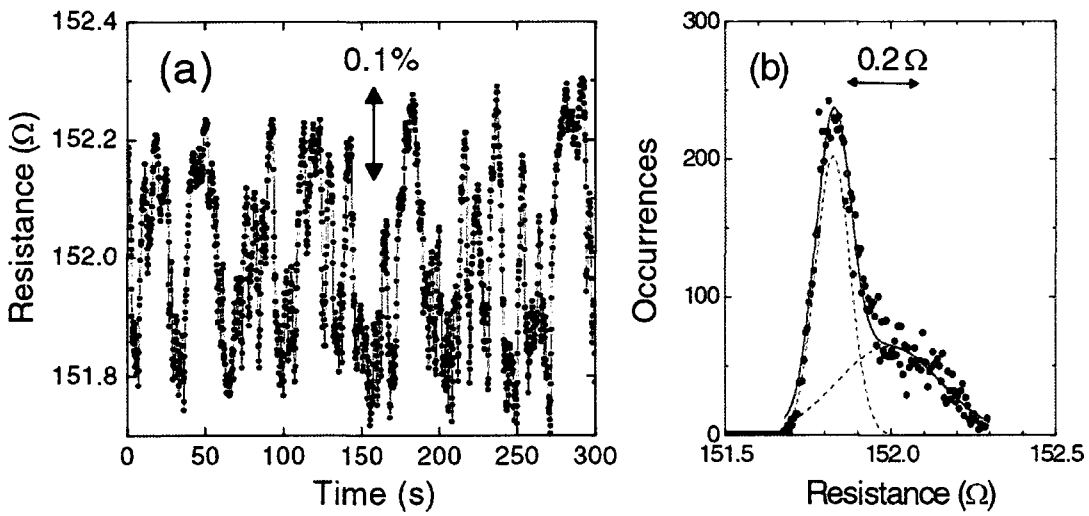

Figure 2.14: (a) Resistance vs time at 100 K showing large 0.25%, telegraph-like fluctuations. (b) A histogram of resistance values demonstrating bimodal behavior.

fact that these fluctuations were only seen in narrow lines suggests that perhaps these large slow fluctuations were due to pinning of stripe fluctuations. The quest to resolve whether or not these results are a signature of stripe domains has been a large motivation for this project. In the next chapter, I will introduce several ideas on measuring resistive noise that are used in order to help elucidate the nature of these fluctuations. From these noise measurements I will show how it is possible to infer dynamic, thermodynamic and symmetry characteristics of the underlying noise source.

Chapter 3

Transport Noise

3.1 Introduction

The experimental method of this research involves measuring resistance noise in YBCO and Ca-YBCO wires. Invariably, resistance noise is caused by underlying fluctuations that couple to the resistivity. The goal of studying transport noise is to gain key insight into the composition of these fluctuating regions and the physics behind what drives the fluctuations. Specifically, we would like to study the fluctuation size and dynamics, temperature dependence, doping dependence and isotropy of the normal state resistance noise in order to probe the pseudogap phase. Since T^* is associated with the an S-shaped change in slope in the resistivity (see § B-sec:obs), transport noise may be able to show precursor fluctuations. Furthermore, since resistively anisotropic charge stripes are believed to form in YBCO [68], and fluctuating magnetic order has been observed via neutron scattering [57] it is feasible that these characteristics should manifest themselves in the resistance noise. Ostensibly, the coupling of fluctuating unidirectional charge stripes to transport noise should be simple; the resistance of a charge stripe should be anisotropic, with much lower resistance along the stripe than perpendicular to it. Spin order, typically in the form of spin density waves is known to manifest itself as resistance fluctuations; noise measurements of spin density waves in Cr have been particularly sensitive to both wave vector dynamics, which set in at higher temperatures, and polarization dynamics [73, 74, 75].

3.2 1/f Noise

For the most part, this thesis deals with a particular type of noise known as 1/f noise, where f is the frequency, and typically follows a dependence of $1/f^{\alpha}$ where $0.9< \alpha <1.2$. This type of noise exists in addition to both thermal and quantum noise and is nearly ubiquitous in electronic devices. Over the last several decades, vast amounts of data have been accumulated and many models have been proposed with the goal of gaining insight into the types of mechanisms behind 1/f noise [76, 77]. A range of models have been developed that can help to shed light on many of the physical properties of the sources of 1/f noise. One of the most successful of these models, the Dutta Horn model, will be discussed in this section.

Standard noise measurements involve analysis of the voltage across a resistor as a function of time $V(t)$. With constant dc current, the voltage fluctuates around a value, $\langle V \rangle = V_{DC}$. The power spectrum, $S_V(f)$ is related to voltage fluctuations via the autocorrelation function $C_v(t)$ where

$$C_V(t) = \langle V(t)V(0) \rangle - \langle V \rangle^2 \tag{3.1}$$

and

$$S_V(f) = \frac{1}{\sqrt{2\pi}} \int_{-\infty}^{\infty} C_V(t) e^{-2\pi f t} dt \tag{3.2}$$

where f is the frequency. With no current flowing and $\langle V \rangle = 0$, the fluctuations are known as Johnson noise and are given by $\langle (\delta V)^2 \rangle = 4k_B T R \Delta f$ where k_B is the Boltzman constant. Johnson noise has no frequency dependence (at least for frequencies $\ll 1/\tau_c$, where τ_c is the time between molecular collisions) and it can be eliminated for R$\rightarrow$ 0 (like in a superconductor) and reduced for lower T.

A main characteristic of 1/f noise is that it is scale invariant for $\alpha = 1$. The power spectral density for 1/f noise can be written as $S_V(f) = C/f$, where C is some

constant. Integrating the power spectrum between two frequencies, f_1 and f_2 gives

$$P_V(f1, f2) = \int_{f1}^{f2} S_V(f)df = C \ln \frac{f2}{f1}. \tag{3.3}$$

In other words, summing the noise over a frequency range with a fixed frequency ratio $f2/f1$ will give a constant noise power. Therefore the noise power over octave (successive doublings) of frequency (i.e. 2 Hz to 4 Hz or 4 Hz to 8 Hz) should be identical. The second property of 1/f noise is that it is weakly non-stationary (i.e. stationary only over a frequency range). Stationarity here means that the average noise power as a function of frequency should not change as a function of time. The stationarity only holds over a band-pass filtered power spectral density. Unfiltered 1/f (for $\alpha = 1$) noise is not stationary since there is no low frequency cutoff and the observation time for very low frequencies approaches infinity.

Typically, the magnitude of $1/f$ noise measured in resistors varies inversely with the volume of the system being measured. This is because the smaller the system the larger the effect of a property that causes a fluctuating resistivity; this is a standard statistical property that averages become more accurate for larger samples. It is typical to plot normalized noise data as a function of sample volume.

3.2.1 The Dutta-Horn Model

The basic building block of the Dutta-Horn model of 1/f noise is the two level system (TLS). The levels of each TLS are metastable states associated with different resistances separated by a free energy barrier $E_{\pm}$ and offset by an amount ΔE. The single TLS has an effective fluctuation time, $1/\tau = 1/\tau_{up} + 1/\tau_{down}$, and is manifest as a series of discrete resistance changes, ΔR, known as random telegraph noise. The

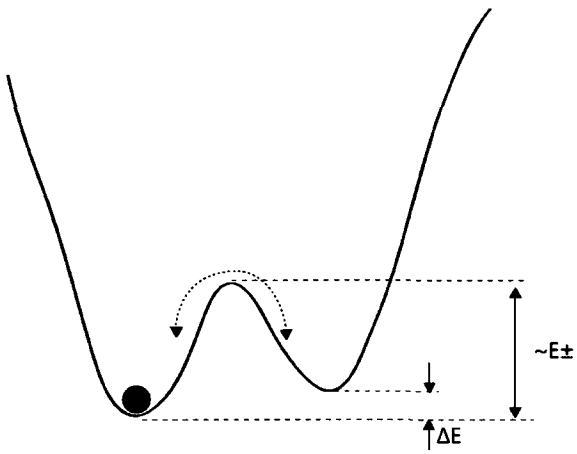

Figure 3.1: Two level system.

autocorrelation of this time trace is given by a decaying exponential

$$C_V(t) \propto e^{-t/\tau}. \tag{3.4}$$

The power spectrum is then described by a Lorentizan form:

$$S_R(\omega) \propto \frac{\tau}{1+\omega^2\tau^2}. \tag{3.5}$$

where $\omega = 2\pi f$. For the case of only thermally activated kinetics, the time spent in each state is given by

$$\tau_1 = \tau_0 e^{(E^{\pm}+\Delta E/2)/k_B T} \tag{3.6}$$

$$\tau_2 = \tau_0 e^{(E^{\pm}-\Delta E/2)/k_B T}, \tag{3.7}$$

where τ_0 is a typical attempt time of on the order of 10^{-12} sec in metallic systems. The Dutta-Horn model supposes a distribution of many TLS with varying energy barriers and level splittings, $D(\Delta E, E_{\pm})$, each with a Lorentzian power spectrum. If we assume that $D(E_{\pm})$ is smooth and ignore the variation in ΔE we can write $D(E_{\pm}, \Delta E) = D(E_{\pm})n_s$ where n_s is the density of fluctuators. This means that

$D(E_\pm)n_s\Delta(E_\pm)$ is the density of the TLS that have activation energies in the interval from $E_\pm$ to $E_\pm + \Delta E_\pm$. If we assume that we have an ensemble of TLS, $S_R(f)$ is then made up of a sum of Lorentzians

$$S_R(\omega) \propto \int_{\tau_1}^{\tau_2} D(\tau)\frac{\tau}{1+\tau^2\omega^2}d\tau, \tag{3.8}$$

where $D(\tau)$ is the distribution of barrier dependent fluctuation times $\tau(E_\pm)$. If the TLS can be described by thermally activated kinetics, $\tau = \tau_0 e^{E_\pm/k_BT}$, we can describe the power spectrum as

$$S_R(\omega,T) \propto \int D(E_\pm)\frac{\tau_0 e^{E_\pm/k_BT}}{1+(\tau_0\omega e^{E_\pm/k_BT})^2}dE_\pm \propto A(\omega,T)/\omega \tag{3.9}$$

resulting in the characteristic 1/f dependence. The variable $A(\omega,T)$ is proportional to the fraction of fluctuators with rates within an octave of ω. Here we have made the assumption that the distribution of activation energies is smooth on the scale of k_BT and centered around the energy $\tilde{E} = -k_BT\ln(\omega\tau_0)$. Based on the key assumption of a smoothly varying distribution of thermal activation energies, the Dutta Horn model attempts to relate the frequency dependence of the noise spectrum to the temperature dependence of the noise spectrum. Firstly, we look at the frequency dependence of the noise spectrum with varying distribution of activation energies. A uniform distribution of $D(\tilde{E})$ gives us exactly $\partial\ln S_R/\partial\ln f = 1$ while any other nonuniform distribution would yield $\partial\ln S_R/\partial\ln f = \alpha$ where typically $0.8 < \alpha < 1.4$ [76]. Secondly, with respect to the temperature dependence, if we assume a uniform $D(\tilde{E})$ with one fluctuator per octave, for successive octaves $\tau_1/\tau_2 = e^{(E_1^\pm - E_2^\pm)/k_BT} = 2$. By doubling the temperature, the fluctuations increase, the characteristic times become shorter, $\tau_1/\tau_2 = 1$, and the number of fluctuators per octave doubles. Assuming no temperature dependance on the coupling of the fluctuators to the resistance noise or the density of TLS, then a uniform $D(E)$ would give $A \propto T$. Any nonuniform

$D(\tilde{E})$ would result in a nonlinear temperature dependence, $A \propto T^{\beta}$. The Dutta Horn relation is based on the fact that the frequency exponent, α and the temperature exponent β must be related since they are both dependent on $D(\tilde{E})$. The Dutta Horn relation is typically expressed as

$$-\partial \ln S_R / \partial \ln \omega = 1 + \frac{1}{ln(\omega\tau_0/2\pi)}(\partial \ln S_R / \partial \ln T - 1) \tag{3.10}$$

where the derivatives of S_R are understood to be defined locally. ω is limited by the measurement window and is typically on the order of 10-100 Hz. For $1/\tau_0 \approx 10^{10} - 10^{12}$ Hz, $\ln(\omega\tau_0) \approx -25$. The Dutta Horn relation has been successful in fitting noise features in a variety of metals and amorphous metals which have uniform or smoothly varying distributions of thermal activation energies. When the Dutta Horn relation breaks down, this can indicate sharp changes in the underlying kinetics of TLS as a function of T or in the distribution of activation energies.

3.3 Fluctuation Isotropy

While the bulk resistance is usually isotropic, individual resistance fluctuations can have a different symmetry. In this section we discuss a technique developed for measuring an empirical macroscopic parameter for studying the isotropy of local fluctuators using global measurements [78, 79, 77]. The isotropy measurement can help to narrow in on the underlying source of fluctuations, since various noise sources such as carrier number fluctuation and mobility fluctuations can each display a distinct isotropy. The assumptions of the analysis include: the fluctuations in resistance occur in equilibrium, the sample is homogeneous and linear in its macroscopic properties, and that the fluctuations in a given volume are small. In order to study the tensor property of the underlying resistivity fluctuations, we develop the isotropy parame-

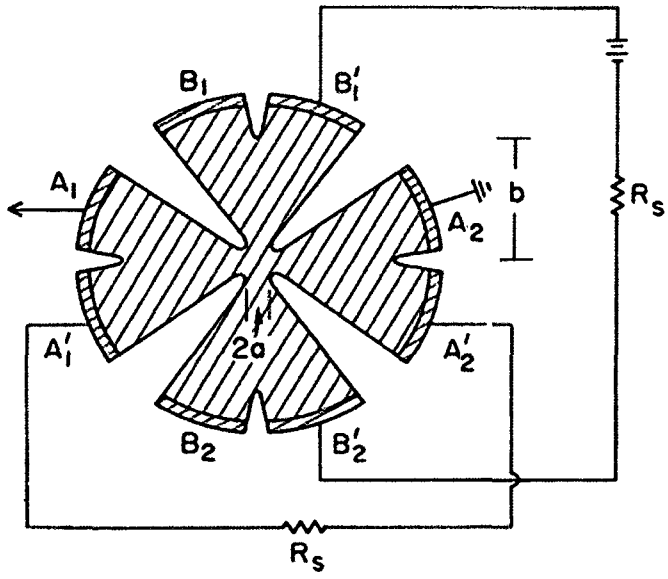

Figure 3.2: Isotropy measurement geometry [78]

ter[1] by analyzing the planar resistor shown in Figure 3.2 . The resistor has 8 total contacts, 4 for current and 4 for voltage measurements labeled A1, A1', A2, A2', B1, B1', B2 and B2'. We can describe the resistance fluctuations in terms of local fluctuations in the electric field, $\delta\vec{E}$. For simplicity, the analysis ignores the current-voltage distinction. When flowing current and measuring the voltage fluctuations across the A contacts, we can then write

$$\delta V_A = \int \delta\vec{E} \cdot \vec{j_A} d^2\vec{r}. \tag{3.11}$$

Here $\vec{j_A} = \vec{J_A}/I_A$ where I_A is the applied current in the A direction and $\vec{J_A}$ is the mean steady-state current density (all variables not preceded by a δ are understood to be expectation values). Expanding in $\delta\vec{E}$ to first order in $\delta\boldsymbol{\rho}$

$$\delta\vec{E} = (\delta\boldsymbol{\rho})\vec{J} + \boldsymbol{\rho}\delta\vec{J} \tag{3.12}$$

[1]The original derivation of the isotropy parameter can be found in [79] and [80]

where the variation in $\vec{J}$ is caused by the variation in ρ. Combining Eqs. 3.11 and 3.12, we have

$$\delta V_A = \int \vec{j_A} \cdot (\boldsymbol{\rho}\delta\vec{J} + \delta\boldsymbol{\rho}\vec{J}) d^2\vec{r}. \tag{3.13}$$

For a constant current it can be shown that the second part of the integral in Eq. 3.13 is 0. We can write

$$\int \vec{j_A} \cdot (\boldsymbol{\rho}\vec{J}) d^2\vec{r} = \int \delta\vec{J} \cdot (\boldsymbol{\rho}\vec{j_A}) d^2\vec{r}. \tag{3.14}$$

Since for a conservative field $\boldsymbol{\rho}\vec{J_A} = \vec{E_A} = \nabla_r \phi_A$, we can rewrite Eq. 3.14 as:

$$\frac{1}{I_A}\int \delta\vec{J} \cdot \nabla_r \phi_A d^2\vec{r} = \frac{1}{I_A}\int_{boundary} \phi_A(\delta\vec{J} \cdot \vec{n}) ds \tag{3.15}$$

However, current does not flow normal to the surface boundary (except at the contacts) so $\delta\vec{J} \cdot \vec{n} = 0$ here. At the contacts, the current and the potential ϕ_A are constant so $\int_{contacts}(\delta\vec{J} \cdot \vec{n}) ds = 0$. We can now rewrite Eq. 3.11 as

$$\delta V_A = I_A \int \vec{j_A}(\delta\boldsymbol{\rho})\vec{j_A} d^2r + I_B \int \vec{j_B}(\delta\boldsymbol{\rho})\vec{j_B} d^2r. \tag{3.16}$$

With the resistance fluctuations defined as

$$\begin{pmatrix} \delta V_A \\ \delta V_B \end{pmatrix} = \begin{pmatrix} \delta R_A & \delta R_C \\ \delta R_C & \delta R_B \end{pmatrix} \begin{pmatrix} I_A \\ I_B \end{pmatrix} \tag{3.17}$$

where the first integral in Eq. 3.16 represents δR_A and the second integral is δR_C. If there is no applied H field and no spontaneous time-reversal symmetry-breaking, the off diagonal parts of the resistance fluctuation matrix should be identical due to the Onsager reciprocal relation.

We now introduce the isotropy parameter, defined in terms of the resistivity fluctuations.

$$S \equiv 2\langle \mathrm{Det}(\delta\boldsymbol{\rho})\rangle / \langle \mathrm{Tr}[(\delta\boldsymbol{\rho})^2]\rangle. \tag{3.18}$$

S can take the values $-1 \leq S \leq 1$. If we assume that the sample is isotropic and homogeneous meaning that the resistivity is on average scalar and the fluctuations $\delta\boldsymbol{\rho}$ do not have a preferred direction or location then

The resistivity fluctuations can then be calculated in a fixed-axis form and written in terms of the S. Calculations, details of which can be found in [80], give the result

$$\langle(\delta\rho_{xx})^2\rangle = \langle(\delta\rho_{yy})^2\rangle = \gamma(S+3)/4 \tag{3.19a}$$

$$\langle\delta\rho_{xx}\delta\rho_{yy}\rangle = \gamma(1+3S)/4 \tag{3.19b}$$

$$\langle(\delta\rho_{xy})^2\rangle = \gamma(1-S)/4 \tag{3.19c}$$

$$\langle\delta\rho_{xy}\delta\rho_{xx}\rangle = \langle\delta\rho_{xy}\delta\rho_{yy}\rangle = 0, \tag{3.19d}$$

where γ is a constant. For $S = 1$, the fluctuations are scalar (fully isotropic), $<\delta\rho_{xx}\delta\rho_{yy}>=<(\delta\rho_{xx})^2>$ and $<(\delta\rho_{xy})^2>=0$. For $S = 0$, the fluctuations are dyadic and $\langle\delta\rho_{xx}\delta\rho_{yy}\rangle = \langle(\delta\rho_{xy})^2\rangle$. For $S = -1$, the fluctuations are traceless (fully anisotropic) and $\langle(\delta\rho_{xx})^2\rangle = \langle(\delta\rho_{xy})^2\rangle = -\langle\delta\rho_{xx}\delta\rho_{yy}\rangle$. These are the local resistivity fluctuations within the sample that would add up to give the global, measurable resistance fluctuations δR. By combining Eqs. 3.16 and 3.19, the values for the resistance fluctuations are

$$\langle(\delta R_A)^2\rangle = \theta\rho^2 \int j_A^4 d^2\vec{r}(3+S)/4 \tag{3.20a}$$

$$\langle(\delta R_C)^2\rangle = \theta\rho^2 \left[\int (\vec{j_A}\cdot\vec{j_B})^2 d^2r(3+S)/4 + \int (\vec{j_A}\times\vec{j_B})^2 d^2\vec{r}(1-S)/4\right] \tag{3.20b}$$

where θ is some constant. We can solve for the cross correlation by using the equation for δV_B allowing for current to flow along both sample directions.

$$\langle\delta R_A\delta R_B\rangle = \theta\rho^2 \left[\int (\vec{j_A}\cdot\vec{j_B})^2 d^2r(3+S)/4 + \int (\vec{j_A}\times\vec{j_B})^2 d^2\vec{r}(1+3S)/4\right]. \tag{3.20c}$$

We can then write a parameter, Q, in terms of the measurable variables that is sensitive to the isotropy parameter

$$Q+1=2+\frac{\langle \delta R_A \delta R_B \rangle + \langle (\delta R_C)^2 \rangle}{\langle (\delta R_C)^2 \rangle} = \frac{4SG}{3+S+G-SG} \tag{3.21}$$

where G is a sample dependent geometric factor

$$G = \frac{\int (\vec{j_A} \times \vec{j_B})^2 d^2r}{\int (\vec{j_A} \cdot \vec{j_B})^2 d^2\vec{r}}. \tag{3.22}$$

Finally, we can write S in terms of the measurable quantity Q and the geometric factor G

$$S = \frac{(Q-1)(3+G)}{3G-Q+1+QG}. \tag{3.23}$$

Geometrical Factor Calculation

Part of the calculation of S involves a calculation of G particular to the geometry of the sample. Using a C++ based software called $freefem++$, we calculated the electric potential from Poisson's equation, $\nabla^2\phi(\vec{r}) = 0$, over the geometry. The measurements of the geometry (1/4 of an 8 probe sample) had a diameter of the central area of 7 μm. The sample calculations were performed over a 50 μm^2 area with a 3 μm wide trench along the diagonal. The $freefem++$ software uses an adaptive mesh technique. This technique is useful since we are able to calculate with greater detail, the variations of the electric potential at bottlenecks in the geometry where the current density should be highest. An example of the mesh grid used to calculate the potential can be seen in Fig. 3.3(a). The mesh density was approximately 10 times greater at the curvature near the center since this is where the current density is the highest and varies the most. Only 1/4 of the sample was calculated

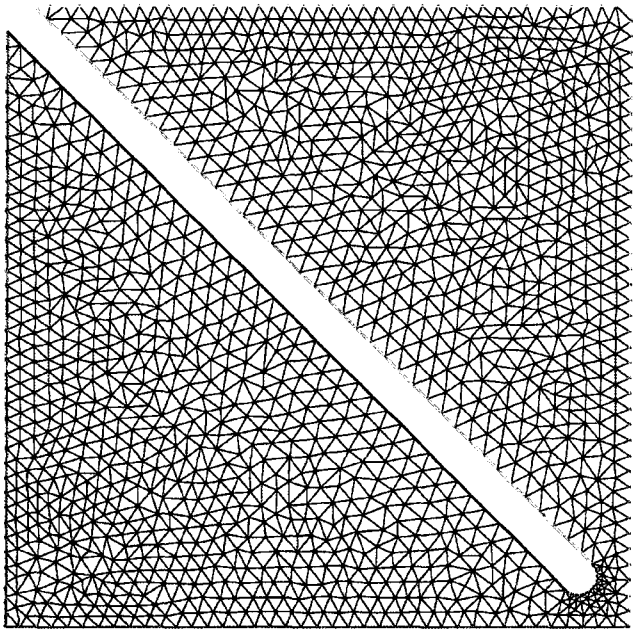

(a)

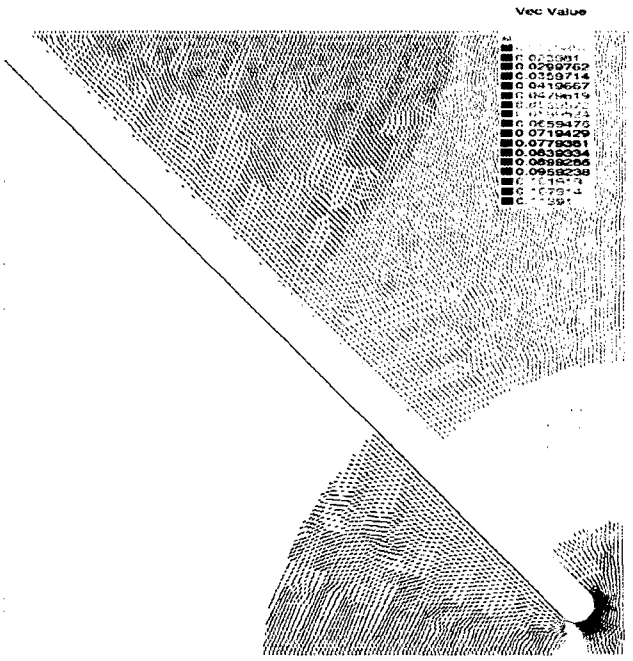

(b)

Figure 3.3: (a) The mesh for calculating the electric potential in the isotropy measurement geometry. The grid density shown is 1/6 of the density used in the calculation. (b) The electric field vectors, with arbitrary units, flowing in the B direction, from the top contact to the bottom contact.

due to four-fold symmetry. The potential was calculated assuming equipotentials, remaining at their initial values at the contacts, and the derivative of the potential was zero at the other boundaries. The electric field for the B direction was then calculated as $\vec{E_B}(x,y) = -\nabla\phi_B$. The electric field, for current flowing in the B direction, can be seen in Fig. 3.3(b). $\vec{E_A}(x,y)$, for current flowing in the A direction, was calculated by symmetry. As expected the current density is highest in the center of the sample geometry meaning that fluctuations there should have a larger weight in the macroscopic resistance fluctuations. The $freefem++$ code can be found in Appendix A.1. Once the current densities were calculated for the sample geometry, we calculated G by summing the cross and dot products of the current densities over the geometry.

$$G \approx \frac{\sum_i (\vec{j_{Ai}} \times \vec{j_{Bi}})^2 \text{Area}_i}{\sum_i (\vec{j_{Ai}} \cdot \vec{j_{Bi}})^2 \text{Area}_i} \tag{3.24}$$

The pattern yielded a result of $G = 1.11$. Previous calculations of G, yielded a larger value of $G \approx 1.3$ [79, 80], however they used a less detailed 65×65 grid. Our result was lower most likely due to the fact that we were able to map out the higher current densities at the rounded edge near the center of the sample to a greater detail. Current flowing in both directions are greater in magnitude and parallel to each other at this region, thus they would contribute more the denominator in Eq. 3.24. We were able to replicate the previous result by increasing the grid size in our calculations to roughly the same size in the previous calculation.

3.4 Telegraph-like Fluctuator Noise

Occasionally, if the fractional volume of a fluctuator is large enough, it is possible to observe individual fluctuators as discrete, telegraph-like fluctuator noise. Fluctuator noise can be studied to look for fluctuator interactions, track lifetimes and test to see

if the fluctuator activation is dominated by thermal or quantum processes. Also for TLS fluctuators it is possible to calculate the free energy difference between the states, ΔF, from the ratio r of time spent in each state, $r(T)$, from the Boltzman expression $r = e^{\Delta F/k_B T}$. The temperature derivative of ΔF then allows the calculation of the change in energy ΔU and the change in entropy $\Delta\sigma$, using standard thermodynamic relations. These thermodynamic variables, particularly entropy, can give insight into the physics behind the fluctuations. If $\Delta\sigma$ per unit volume is large, this would represent a fluctuation between different phases, while low values of $\Delta\sigma$ would mean fluctuations between qualitatively similar configurations. We use much of this latter analysis for telegraph-like noise that we have observed during our measurements.

Chapter 4

Fabrication and Measurement Techniques

4.1 Micro-fabrication

Pulsed Laser Deposition

YBCO and Ca-YBCO thin films were both grown on $LaAlO_3$ (LAO) substrates. LAO substrates are ideal for noise studies; Rajeswari *et al.*[81] have shown that LAO allows for the lowest excess noise at low-frequencies in YBCO thin films. The technique for growing the films is known as pulsed laser deposition (PLD). PLD involves ablating a target of the source material, in our case YBCO, with pulses of high intensity ultraviolet (UV) light. The impact of the pulses creates a stoichiometrically correct plume of YBCO that is deposited on a heated LAO substrate.

For YBCO films grown via PLD in the Dale Van Harlingen group at the University of Illinois we used a Lambda Physik Compex 301 excimer (excited dimer) laser. The laser was filled with a mixture of Ne, Ar, He and F gases to produce 193 nm UV light. Typical ablations used 350 mJ bursts at 3 Hz for growth rates of 2-3 Å per second. The laser beam is scanned over the YBCO target by using a scanning mirror in order to prevent burning a deep hole in the target and preclude stray scattering of the YBCO plume. The mirror is mounted on a gimbal mount and is scanned in the x and y directions using independent micrometer stepper motors. The beam is focussed with a lens down to a beam spot typically of 3 μm $\times$ 1 μm. The LAO substrate is attached using silver paint to an iconel (a steel alloy) substrate holder that sits in a water cooled base. The sample is heated using a quartz-Halogen light

bulb. Temperatures can reach as high as 1000°C at the center of the substrate holder. The initial films are grown close to optimal doping under higher oxygen pressures, typically at 820°C and $\sim$ 60mTorr of O_2. Subsequent annealing steps lowers the oxygen content and hence the T_c of the sample. Ca-YBCO films are grown by Tom Lemberger's group at Ohio State University. As part of the Ca-YBCO growth, targets with Pr instead of Y are used to grow insulating capping layers of PrBCO above and below the Ca-YBCO thin film. The doping in both YBCO and Ca-YBCO films is varied by oxygen concentration. Typical film thicknesses are approximately $25 - 35$ nm.

Lithography

Reducing the contact noise is important for noise studies. If the contact noise is too high, it can overwhelm the signal and prevent the extraction of the noise from resistance fluctuations. To reduce contact noise the contact area was ion-milled *in-situ* before gold was deposited. The ion mill is a standard dry etchant that uses accelerated Ar ions to mill away material, in effect an atomic sandblaster. Ion milling has the tendency to heat and damage the films which is problematic since heating cuprates in a vacuum can cause sample deterioration by the removal of oxygen. Therefore, in order to prevent heating, the sample is ion milled with low power on a liquid nitrogen cooled stage. We then use a brass shadow mask in order to mask the area of the film that will define the sample while exposing the areas that will define the contacts. Usually, 300 Å of Au are deposited for the contacts.

The samples were defined by using standard photolithography and ion milling. The photolithography involves spinning a thin layer of a polymer photoresist, a material which changes its properties when exposed to UV light allowing for it to be developed and removed by an alkaline solution. After application of the photoresist, it is baked for 1 minute at 110 °C. A photolithography mask made from soda-lime

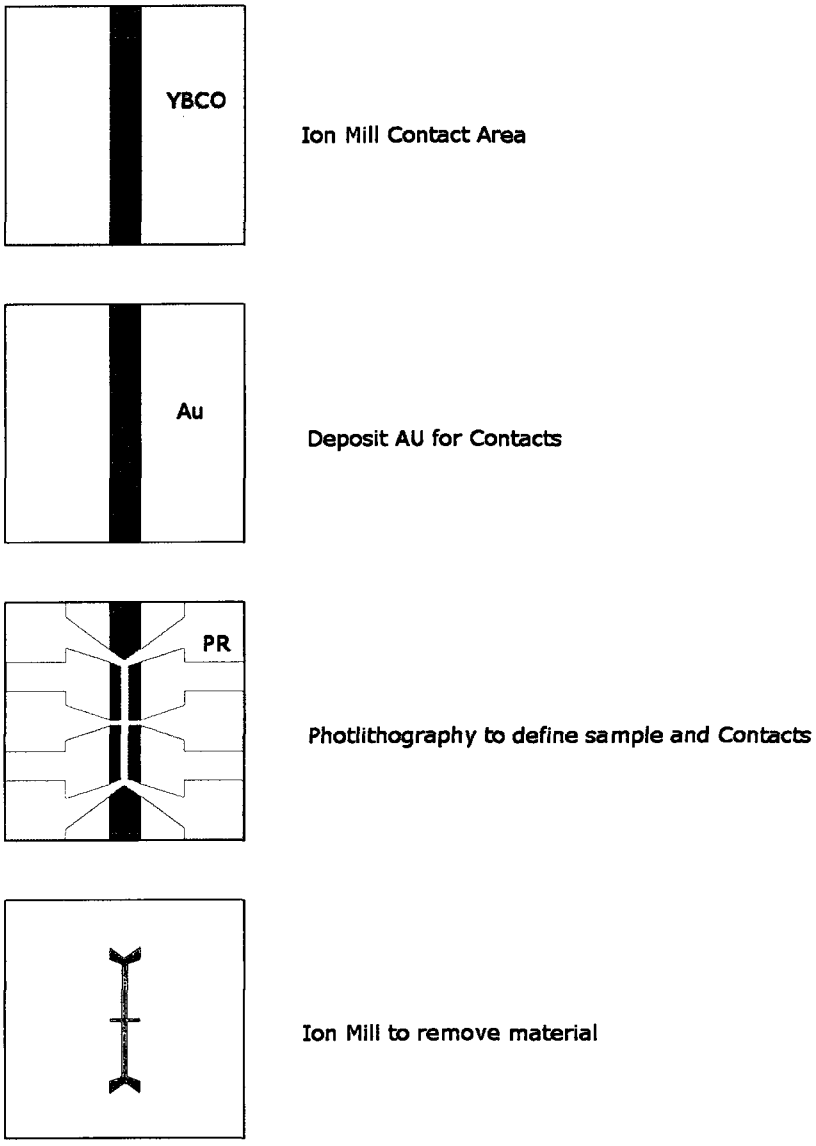

Figure 4.1: Top view of the lithography process. First the center of the sample is covered with a shadow mask while the rest is lightly ion-milled. Au is then deposited *in-situ*. Next photolithography defines the sample and finally ion milling removes excess material.

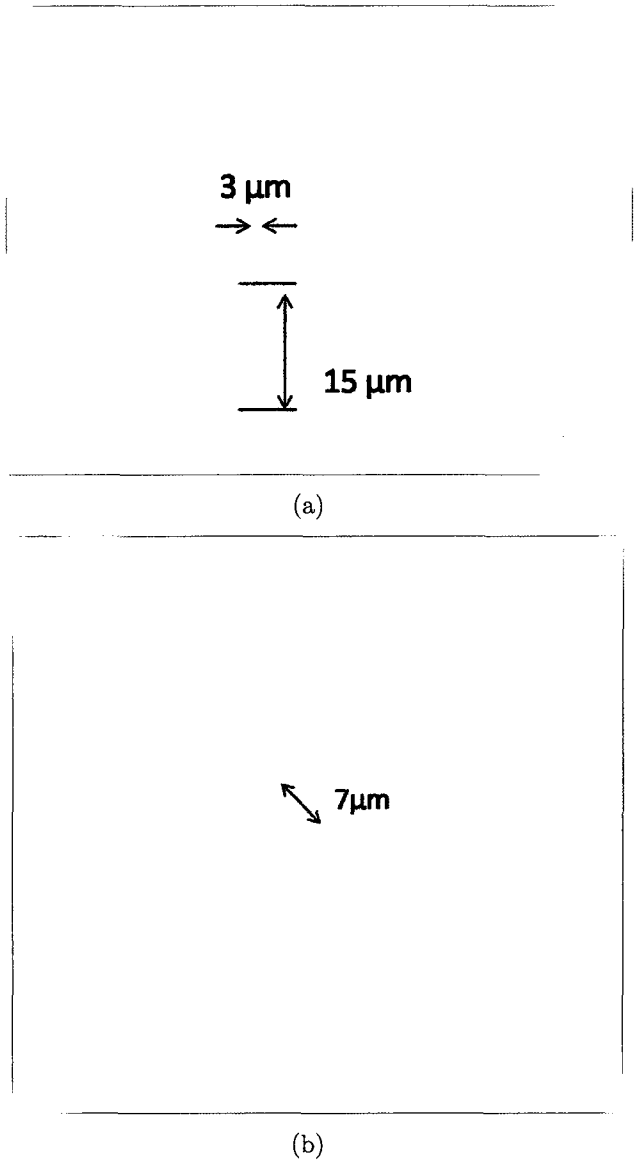

Figure 4.2: Optical microscope pictures of (a), a 3 μm wide wire used for measurements of the noise spectral power vs. frequency and temperature and (b), the sample used for isotropy measurements.

glass, with a pattern in iron-oxide that has the dimensions of the sample, is placed over the film. The pattern on the mask blocks the UV light from the areas that will define the sample. The resist on top of the film is exposed to UV light and developed. The remaining resist is then used as an ion-milling mask. The exposed material is then removed via ion-milling on a liquid nitrogen cooled stage. The final step is to remove the photoresist using acetone. A low power oxygen plasma is occasionally used if there is any organic residue left on the surface.

There were two types of samples fabricated for the work in this thesis. The first, for noise measurements, were usually in the form of 15μm long wires that are 2-3 μm wide. A typical wire sample can be seen in Fig. 4.2(a). The second type of sample used the special geometry for isotropy measurements shown in Fig. 4.2(b) and described in § 3.3. The final product for the isotropy measurements is an 8 probe sample with a central diameter of roughly 7 μm. Based on initial tests of the contact between YBCO and Au, the contact resistances between the Au and the cuprate should be $< 1\ \Omega$ for all samples.

4.2 Measurement Techniques

4.2.1 Technical Consideration

There are several experimental limiting factors for the measurement of resistance fluctuations, these include: 1) The current density must be high enough to maximize the voltage signal due to resistance fluctuations, but low enough to prevent electromigration or joule heating. A rough magnitude estimate for the maximum current density before this occurs is around $J = 10^6 \mathrm{A/cm}^2$. For a precise determination of the maximum current density there are two techniques used to detect joule heating. One technique is to check for linearity in voltage as a function of current. This can be done directly by ramping up the current until deviations from linearity in the

voltage begin. This is the technique that we used; the current was typically set up to maximum scale if there was no deviation from linearity. A second technique involves monitoring the noise amplitude to see if it scales as $V(T)^2$. When the power, as a function of applied current, scales greater than V^2 this can be an indication of heating.

2) Johnson noise, which is thermal noise proportional to the sample resistance and frequency independent, must be lower than the voltage noise due to the resistance fluctuations. The ratio of these two types of noise is determined by the current density. The size of the sample is important with respect to Johnson noise because it determines the maximum current density before heating begins.

3) The voltage noise of the input amplifier needs to be less than the voltage noise due to resistance fluctuations. Ideally, one should use a low-noise pre-amplifier that is optimal for the impedance of the sample. For low impedance samples bipolar based input amplifiers are optimal since they have low voltage noise. However, for higher impedance samples bipolar amplifiers can be a source of large current noise. In this case FET based amplifiers, which have greater voltage noise but much less current noise, are better.

4) A large source of noise are 60 Hz signals. These signals are nearly ubiquitous due to oscillating power lines that act as transmitters. The 60 Hz signal needs to be reduced before amplification of the voltage signal since it can dominate the ac voltage signal and prevent sufficient amplification of the measurement signal. Low frequency signals are difficult to prevent via shielding due to the large skin depth (over 8 mm in copper at 60 Hz). The reduction of 60 Hz noise before amplification is usually done with twisted pairs of wires. Twisted pairs of wires contain loops which pick up alternating signs of the magnetic flux due to 60 Hz noise, effectively canceling the signal. Finally, the setup requires proper grounding to prevent ground loops. Since two or more grounds in an electrical setup may be at different potentials, currents

may flow between them. Furthermore, such ground loops can act as antennaes that can pick up external electromagnetic noise.

5) Vibration isolation is required when using large magnetic fields. This is because excess noise can be picked up due to vibrating wires in a magnetic field

The resistance fluctuation noise usually falls off as 1/f which is a steeper rolloff than the frequency dependence of both types of background noise, Johnson noise and amplifier noise. Therefore, resistance fluctuation noise can only be measured in a window of lower frequencies before it intersects the background noise.

4.2.2 Experimental Setup

The series of measurements performed for this thesis required temperature control from below the transition temperatures of the samples (<30 K) up to room temperature ($\sim$ 300 K). This was achieved by using one of two different cryostats (vessels used in low-temperature physics measurements capable of attaining very low temperatures) depending on magnetic field requirements. For low field measurements (<2.5 kG), we used a Janis flow-through cryostat where the cooling is controlled by flowing the cryogen through the system, typically using liquid nitrogen as the cryogenic coolant. The system was cooled as liquid nitrogen passed through a copper stage to which the sample was thermally anchored. Using a needle valve we were able to set a constant flow of cryogen while the stage could be heated using a resistive heater attached to the sample stage. The sample stage sat within a vacuum can which was pumped out to prevent thermal conduction to the outside environment. An electromagnet straddled the vacuum can and was capable of attaining fields as high as 2.5 kG. We were able to vary the field direction with respect to the sample by rotating the sample stage. For high field measurements (up to 6 Tesla), we used a Janis helium flow-though cryostat. The cryostat had an external vacuum jacket as well as reflective superinsulation in order to prevent conductive and radiative heating

respectively. A reservoir within the system was filled with liquid helium in order to cool the superconducting magnet and serve as the cryogen to cool the sample. Similar to the previous cryostat, a needle valve controlled the flow of liquid helium, however the sample sat directly in the helium vapor. Heating in this system was also supplied by a resistive heater mounted on the sample stage.

Since resistivity noise can be highly sensitive to temperature, both temperature measurement and control were crucial to these experiments. Since certain thermometers can be affected by magnetic fields, for low and high field measurements we used a silicon diode thermometer and a Cernox^{TM} thermometer respectively. The thermometers were physically clamped to the sample stage while the samples were attached to the stage with conducting thermal grease to ensure good thermal contact. The temperature was monitored using a Lakeshore 340 temperature bridge. The same temperature bridge set the temperature by using a PID (a generic control loop feedback algorithm) which controlled the power output to the heater resistor. Temperature stability was typically less than ± 10 mK (the main limitation in temperature measurement was the digitization of the thermometer voltage) and the temperature could be swept at rates from 0.1 K/min to 10 K/min. The temperature was recorded by sending an analog signal that corresponded to the sample temperature to the ADC (analog to digital converter)that was then recorded by a computer.

A constant dc current of up to 450 μA, was provided by a battery with a series resistor of roughly 100 times the resistance of the sample. The raw ac voltage signal was first amplified by a Stanford Research SR552 low-noise amplifier at 40 dB (or a factor of 100; x dB of gain corresponds to voltage amplification by a factor of $10^{\frac{x}{20}}$). Subsequently, the signal was sent through a Stanford Research SR640 anti-aliasing filter with a corner frequency of less than half of the sampling frequency. The SR640 then further amplified the signal, usually by another 40-80 dB, before it was digitized by an NI 6143 ADC converter and recorded by a computer running Labview software.

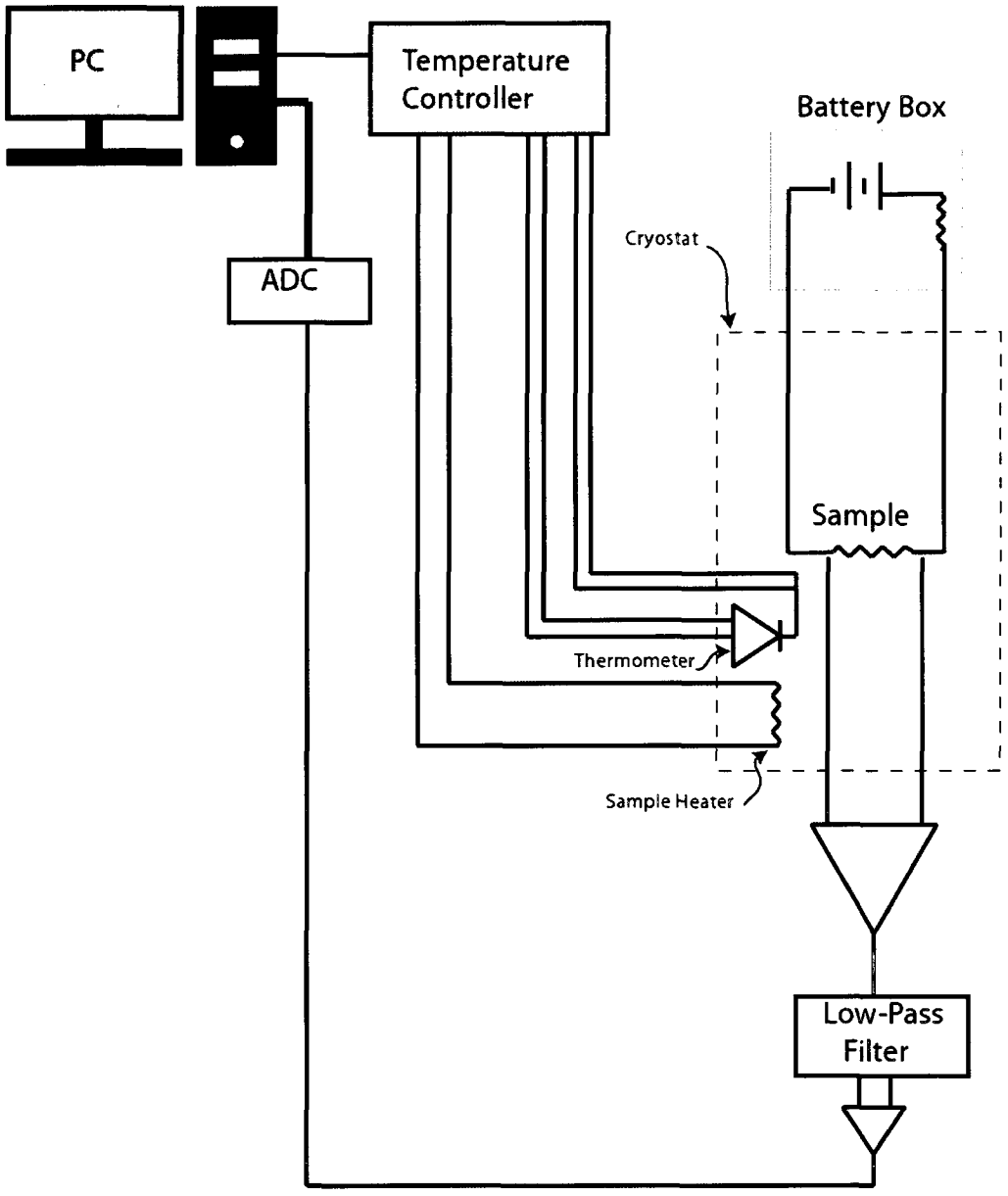

Figure 4.3: Schematic of the experimental setup for transport noise measurements

The dc voltage was also recorded in order to monitor the resistance of the sample. We also measure a background signal, with no current flowing, in order to measure the noise that is due to other sources than the resistance fluctuations. The sampling rate was usually 200-300 Hz.

4.2.3 Data Analysis

The raw voltage data is then analyzed using Matlab software which performs FFTs (fast Fourier transforms) in order to get the raw voltage power spectrum. Octave sums, O_i, are then performed over the power spectra of V(t), the Voltage time trace, by summing over successive doublings of the frequency

$$O_i^k = \sum_{f_i<n<2f_i} P_n^k. \tag{4.1}$$

These octave sums are useful because they compact and average the noise spectra. There is also the advantage advantage of displaying roughly the same noise power per octave. The normalized resistance power spectra, $S_R(T)/R(T)^2$ are calculated by first subtracting the background noise spectra from the voltage power spectra and subsequently dividing by the square of the resistance.

Isotropy Analysis

Several measurement steps are necessary in order to calculate the isotropy sensitive parameter Q (Eq. 3.21) for the sample in Fig. 3.2. We calculate the numerator of Q, $\langle(\delta R_C)^2\rangle$, by flowing current in the A direction while measuring voltage in the orthogonal B direction and taking the power spectrum of the voltage data:

$$\langle(\delta R_C)^2\rangle = FFT^*(V_B(t)) \cdot FFT(V_B(t)). \tag{4.2}$$

By Onsager reciprocity we can obtain the same value by flowing current in the B direction and measuring the voltage in the A direction in order to obtain further statistics on the parameter Q. In order to obtain the denominator from Eq. 3.21, we first need to measure the cross spectrum $\chi_{AB}(\omega)$. The measurement involves flowing current and measuring the voltage in both the positive A and B direction (from A1 to A2 and from B1 to B2) and taking the cross spectrum:

$$\begin{aligned}\chi_{A_+B_+}(\omega) &= FFT^*(V_A(t)) \cdot FFT(V_B(t)) \\ &= \langle \delta R_A \delta R_B \rangle + \langle (\delta R_C)^2 \rangle + \langle \delta R_C \rangle \langle \delta R_A \delta R_B \rangle\end{aligned} \tag{4.3}$$

We would like to remove the extra, final term in $\chi_{A_+B_+}(\omega)$. To do so we flow current in the opposite direction of one of the leads to obtain $\chi_{A_+B_-}$ and subtract it from $\chi_{A_+B_+}(\omega)$. This result gives us the denominator of Q,

$$\frac{1}{2}(\chi_{A_+B_+}(\omega) - \chi_{A_+B_-}(\omega)) = \langle \delta R_A \delta R_B \rangle + \langle (\delta R_C)^2 \rangle. \tag{4.4}$$

For each of these measurements, it is necessary to subtract the power spectrum and cross spectrum of the background signal (with no current flowing). The Matlab code for calculating the isotropy parameter from the raw V(t) data, which uses the same techniques of analysis for the S_R(T) and field dependent measurements in the wires, can be seen in Appendix A.1.

Chapter 5

Results

The noise analysis used in this thesis [1] is based almost entirely on the power spectra of resistance fluctuations. Figure 5.1(a) illustrates the power spectra for various temperatures as a function of frequency. Each spectrum displays a characteristic 1/f rolloff. As mentioned in the previous chapter, it is convenient to average and compact the data over successive doublings of frequency into octave sums. The octave sums for the three spectra in Fig. 5.1(a) are shown in Figs. 5.1 (b), (c) and (d). For pure 1/f noise, similar to Fig. 5.1(c), there is an equal power density in each octave. For $1/f^{\alpha}$ noise, where $\alpha > 1$, the lower octaves display a higher amplitude while the opposite is true for $\alpha < 1$. All of the frequency dependent (as opposed to time dependent) noise data shown in this chapter are displayed in terms of octave sums. The magnitude of all measurements displayed are normalized for sample volume as discussed in § 3.2. The amplitude of the normalized noise power in our experiments is similar to previous results for YBCO on LAO [81].

5.1 Fluctuation Isotropy Measurements

5.1.1 Experimental Results

The isotropy measurements were performed over one sample with a T_c of 58K patterned into the geometry shown in Fig. 4.2(b). All measurements used a current of 450 μA. Raw data ,$V_A(t)$ and $V_B(t)$ for the A and B directions respectively, was

[1] Many of the results and discussion found in this chapter can also be found in reference [82].

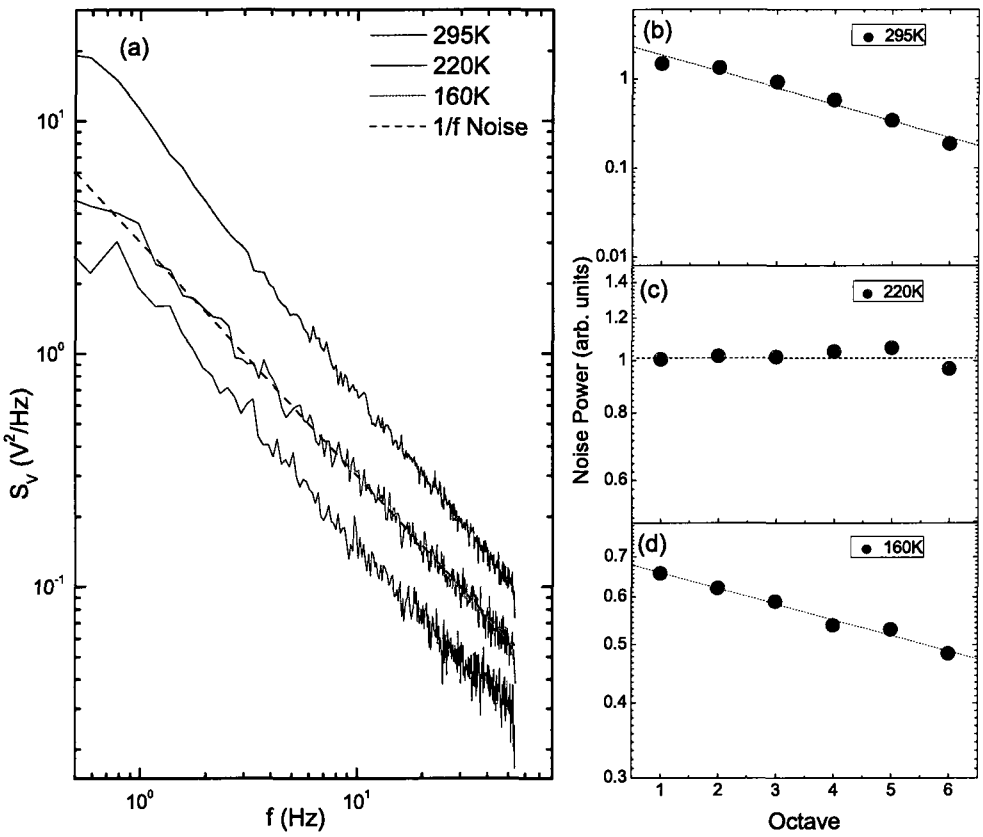

Figure 5.1: (a) The power spectra at 3 different temperatures for the sample with T_c = 58 K indicating a $1/f^{\alpha}$ dependence. A 1/f fit, with $\alpha = 1$, is plotted along with the power spectrum at T=220 K. (b) Noise power vs octave for T=295 K. The downward slope of the power per octave indicates that $\alpha > 1$ for this temperature. (c) Noise power vs octave for T=220 K. An octave independent spectral power indicates pure 1/f noise ($\alpha = 1$) (c) Noise power vs octave for T=160 K

recorded and analyzed as described in the previous chapter.

The data were always of the form $S(f,T) \propto 1/f^{\alpha}$ and we never saw any discrete fluctuations for this geometry, which would show up as Lorentzian bumps in the spectra. If fluctuations were due to unidirectional stripe orientation fluctuations, one would expect a traceless isotropy parameter, S = -1. Scalar fluctuations, which one would expect for amplitude fluctuations i.e. growing and shrinking local bubbles of uniformly varying resistivity, would give a value of S = 1. The results of the isotropy parameter S(f,T) over 4 octaves for temperatures ranging from 160 K to 295 K are shown in Fig. 5.2. We found that the isotropy parameter of the sample clustered around S = 0 for all temperatures. This seems to indicate that over the frequency range of our measurements, the noise is not traceless and therefore not due to rotations of resistively asymmetrical regions in a symmetrical environment as hypothesized in [70] and [83]. We observe, however, that the isotropy parameter appears to pick up some variations below $\approx$ 200 K. As we will show later in this chapter, an extra noise source appears around this temperature for our frequency range.

5.2 Thermodynamic Properties of the Spectral Noise Power

When measuring $S(f,T)$ for the isotropy sample, we discovered an anomalous excess noise that appears below about 230K for the frequency range of our experiment. Figure 5.3 shows the $S(f,T)$ for the highest doped sample that we measured with a T_c of 85 K. This sample is representative of many of the temperature and magnetic phenomena which turn on at lower temperatures: 1) There is an excess noise beginning below 230K, larger in magnitude than what would be expected by extrapolating down from the high temperature noise. 2) The strong peak just above T = 100 K is a Lorentzian feature due to an individual fluctuator which acts as a telegraph-like noise

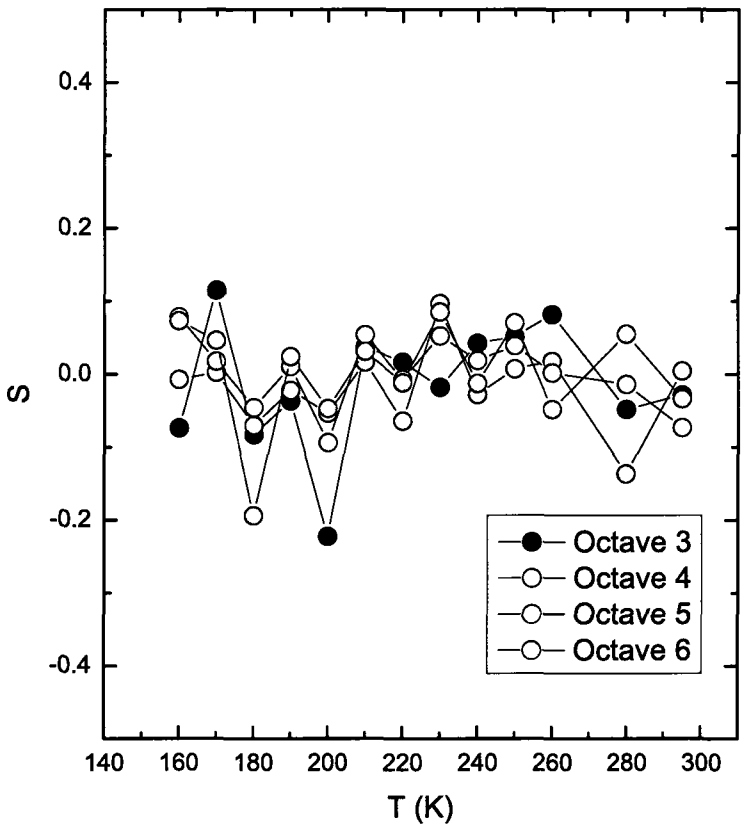

Figure 5.2: The isotropy parameter, S, measured for a sample with T_c=58 K. The data shown is for 4 octaves measured from 160K to 295K. The error is at most ± 0.05 for the higher octaves and ± 0.10 for the lower octaves

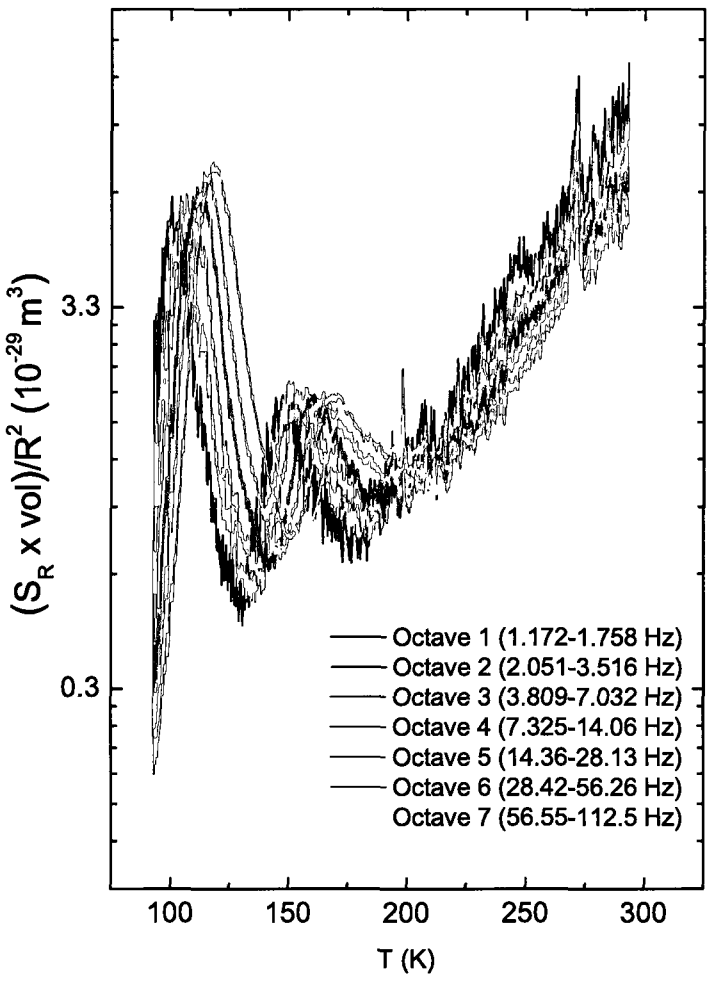

Figure 5.3: The spectral noise power as a function of temperature shown for all 7 octaves recorded. The sample had a T_c of 85 and dT/dt=0.3 K/min.

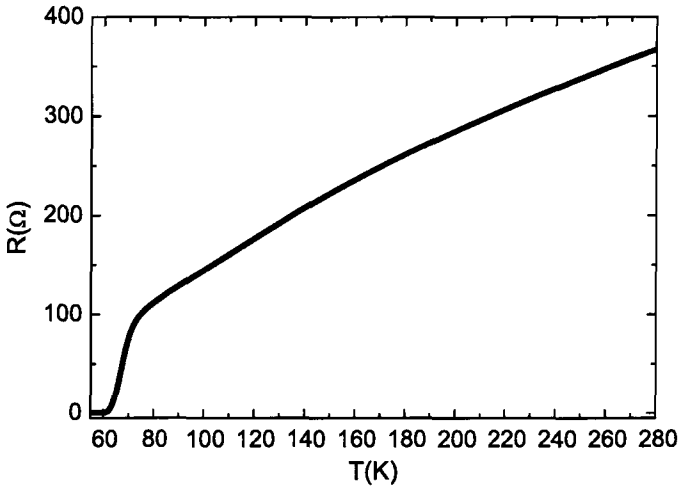

Figure 5.4: R(T) for a sample with a T_c of 65K. The noise of this sample is shown in Fig. 5.5(a). R(T) is smooth and there is no indication of any macroscopic resistance changes in the vicinity of the temperature at which an excess noise signal begins.

source. Further discussion on the dynamics of these fluctuators can be found in § 5.3. 3) A permanent change in the temperature dependent spectra occurred within this sample in between temperature sweeps and is discussed in § 5.2.1. 4) This sample displayed peculiar low magnetic field sensitivity (for applied fields below 2 kG). These results are displayed in § 5.2.2. The only measurement type that is not represented by this sample are the measurements of noise dependence on high field (up to 7.5 Tesla). These measurements, however, were performed on a pair of other samples and these data are shown in § 5.2.3.

5.2.1 Temperature Dependence

Figure 5.5(a) shows the T-dependent octave sums (normalized by R^2) for the sample with a T_c of 58K. Subtracting the extrapolated high-temperature noise power leaves an asymmetrical peak, whose peak temperature we define as $T_p(f)$. We discovered this peak in every subsequent sample that we measured.

In order to determine the nature of the excess noise, we studied the frequency dependence of the peak. The frequency dependence of $T_p(f)$ can be seen in Fig. 5.6(a). We fit the temperature dependence of the $T_p(f)$ to the Arrhenius relation

$$f_p = f_0 e^{\Delta E/k_B T} \tag{5.1}$$

(see Fig. 5.5(b)) where f_p is the peak frequency, f_0 is the attempt rate and ΔE is the barrier height. We discovered that the activation of this feature is determined by thermally activated kinetics, with a typical attempt rate of $f_0 \sim 10^{10} - 10^{11}$ Hz and an activation energy of $E_a = 0.40 \pm 0.02eV$. Arrhenius kinetics means that the activation of the underlying fluctuators is similar to what would be expected of an ensemble of TLS with relatively little temperature dependence on the barrier height. If the kinetics in Fig 5.5(b) were in fact determined by a steeper slope vs. temperature than the Arrhenius temperature dependence, this would suggest some sort of glass (a state characterized by frustrated interactions and many accessible metastable states) or phase transition. Thus $T_p(f)$ gives no indication that there is a genuine phase or glass transition in this vicinity, just a rather sharp increase (compared to many other Arrhenius, thermally activated features which are relatively broader as seen in [77]) to a maximum component of a distribution of activation energies. A rough estimation of this distribution is easily calculated by dividing $S(f,T)$ of the peak by T^2 (see Fig. 5.7).

We have observed this feature in the noise power for every sample measured: 13 samples patterned on 6 separate thin films. A plot of $S_R(T)$ for each distinct sample can be seen in Fig. 5.8. There were 7 distinct samples due to the fact that one inhomogeneous YBCO film produced two differently doped samples with T_c's of 38 K and 72 K. These also include two samples patterned from a Ca-YBCO film grown by Tom Lemberger's group at Ohio State University.

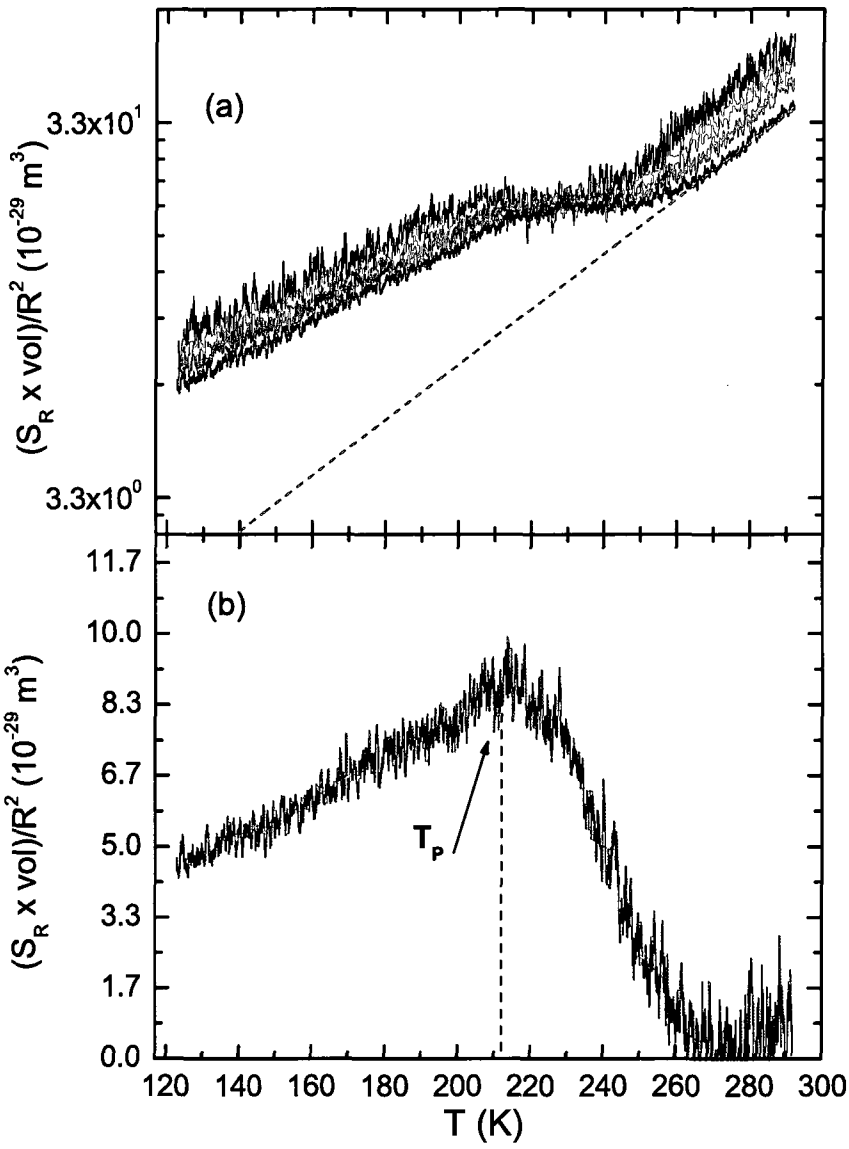

Figure 5.5: Noise spectral power in a YBCO sample with T_c=58K. The temperature is swept at 0.3 K/min. Panel (a) shows the temperature dependent noise power over 4 octaves. (b) We subtract the amplitude from the high temperature noise, extrapolated exponentially to lower temperatures, to show a peak in the noise. The temperature T_p is the maximum of this noise feature which characterizes the onset of the excess noise.

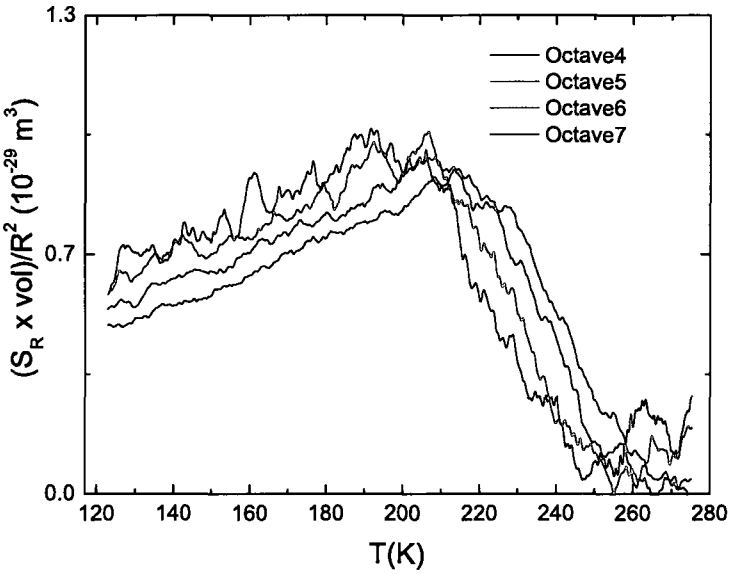

(a)

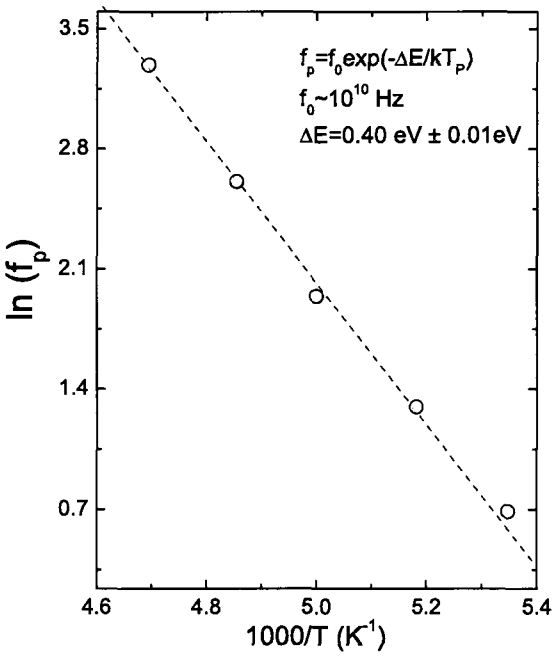

(b)

Figure 5.6: (a) The spread of peaks of different octave for the sample with T_c=58 K.(b) The Arrhenius fit (Eq. 5.1) of the various frequencies, f_p, to the peak temperatures, T_p.

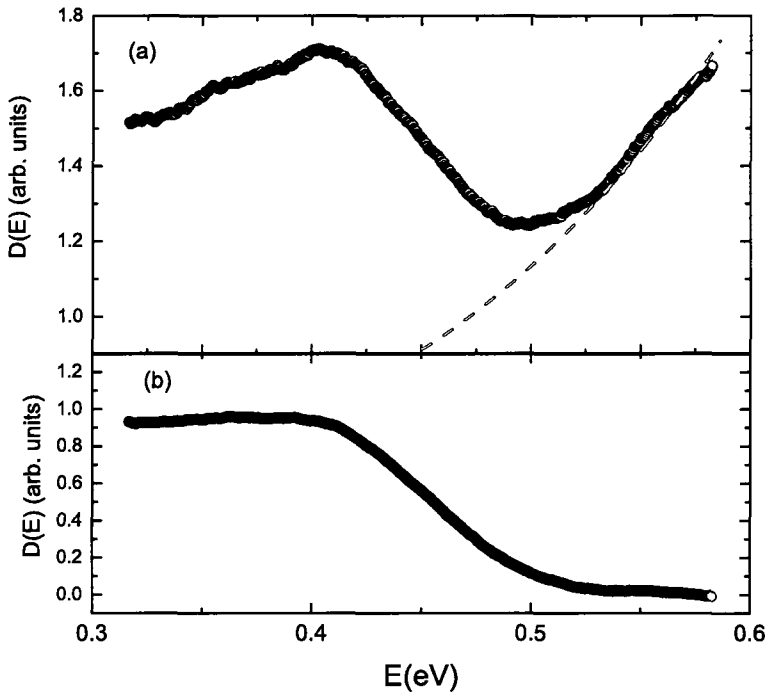

Figure 5.7: (a) The approximate distribution of activation energies for a sample with a T_c of 58 K. (b) We subtract a background contribution to estimate the distribution of activation energies that contributes to the peak feature in Fig. 5.5(b).

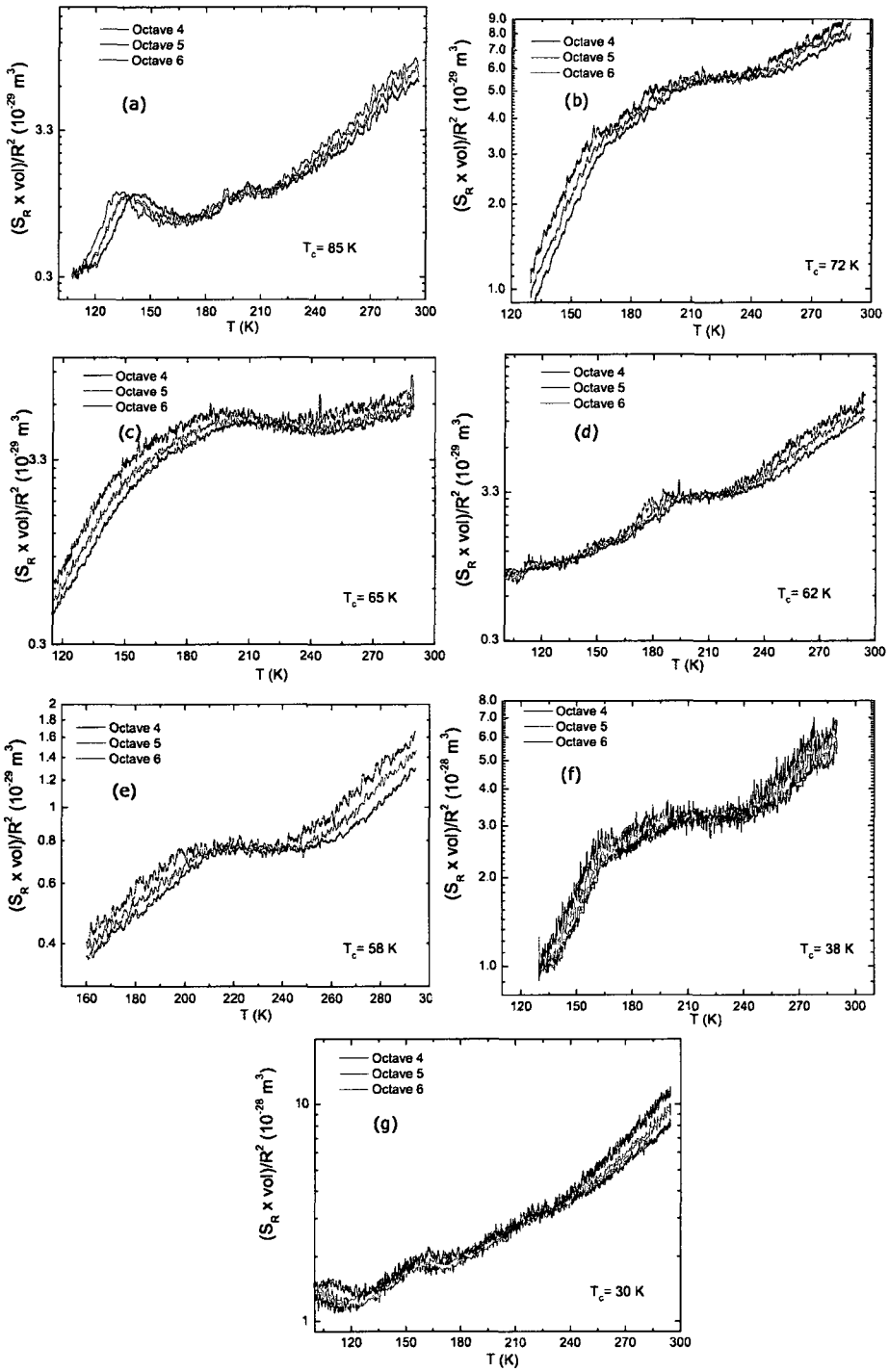

Figure 5.8: $S_R(T)$ over three octaves for every distinct sample.

Dutta Horn Analysis

For every distinct sample we calculated both sides of the Dutta-Horn equation given in Eq. 3.10. Both the spectral exponent, α, from the left hand side of Eq. 3.10 and the prediction of α from the temperature dependence of Eq. 3.10 are shown. The interesting feature in α is where it dips to $\alpha \sim 1$. This occurs due to the sum of two or more distributions of activation energies where the total distribution flattens out. As discussed in § 3.2.1, $\alpha = 1$ whenever there is a uniform distribution of activation energies. The results for a selection of 6 differently doped samples seen in Figs. 5.9(a)-(f) show temperature dependent deviations from Dutta-Horn. As a reference, a 0.1 difference between predicted and measured α can be significant since it represents roughly an increase by $\sim T^{2.5}$ above what one would expect in the spectral power density. These results do not show any systematic doping dependence in the variation from Dutta-Horn. For example, over a wide range of temperatures, Fig. 5.9(a) shows good agreement with the Dutta Horn equation while Figs. 5.9(b), (d), (f) show roughly a constant deviation from Dutta-Horn. However, with the exception of one of the samples with T_c=72K the data shows an increase of the deviation from Dutta-Horn in the vicinity of the dip in α. The possible relationship of this slight deviation in Dutta-Horn to other noise features that also appear to turn on in this temperature range will be discussed in the following chapter.

Doping Dependence

There are several intriguing doping dependent properties in the observed noise. Firstly, for a given frequency, the location of the peak T_p is roughly doping independent. In order to determine the maximum value, T_p and spread, ΔT_p, we perform a gaussian fit on the higher temperature section of the peaks . Two other peaks, for a Ca-YBCO sample with T_c of 62 K and a YBCO sample with T_c of 72 K can be seen in Figs. 5.10 and 5.11 respectively. The table of values for T_p and the spread ΔT_p as a function

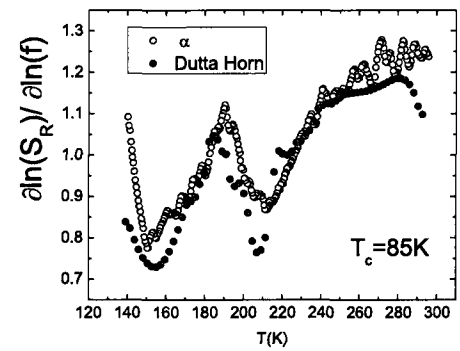

(a)

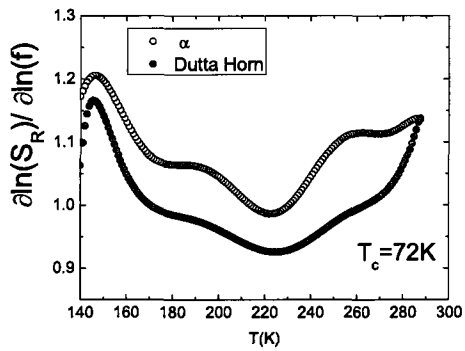

(b)

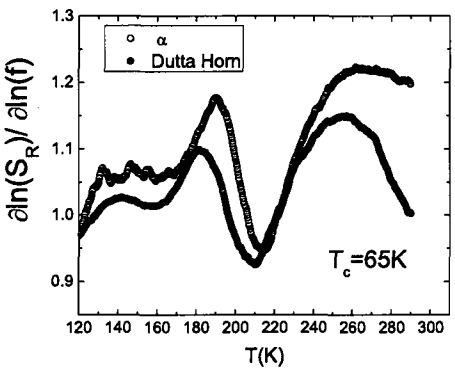

(c)

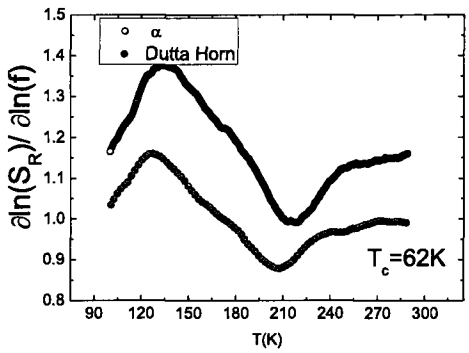

(d)

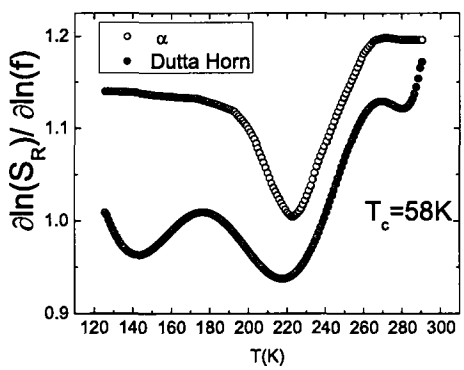

(e)

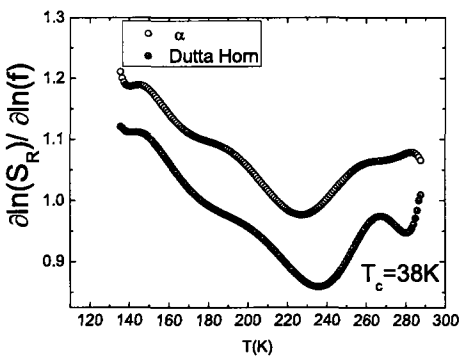

(f)

Figure 5.9: α and the Dutta Horn prediction of α for a sample of T_c's.

of sample T_c can be seen in table 5.1. In the sample with the lowest T_c, there is no clear single peak, only the onset of excess noise; here the value of T_p is a rough estimate based on the location of the maximum this excess noise. In several cases, such as in Fig. 5.11(b), it appears that there is more than one peak in the underlying distribution of activation energies.

Table 5.1: Values of T_p and the spread of the peak ΔT_p for every distinct sample.

T_c(K)	30	38	58	62	65	72	85
T_p(K)	213	204	217	201	197	199	204
ΔT_p(K)	45	48	52	71	42	71	41

While the location T_p is doping independent, the amplitude of the noise, both above the peak and at the peak change as a function of doping. Figure 5.12 displays both the peak amplitude and the noise amplitude (at 280 K) above the peak as a function of the sample T_c. The amplitude of the noise at temperatures higher than T_p shows a drastic change in its doping dependence as doping is varied from optimally doped to underdoped. For the four distinct samples at higher doping, there is little dependence on the higher temperature noise. This changes drastically for the two lower doping samples. Interestingly, in between these separate doping dependencies is where a gradual decrease in the structural anisotropy between the a and b lattice parameter begins. Figure 1.3(a) shows how a and b lattice parameters converge to the same value as YBCO becomes less orthorhombic at $T_c \approx 53$ K and becomes fully tetragonal at $T_c \approx 28$ K. Furthermore, these values would be shifted to lower temperatures for the Ca-YBCO samples since they contain less oxygen, the addition of which eventually causes the structural change. In contrast, the peak amplitude displays strong doping dependence throughout the phase diagram. Figure 5.12 shows

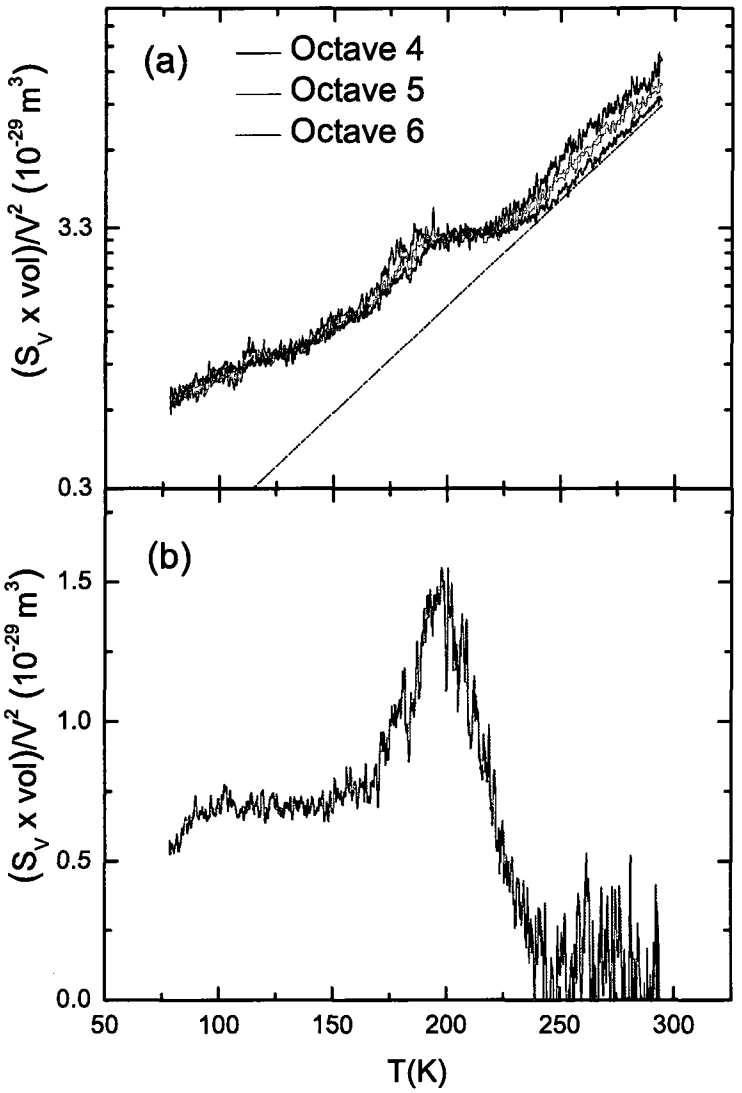

Figure 5.10: Noise spectral power in a Ca-YBCO sample with T_c=65K, dT/dt=0.3 K/min. Panel (a) shows the temperature dependent Noise power over 3 octaves. (b) The peak in the underlying noise after subtracting the higher temperature noise source extrapolated to lower temperatures

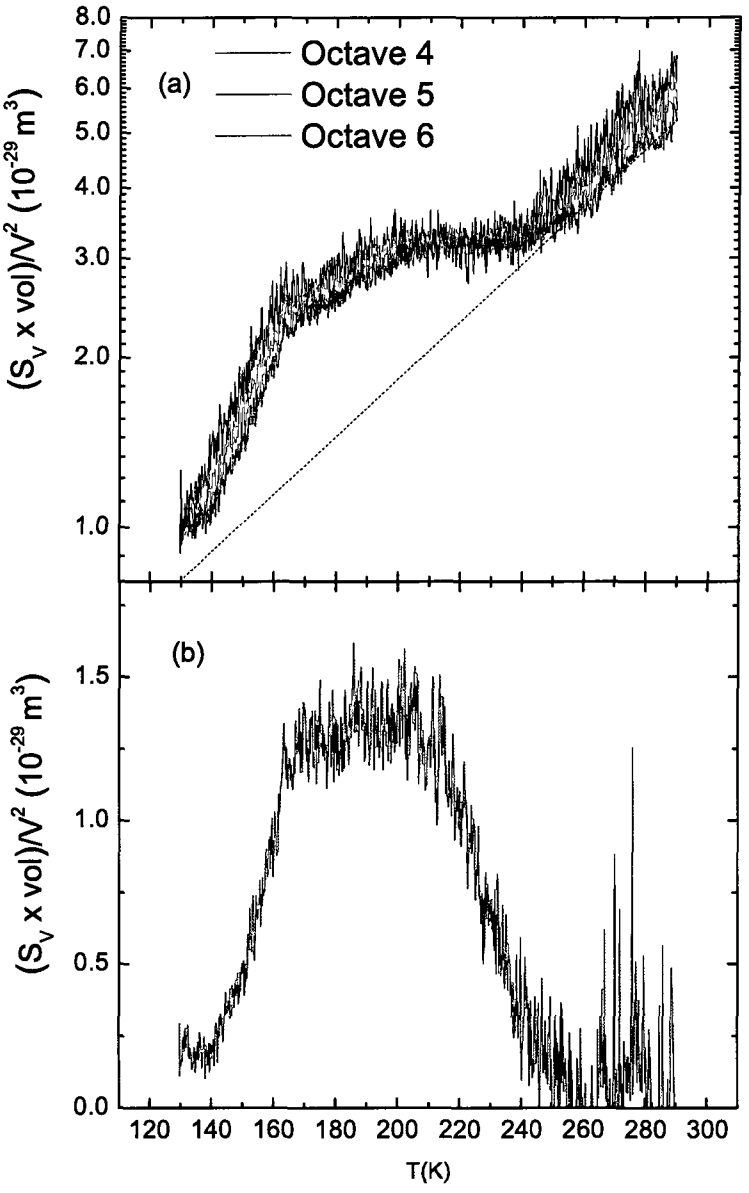

Figure 5.11: Noise spectral power in a YBCO sample with T_c=72K, dT/dt=0.3 K/min. Panel (a) shows the temperature dependent Noise power over 3 octaves. (b) The peak in the underlying noise after subtracting the higher temperature noise source extrapolated to lower temperatures

an exponential increase in the amplitude; the peak amplitude changes almost 2 orders of magnitude from the highest doped sample with a T_c of 85 K to the lowest doped sample with a T_c of 30K. The lone exception is a Ca-YBCO sample with a T_c of 62 K which has both lower amplitudes than what would be expected, probably due to a thicker sample than expected, for both the peak noise and the higher temperature noise. The possible relevance of the doping dependence (or lack thereof) will be discussed in the following chapter.

Sample Change

In a pair of samples near optimal doping with $T_c = 85$ K, a permanent change in the temperature dependent spectra occurred in between temperature cycles. Despite this permanent change in the noise as a function of T, there was no accompanying change in the resistance of the sample. Unfortunately, we were not able to see if there was a change in T_c since the change occurred after the initial measurement of T_c. Similar to other effects that turn on in the noise, these changes in noise occured below approximately 230 K. Figure 5.13 shows the change in the 6th and 7th octaves for one of these 2 samples. The relative change for both samples that changed is shown in Fig. 5.14. While the change in noise power was significant below about 230 K, the higher temperature noise did not change from its initial value. The two samples measured here were patterned from the same film and were separated by approximately 15 μm. Since the bulk resistance did not change and the change in noise measured is due to local fluctuations within each sample, this suggests that the change in the noise power was due to a change in the underlying fluctuations that extended, at least partially, over both samples.

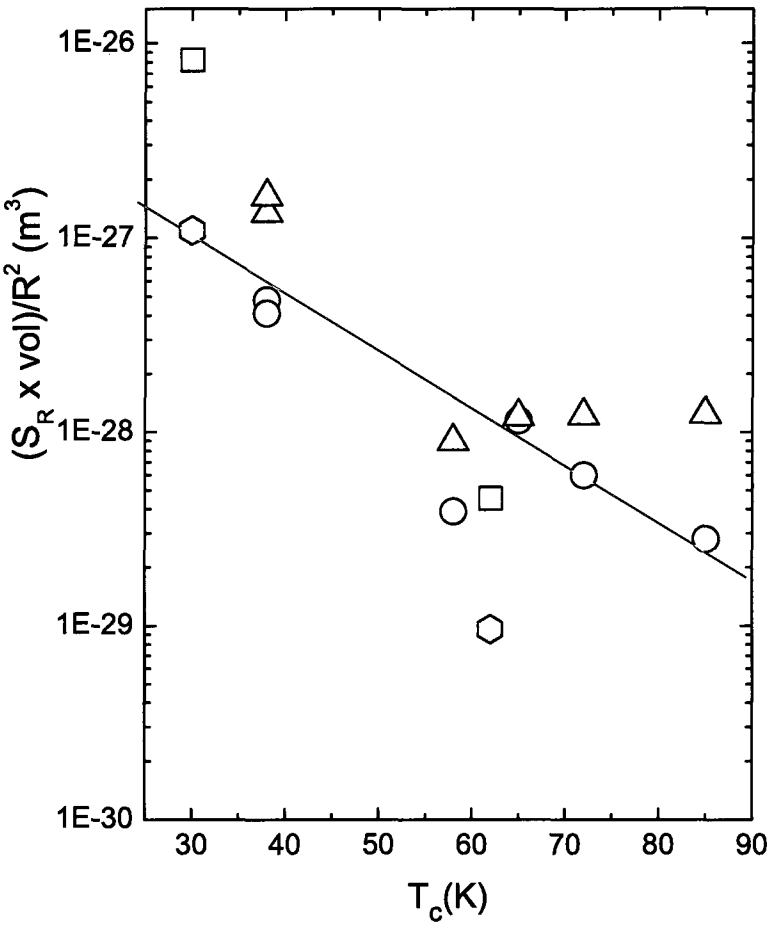

Figure 5.12: Noise power amplitude as a function of sample T_c for the higher temperature noise at T=280 K for YBCO (blue triangles) and Ca-YBCO (blue squares) samples. Also shown is the noise power amplitude vs T_c at the peak for YBCO (red circles) and Ca-YBCO (red hexagons) samples. The noise power is normalized for the sample volumes. One of the Ca-YBCO samples (T_c = 30 K) followed the trend of all the other samples while one (T_c=62 K) was clearly as an outlier for both the peak amplitude and higher temperature noise trends. The red line is used as a guide for the eye.

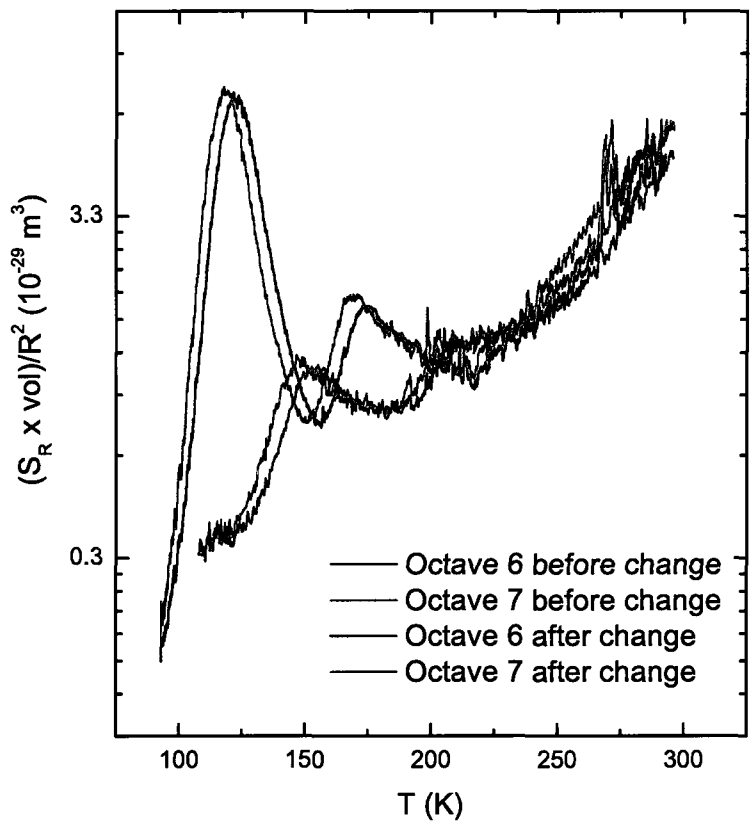

Figure 5.13: Change in noise power for a sample with T_c=85 K shown over two octaves. There was no evidence for a change in the bulk resistance

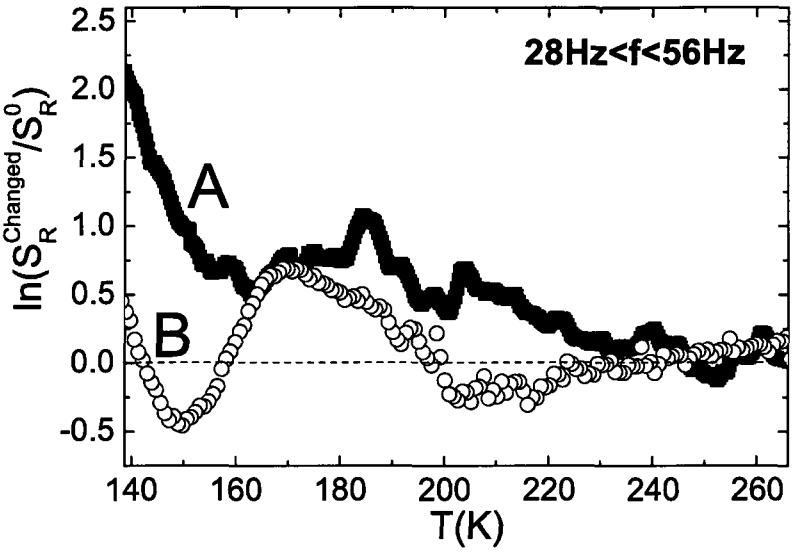

Figure 5.14: Relative change in noise for two samples (sample A shown in Fig. 5.13) grown from the same film with T_c=85 K. The samples were separated by 15 μm.

5.2.2 Low Field Noise Measurements

We have observed evidence of a magnetic dependence in the noise of several of the samples. Both low field measurements (H $\leq$ 1.5 kG = 0.15 Tesla) and high field measurements (up to 7.5 Tesla) show magnetic effects of the noise, each with a distinct dependence. We begin by discussing the low-field noise which we observed only in one sample. We observed an unexpected sensitivity to low in-plane fields in both of the samples patterned on a film with T_c = 85 K (see Fig. 5.3) in the vicinity of T_p and only before they experienced a spectral change. After the spectral change occurred, shown in Fig. 5.13, the noise in both samples lost its low-field dependence. By measuring the noise with no current and the magnetic field on, we did not see a large enough signal from microphonics (noise due to mechanical vibrations of the lead wires in a magnetic field which would also track with the magnetic field) that would cause the level of observed magnetically sensitive noise.

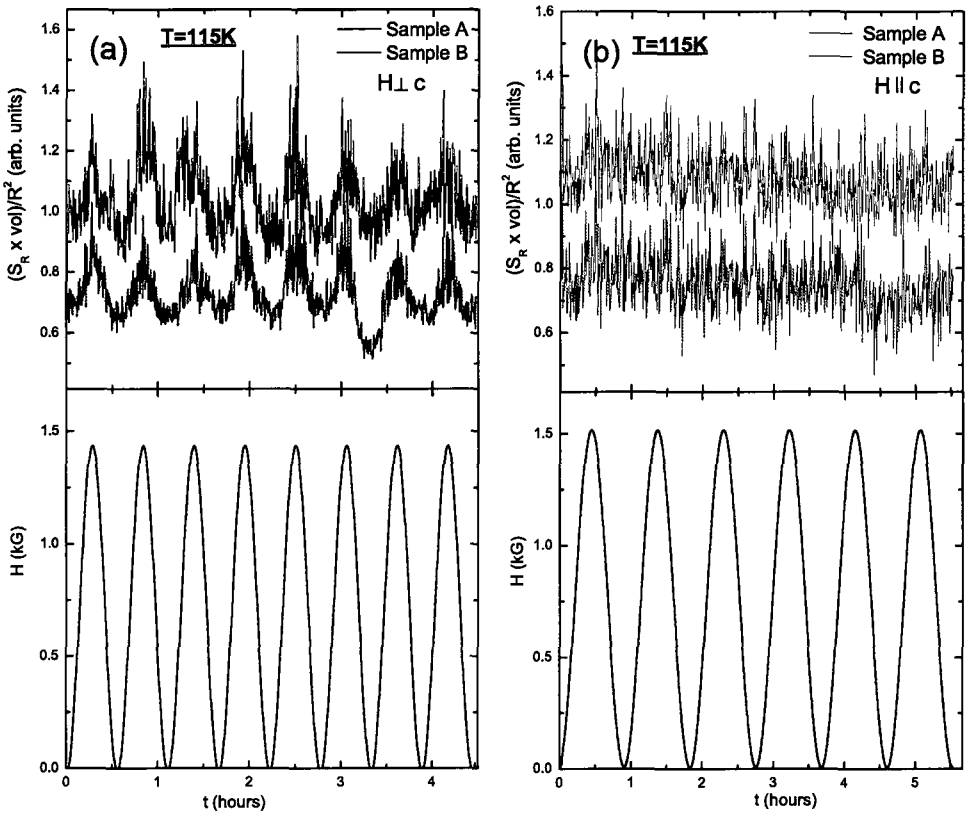

Figure 5.15: (a) Response of the noise to the in-plane low magnetic field for two samples with T_c=85K at 115 K. The lower panel shows the magnetic field as a function of time, while the upper panel shows the noise response of two samples to the magnetic field. (b) No response to the magnetic field is observed when the field is perpendicular to the plane.

The experimental technique involved sinusoidally sweeping the magnetic field at very low frequencies ($< 5 \times 10^{-4}$ Hz) from 0 to 1.5 kG and observing the spectral dependence of the noise. All of the data shown is for the noise dependence in the 7th octave centered at 80 Hz. The data shown is for two samples patterned from the same film. The samples were in series, sharing the same current path and separated by 15 μm. Since the noise power from both samples often had similar magnitudes, the data was shifted in order to differentiate the results, hence the y axis is displayed as noise power in arbitrary units (though on the order of 10^{-29} m^3). Figure 5.15 shows the field dependence of the noise at 115 K for orientations of the field both in the plane and perpendicular to the plane (parallel to the c axis). Clearly, there is a field dependence on the noise when the field is in the plane shown in Fig. 5.15(a) as the noise in both samples tracks the field sweep and increases in magnitude by greater than 20%. Interestingly, the noise in sample B drops to a lower noise state for half a period (just after 3.5 hours) indicative of the underlying fluctuations moving to a new local minimum, before it tracks back to the original noise level after the subsequent increase in field. A similar meandering between local minima in a complicated energy landscape, as may be expected, is more prominent at higher temperature data. For all of the data that shows a response to the low magnetic fields, there are two components to the noise: one that slowly tracks the magnetic field, and another component (that occasionally seems to be driven by the field amplitude) that sporadically jumps to a higher noise state. As temperature increases, the former dependence appears to decrease while the latter increases. Furthermore, the sporadic changes in noise for samples A and B occur independently. This indicates that the source of the noise is neither due to changes in the current nor is it spatially extended over both samples.

For the in-plane field data at 127 K, shown in Fig. 5.16, the sample noise continues to track the magnetic field. For two maxima in the field amplitude, sample A clearly jumps up to a higher noise value. In fact for the second jump noise, it temporarily

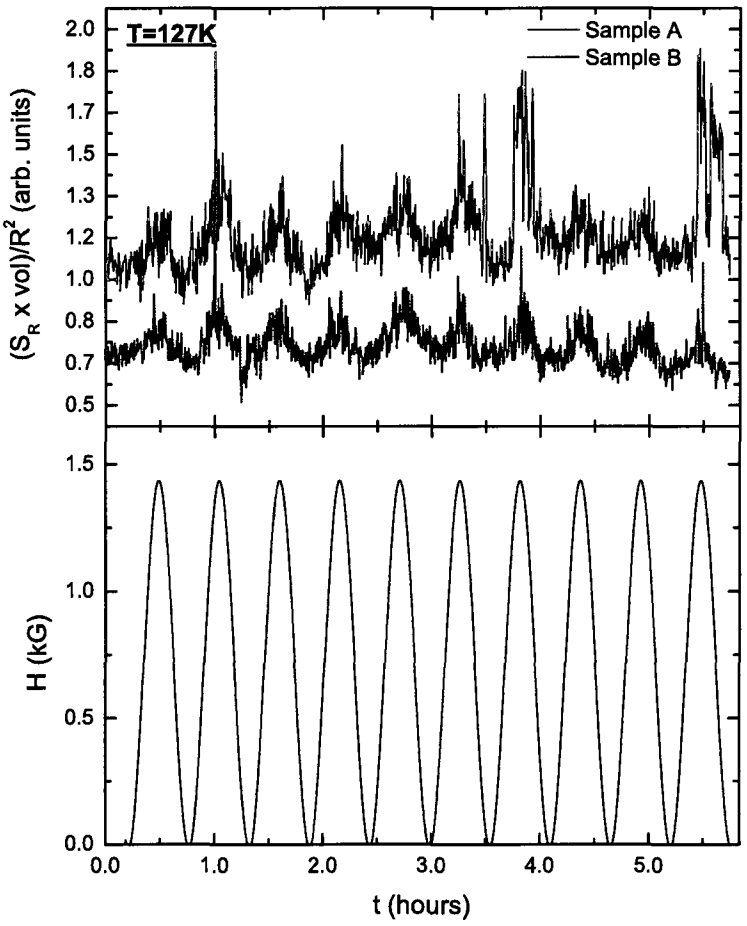

Figure 5.16: Response of the noise to the in-plane low magnetic field for two samples with T_c=85K at 127 K.

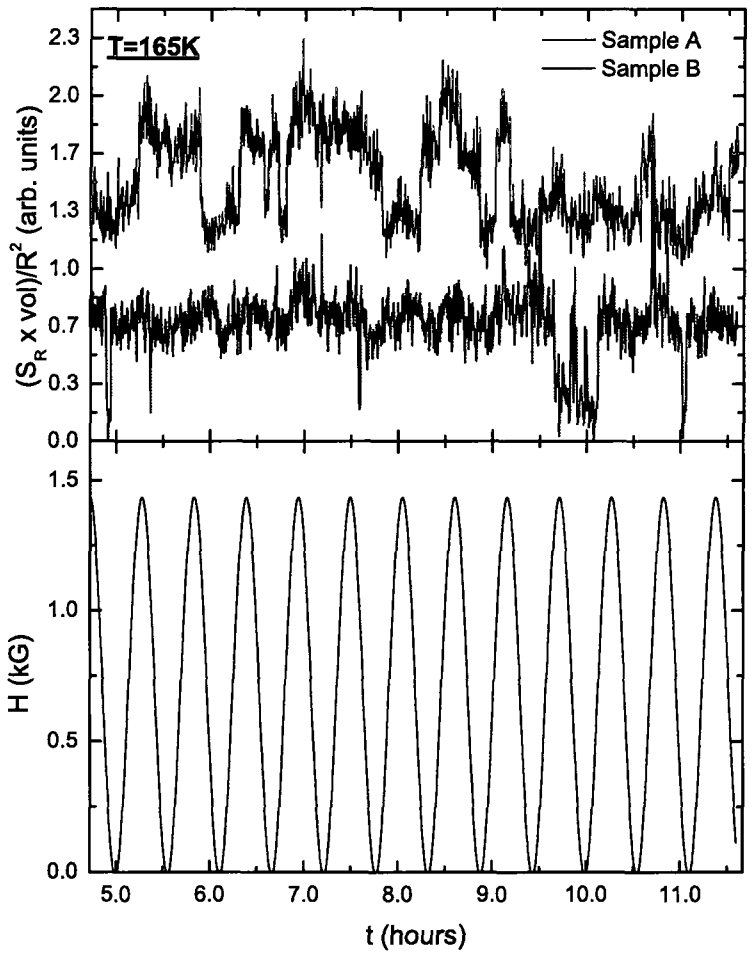

Figure 5.17: Response of the noise to the in-plane low magnetic field for two samples with T_c=85K at 165 K.

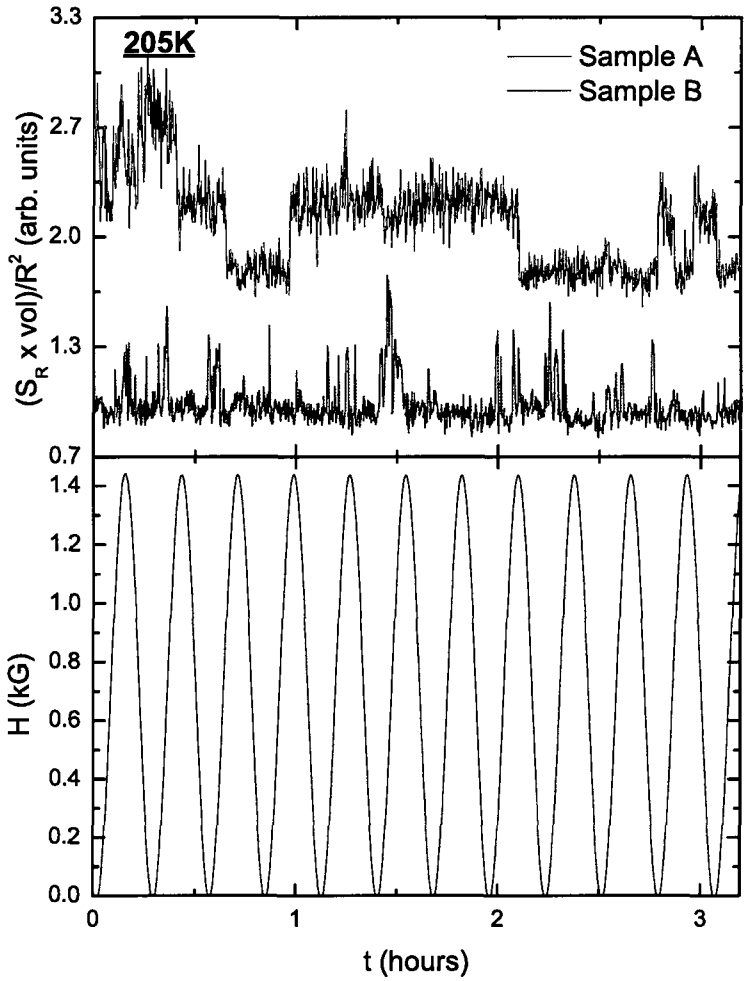

Figure 5.18: Response of the noise to the in-plane low magnetic field for two samples with T_c=85K at 205 K.

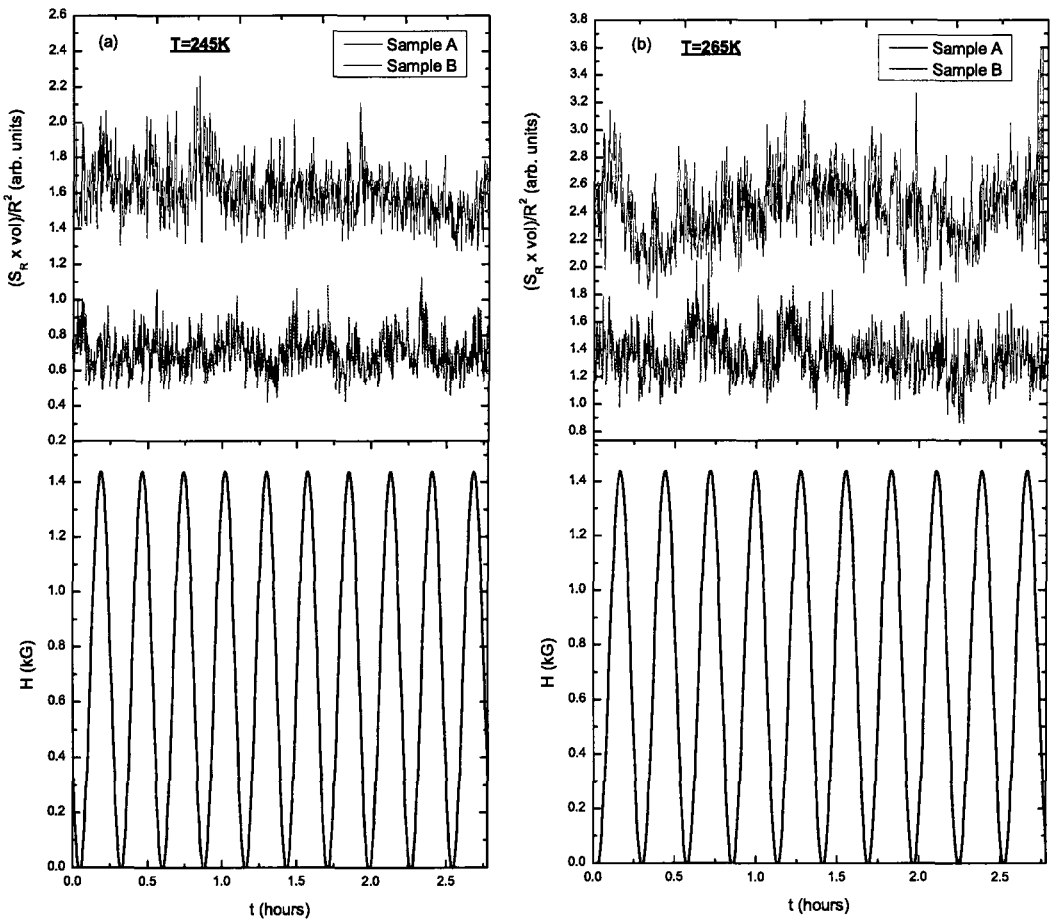

Figure 5.19: Response of the noise to the in-plane low magnetic field for two samples with T_c=85K at (a) 245 K and (b) 265K. No response is observed at these temperatures.

falls back to the same value as most of the other peaks before jumping back up to the excited noise value. This trend continues for the measurement at T = 165 K (Fig. 5.17). There is a drop in the amplitude of the noise that tracks the magnetic field while the amplitude of the jumps increases. At T = 165 K, sample B drops several times to a lower noise power. Even more dramatically, sample A displays several jumps to higher power that last from one to several oscillations of the magnetic field before falling back down. At T=205 K, shown in Fig. 5.18, there is a much reduced noise response in both samples that tracks with the field, however, the amplitude of the jumps increases in Sample A. Furthermore, there are more than two metastable noise states in Sample A at this temperature and it appears that the jumps correlate with the maxima in the magnetic field. In sample B, there are no jumps in noise that extend in time as much as in sample A, however, the frequency of jumps increases.

This striking in-plane magnetic noise response disappeared at higher temperatures. Figure 5.19 shows a lack of the magnetic in-plane response of the noise at 245 K and 265 K. Unfortunately, the low-field magnetic response disappeared after the subsequent cool-down of the sample for measuring T_c as mentioned earlier; this change in the magnetic response happened in conjunction with a permanent change in the noise power shown in Fig. 5.14.

5.2.3 High Field Noise Measurements

We measured a high magnetic field dependence ($H > 6$ T) of the noise in both YBCO and Ca-YBCO samples, and observed a complicated magnetic sensitivity. Figure 5.20 shows an example of the noise sensitivity at 160K. The data, displayed for the 6th octave, begins before any field is applied. It is then ramped up to 6.3 T with the field perpendicular to the plane of the sample causing an increase in the noise magnitude by about 6%. After the field was removed, we observed no immediate change in the noise power. It was only after subsequent cycling of the temperature that we observed

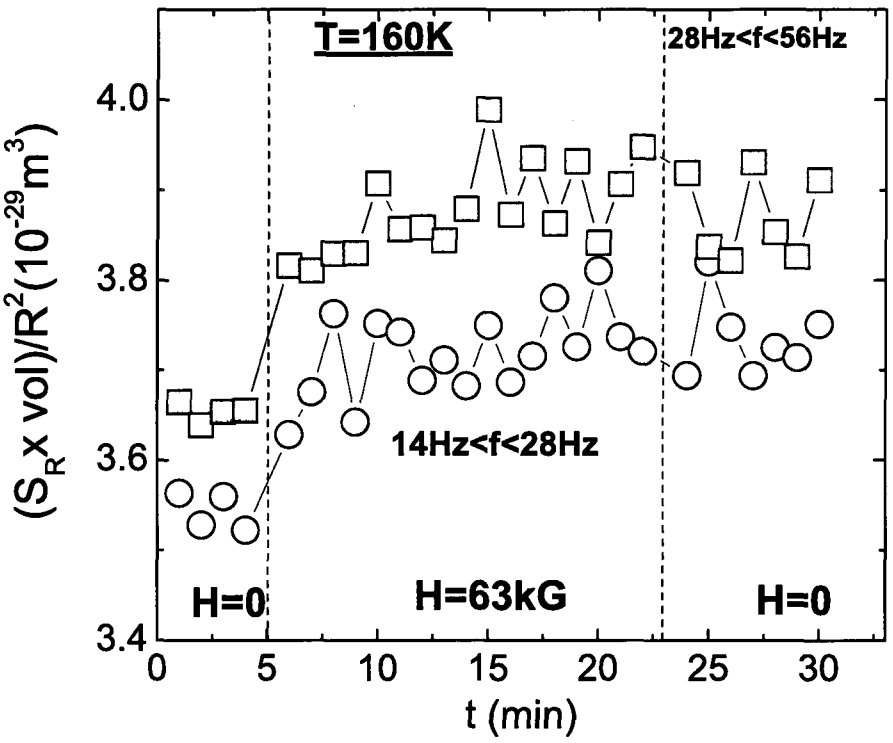

Figure 5.20: The noise power of a Ca-YBCO sample with T_c=62 before during and after the application of 6.3 T, $H \parallel c$.

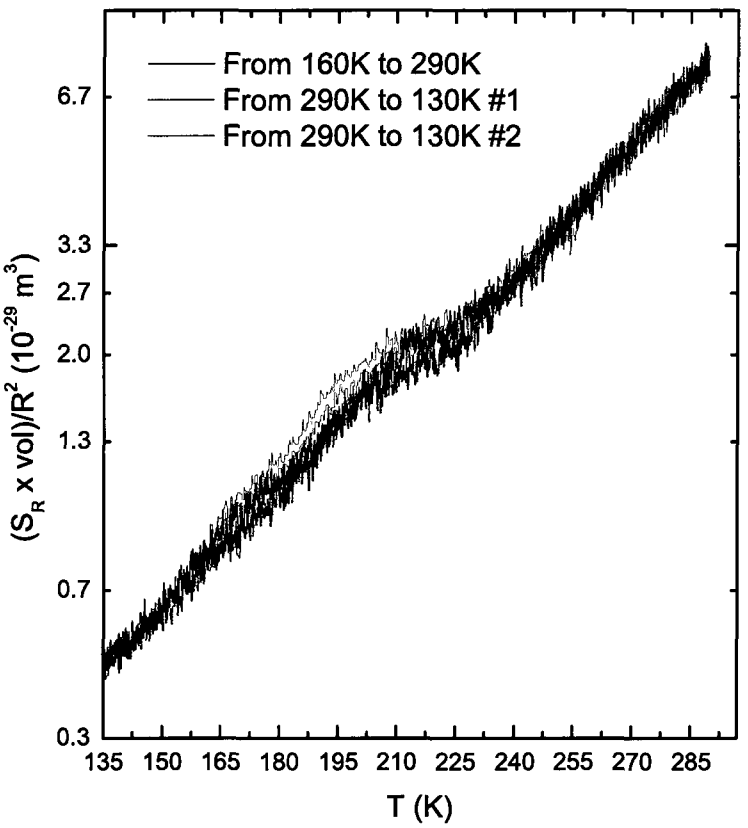

Figure 5.21: Gradual noise power relaxation after the removal of the magnetic field.

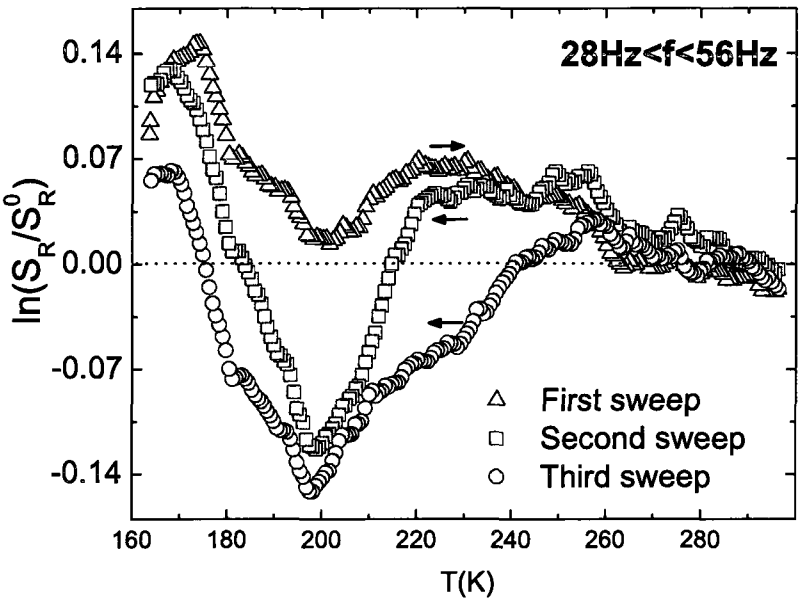

Figure 5.22: Log of the ratio of noise power to pre field value during 3 consecutive thermal cycles after the removal of the 6.3 T field, H|| c.

a gradual relaxation of the noise power. The slow relaxation of the noise power is shown in Fig. 5.21. This relaxation was measured over three temperature sweeps which lasted 18 hours. The relaxation of the noise with respect to the initial noise, $S_R^0(T)$, before the field was applied, is shown in Fig. 5.22. A similar excitation, for a field of 7.5 T ($H \parallel c$), and long relaxation over subsequent temperature sweeps was recorded in a YBCO sample with a T_c of 72 K; this relaxation is shown in Fig. 5.23. The key feature that we notice in both cases is that in the change in the noise power, both in response to the field and over time, become negligible above approximately 250 K. Hence, the magnetic dependence in both the low and high field measurements appears to be associated with the onset of the excess noise.

Surprisingly, when the field was applied parallel to the plane of the sample, such as in the low field measurements, there was no change in the noise power. Figure 5.24 shows the temperature sweeps of the noise after applying a 7.5 T field parallel to

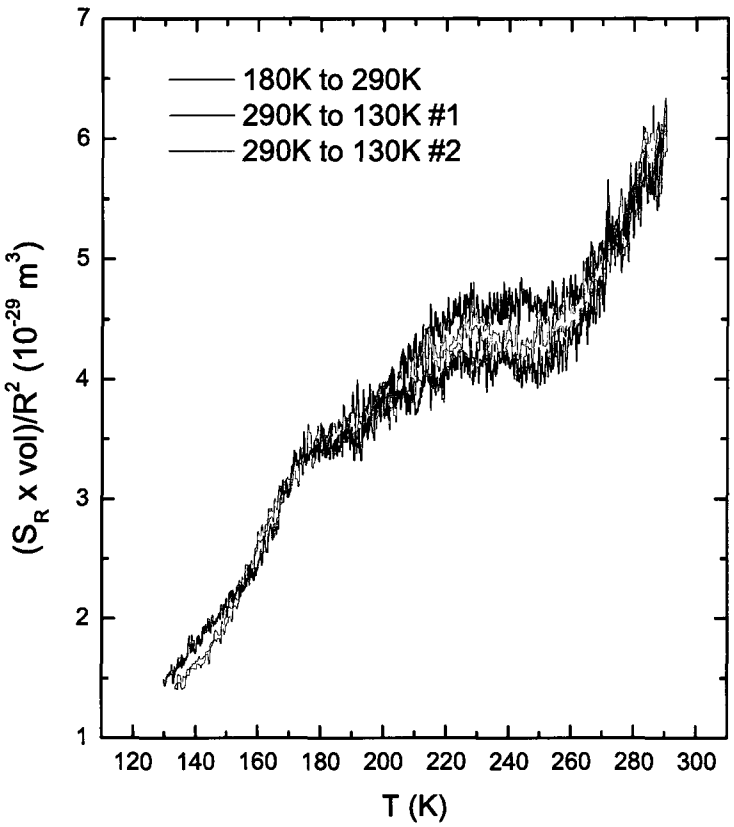

Figure 5.23: Gradual noise power relaxation after the removal of a 7.5 T magnetic field, H|| c. YBCO sample with a T_c of 72 K

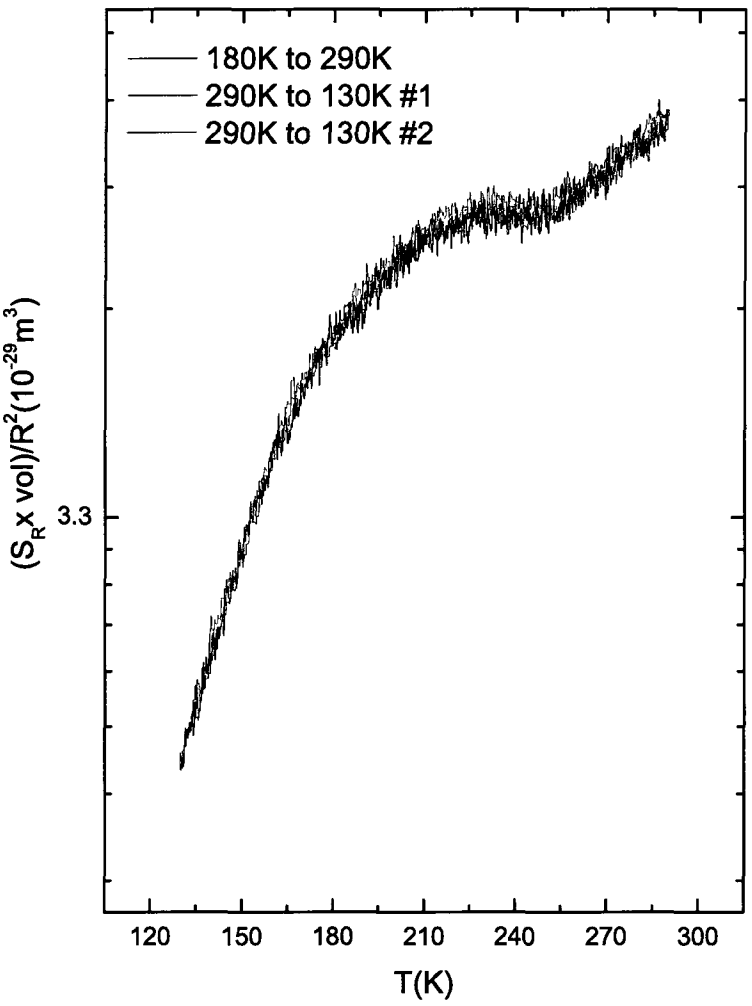

Figure 5.24: Noise response after applying and removing a 7.5 T field, H$\perp$ c.

the sample. Figure 5.25 records the response of the noise as a function of time before during and after the application of a 7.5 T field and subsequently the application and removal of -7.5 T.

We were able to see a strong response in the noise when the field was applied perpendicular to the plane. Furthermore, we observed a frequency dependent response for the application of field in opposite directions. When the positive field was applied, the higher octaves showed a stronger response (shown in Fig. 5.26). The jump in the noise power did not occur until the field had already been on for about 15 minutes and the high level of noise lasted for more than 100 minutes after the field was removed. However, when the negative field was applied, the response was larger in the 5th octave than in the two higher ones. This could indicate that these represent two different fluctuating regions, or the dynamics of the region had changed between the positive and negative field application.

When the negative field was applied, the increase in noise for all octaves appeared to track the increase and decrease in the magnetic field. After the field was removed, the noise level fell back down. With the field off, it then returned to the excited noise value for a few hundred seconds before returning to the original noise level. This further indicates the complicated magnetic dependence of the noise. Taken as a whole, the low field noise dependence is indicative of glassy behavior where the low energy fluctuations are meandering though a complicated distribution of metastable states.

5.3 Fluctuator Noise

Below 200 K we frequently saw the onset of large, temperature dependent individual fluctuators (see Figs. 5.28 and 5.29), mostly of the two-state form. These fluctuators show activated kinetics, as one would expect for a TLS, with attempt rates

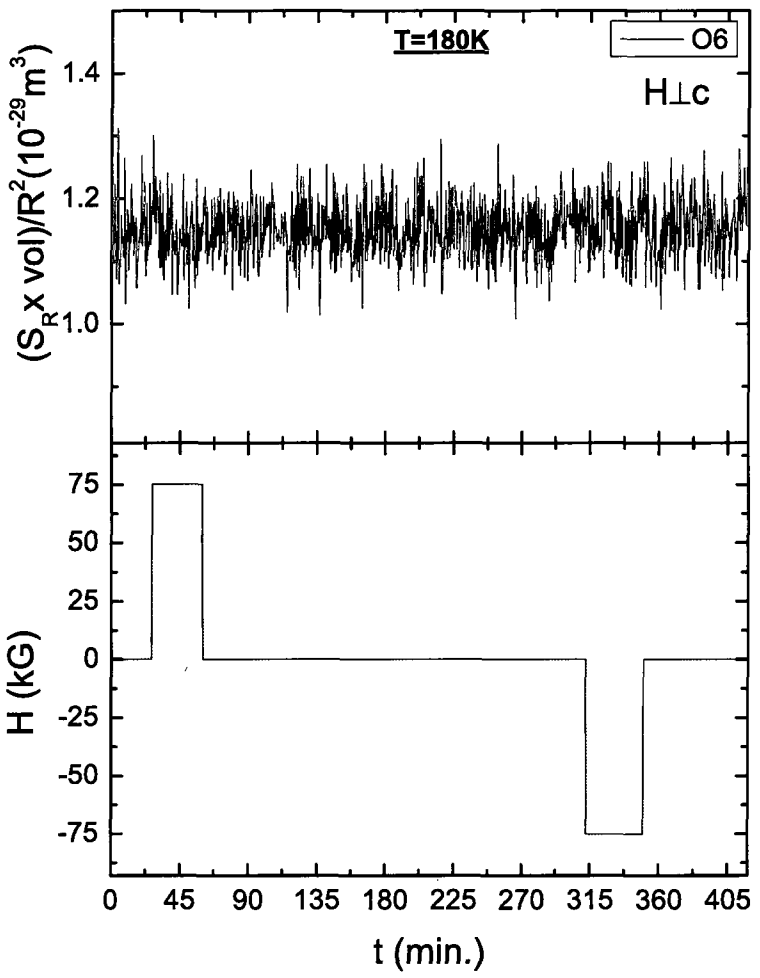

Figure 5.25: The top panel is the response of the noise to magnetic field, H⊥c, shown in the bottom panel.

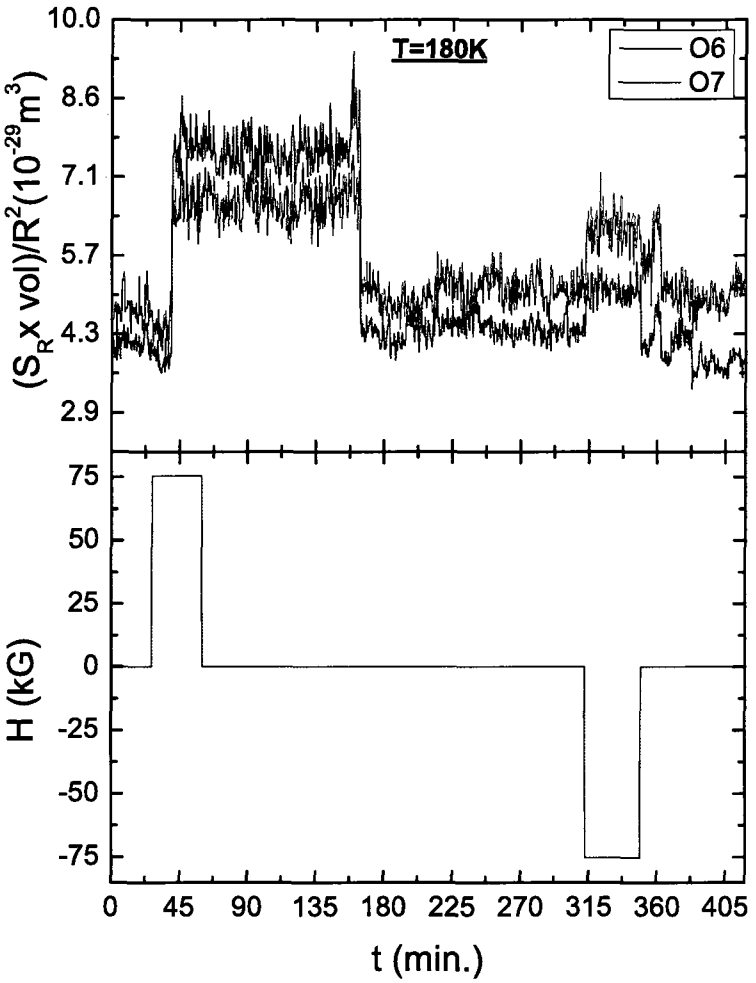

Figure 5.26: Response of the 6th and 7th octave noise (top panel) to magnetic field, H$\|$c, shown in the bottom panel.

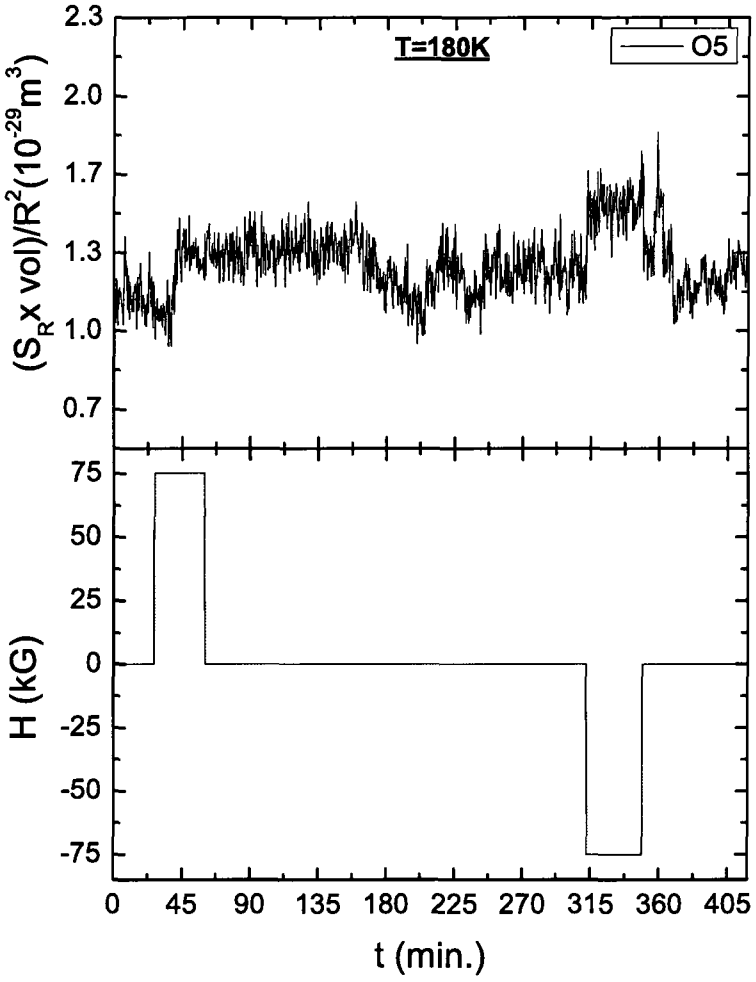

Figure 5.27: Response of the 5th octave noise (top panel) to magnetic field, H||c, shown in the bottom panel.

of about 10^{10} Hz and therefore activation energies, set by our frequency window, of about $20k_BT$. In all 13 samples, many on multiple temperature sweeps, we found no discrete fluctuators above 200 K. The observation of discrete switching of the noise provides some compelling information on the nature of the underlying fluctuations. The switches in resistance of these discrete fluctuators represent fractional fluctuations in the resistance of $\delta R/R > 10^{-5}$. Assuming a symmetry breaking noise mechanism that would not have a local resistive anisotropy greater than a factor of 2 (as shown in [68] and Fig. 2.11), $\delta R/R > 10^{-5}$ corresponds to a fluctuator volume of at least 10^{-5} of the sample volume. Since the sample volume is approximately 10^{-12} cm^3 this makes the minimum fluctuator volume 10^{-17} cm^3. We can then compare this to the size of a fluctuator volume expected due to changes in scattering due to the motion of small defects. To estimate this effective volume, we multiply the point scatter cross section by the mean free path of the carriers. In YBCO, the Debye screening distance (the distance over which carriers screen out electric fields) is much longer than in typical metals [84] so the screening is limited by the Fermi wavelength. Based on a carrier density of $n \approx 10^{21}$ cm^{-3}, we can then estimate the Fermi wavelength, λ_F, from $\lambda_F = 2^{3/2}(\pi/3n)^{1/3}$ which gives approximately 3 nm. This gives an effective scattering cross section of $\sim 10^{-14}$ cm^2. The mean free path above 90 K in YBCO is less than 10 nm, this makes the effective scattering volume to be less than 10^{-20} cm^3. Therefore the size of the fluctuations that we see are at least 3 orders of magnitude larger than would be expected due to changes in scattering from the motion of small defects. This indicates the presence of large-scale collective fluctuations.

Previous experiments [85] in wires of YBCO have reported a reduction in noise as the width of the wires decreases. This large size of the low-frequency fluctuators may explain the reduction of noise. Furthermore, if a narrow sample would in fact constrain and pin the fluctuations, this would lend further credence to the interpretation of fluctuating domain structure based on resistance fluctuations seen by Bonetti

et al. in YBCO nanowires [70] and discussed in §2.2.2.

We calculated the free energy difference between the states, ΔF, for the two state fluctuators from the ratio $r(T) = \tau_{\mathrm{Down}}(T)/\tau_{\mathrm{Up}}(T)$ of time spent in each state from the Boltzman expression $r(T) = exp(\Delta F/k_B T)$. The temperature derivative of ΔF then allows the calculation of the change in energy ΔU and the change in entropy $\Delta\sigma$, since $\Delta F = \Delta U - T\Delta\sigma$. Pure switching between different versions of a broken-symmetry phase should give zero for $\Delta\sigma$ and ΔU. We calculate $|\Delta\sigma|$ for two state fluctuators in three distinct samples and find typical values of $|\Delta\sigma| < 10$ (see for example the plot of the Boltzman fit to the duty cycle in Fig. 5.28(b)). Given the minimum plausible volume involved per fluctuator, as calculated above, this gives $\Delta\sigma$ less than 10^{-3} per unit cell, which would be surprisingly small for fluctuations between different phases. The value is, however, consistent with fluctuations between qualitatively similar configurations of a disordered phase.

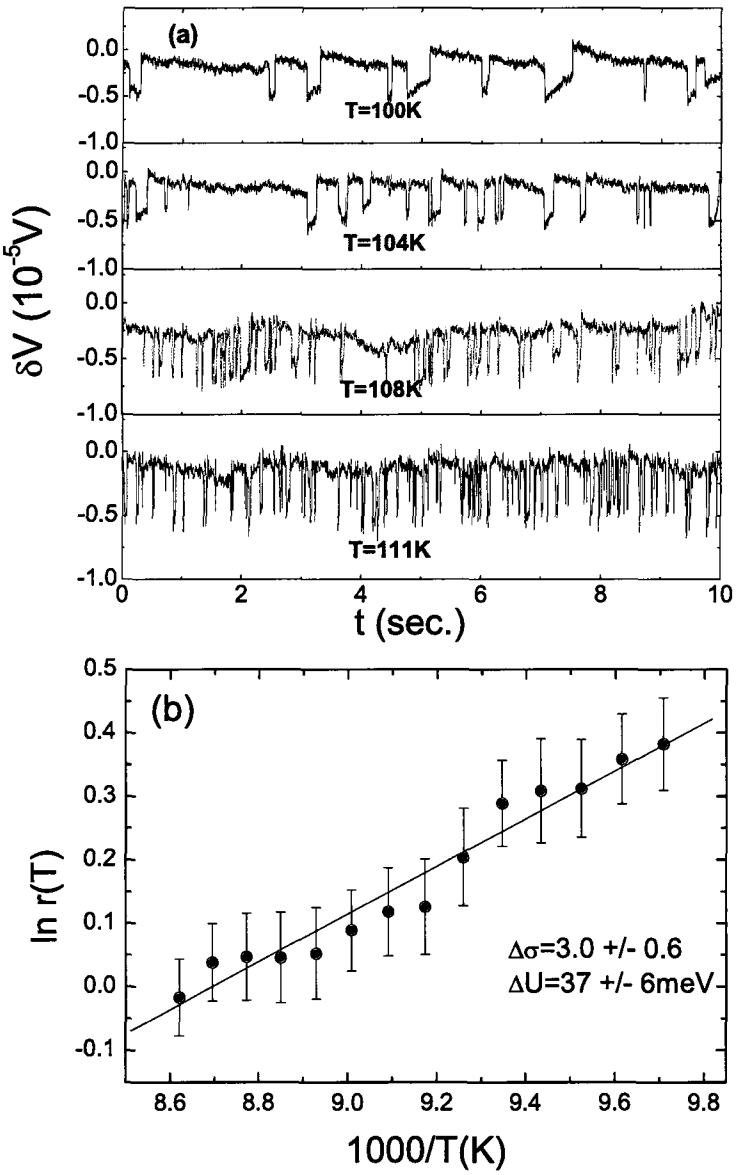

Figure 5.28: (a) Temperature dependence of the time trace of a fluctuator in a YBCO sample with T_c of 85 K. (b) Boltzman fit for duty cycle ratio.

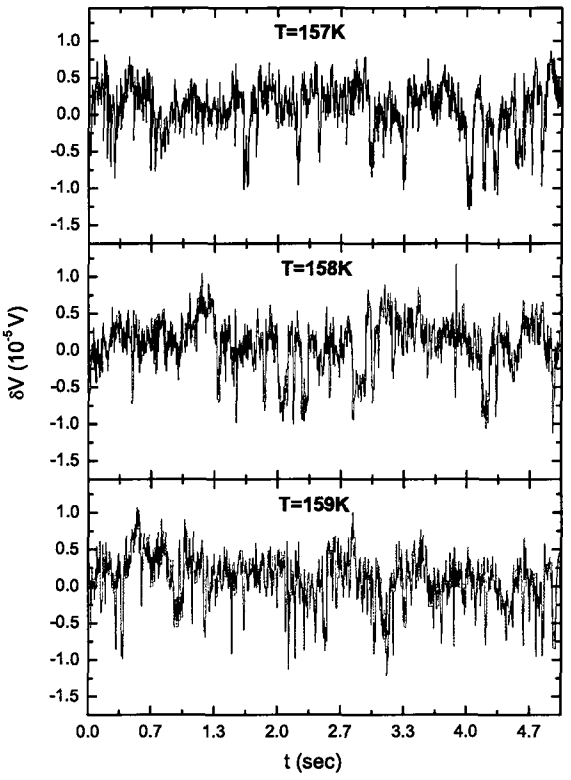

Figure 5.29: Temperature dependence of the time trace of a fluctuator in a Ca-YBCO sample with T_c of 62 K.

Chapter 6

Discussion

Individual noise measurements on their own cannot reveal a full picture about the underlying fluctuators, however the cumulation of several noise experiments and their comparison with other experimental results allow us to infer important details about the physics behind the noise that we have observed. In this chapter we attempt to make sense of the collection of results from the previous chapter and provide evidence that the extra noise source is likely due to some large-scale collective effects associated with electronic symmetry breaking in the pseudogap phase. The strongest evidence comes from the existence of large discrete fluctuators, the presence of aging effects, and the observation of magnetic sensitivity (especially to low-fields) exclusively in the noise region below approximately 230 K. This evidence, along with the results of the anisotropy measurement, allows us to make several inferences about the nature of the fluctuating order. Based on a connection with previous experiments we will also discuss how these magnetically sensitive electronic effects may be connected to oxygen diffusion.

$T_p(f)$ and the derived activation energy of 0.4 eV were nearly the same in 8 samples with T_c's ranging from 30K to 85K (with the exception of one sample from a film which showed several signs of significant inhomogeneity). Since we consistently observe that the starting temperature of the excess noise correlates with the onset of magnetic sensitivity and the change in noise spectral power, we believe that this relationship is more than coincidence. We attempt to find the cause of the relationship between this fluctuator and other observed noise characteristics by comparison with

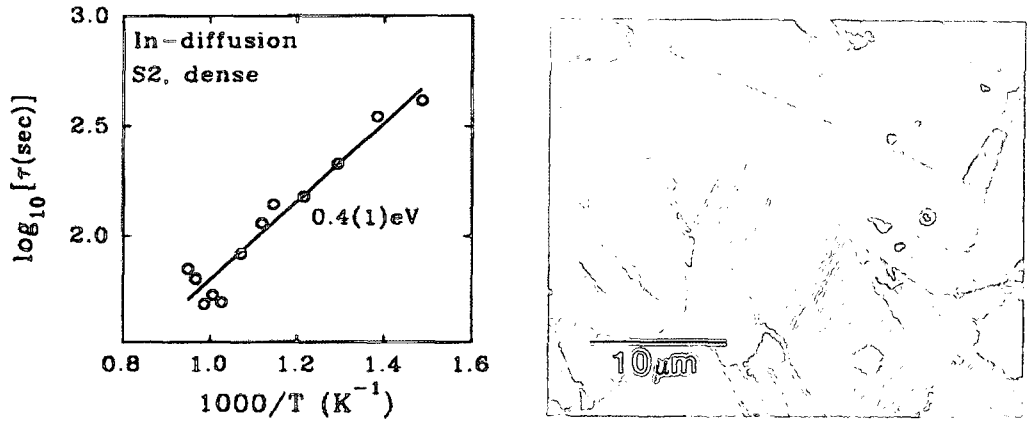

Figure 6.1: (a) Arrhenius fit of relaxation times for oxygen diffusion for temperatures 400-780°C. The lower activation energy of 0.4 eV, believed to be oxygen diffusion across large grain boundaries, is similar to the activation energy seen in noise measurements. (b)The coarse-grain polycrystalline sample which showed displayed a lower energy activation energy for oxygen diffusion [86].

other magnetic and low frequency observations in underdoped cuprates.

One other low-frequency phenomenon that has been measured in YBCO is internal friction. Internal friction is the study of internal damping of a solid. It involves driving a thin reed or wire of the material under study with an electromagnetic force. The vibrations are recorded with a tranducer, measuring the decay time after removing the driving force. The technique ultimately measures the anelastic (non-elastic dissipation) response that arises from the relaxation of defects. The connection between internal friction and transport noise arises from the fact that the same defect motions that cause stresses and strains in the material of study can also couple to scattering rate and hence the resistivity. In the case when defect motion couples both to resistance and the anelastic response, the two techniques can be complimentary. Similar to noise measurements, the magnitude of the response from internal friction measurements are dependent on frequency and temperature. However, internal friction measurements can be more limited than noise measurements; only few

frequencies can be probed since the damping is usually measured from the width of mechanical resonance. Usually, the internal friction is recorded as the inverse of the quality factor, $Q^{-1} = \Delta\omega/\omega_c$, where ω_c is the center frequency and $\Delta\omega$ is the width at half maximum. Several studies have found peaks in internal friction with thermally activated kinetics [87, 88], however the activation energies are much higher ($\sim$ 1 eV) than what we measure ($\sim$ 0.4 eV), and for a similar frequency range, the peaks occur at different temperatures. Neither the location in temperature nor the energies observed in internal friction measurements display any obvious connections to our noise results.

While the activation energy that we observe for the peak does not match the low frequency measurements in internal friction, it does agree with one measurement of the activation energy in a transport diffusion experiment. By monitoring the relaxation times from oxygen diffusion and by measuring changes in the resistance, a structurally dependent component of oxygen diffusion was found in grainy YBCO films with an activation energy of 0.4 eV [86]. This diffusion rate is proposed to be associated with extended defects, such as twin boundaries, based on the fact that it showed up predominantly in grainier polycrystalline samples and disappeared in single crystal samples. While we are unable to show exactly that the source of fluctuations in both measurements are caused by the same mechanism, the connection between our results and the structural dependent diffusion appears to be quite plausible.

One phenomenon that was observed in internal friction that appears to be analogous to our results was the temperature cycling dependence on the amplitude of friction peaks. In § 5.2.1, we described the change in the spectral noise power and abrupt loss of low-field magnetic sensitivity in two samples, patterned from the same film, after a temperature sweep. Using internal friction measurements, Cannelli *et al.* [87] noticed that there was a temperature dependent hysteresis in two internal friction peaks shown in Fig. 6.2. Their discussion attributes the hysteresis to the mo-

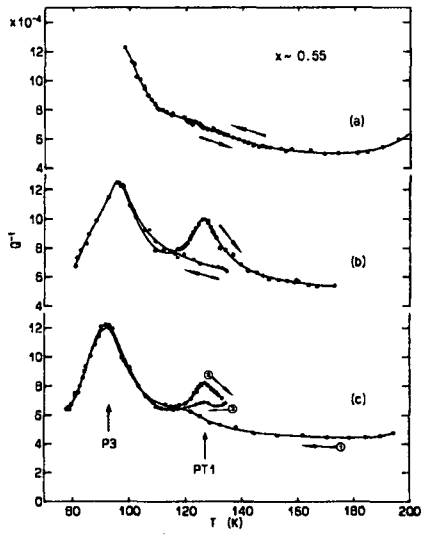

Figure 6.2: The dependence of two internal friction peaks, PT1 and PT2 on thermal cycling. (a)Thermal cycles only above 100K beginning at room temperature (b) cooling then heating on the same sample below 80K (c) cooling to below 80K from room temperature. The directions for (c) are given by (1)cooling to below 80K, (2) heating to above peak PT2, and (3) cooling back down to 80K. [87]

tion of domain walls (i.e grain boundaries or twins) which are coupled to ferroelectric order. While the relationship to ferroelectric order is highly speculative, the discussion on the formation and melting of domains may be relevant to our results. They argue that when cooling from high temperatures, at a certain temperature above 200 K, domains would begin to form. Eventually these domains would settle (or age) at low temperatures into quasi-static orientations. Upon heating, these domains reorientate themselves, eventually melting, and the motion of this reorientation would cause the anelastic peaks. This explanation, based on sluggish dynamics of spatially extended domains, seems plausible since it is difficult to imagine an alternative scenario in which locally confined defects would cause such a large hysteretic effect in the internal damping.

Since there exists a wealth of information about the doping dependent electronic properties of the pseudogap regime, it is important to compare our results to previous experimental observations. It turns out that lack of doping dependence in T_p does

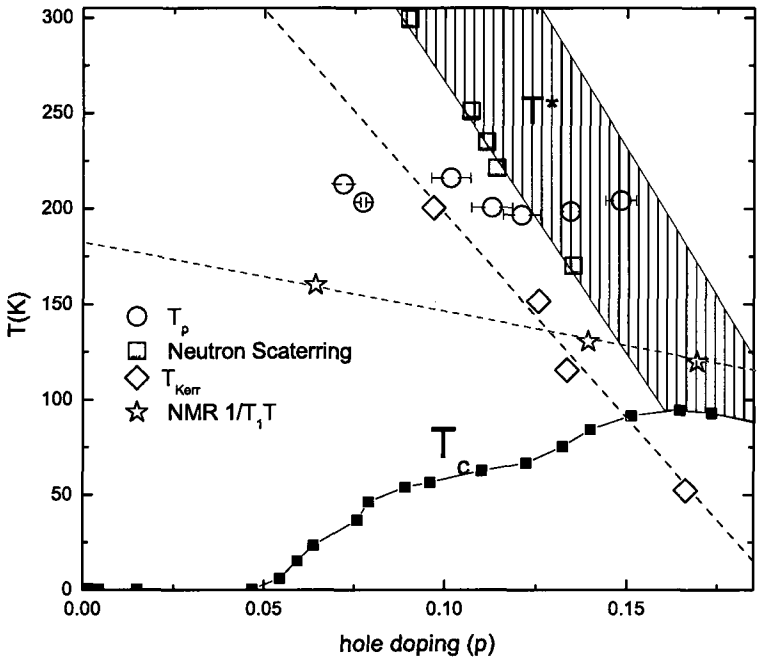

Figure 6.3: Phase diagram comparing T_p to other experimental results including the Kerr effect [91], neutron scattering [90], and NMR $1/T_1T$ data [26]. A range representing various measurements of the pseudogap temperature, T^*, is also included [33].

not match measures of the onset of electronic correlations (for example by neutron scattering, the Kerr effect and μSR, see Fig. 6.3) [89, 90, 91, 92]). Other magnetic behavior, such as the observed noise memory due to magnetic perturbations that exists after cycling up to room temperature, has been seen in other measurements. The Kerr effect, which shows up near and well below T_p [91] (shown in Fig. 6.3), also shows magnetic memory persisting at room temperature. It is possible that the transport noise could be connected with the same time-reversal symmetry-breaking which shows up via the Kerr effect since it is less likely to have two different causes of a high temperature magnetic memory effect in YBCO (especially when current understanding would predict no such effect).

Perhaps the strongest evidence of the noise being due to collective fluctuations of electronic order is the sensitivity to low-level magnetic field changes in a pair of samples. The low-field data showed a large ($> 20\%$ increase) fast response with training of the noise response; one would not expect such a large response to low fields for locally fluctuating moments. As we have already discussed in the previous chapter, the low-field response is reminiscent of glassy behavior. However, the fact that we only observed this effect in two samples (from the same film) and that the effect in low and high field noise were observed for different orientations of the field (low field noise coupled stongly to $H \perp c$, while high field noise coupled to $H \parallel c$) remains puzzling. Clearly, further study is required in order to explain these incongruities.

So far we have compared our results with other magnetic observations in the pseudogap, and low-energy excitations that occur within our frequency range. However, the connection between the magnetic sensitivity and collective structural fluctuations picked up via diffusion [86] and anelastic damping [87] are not obvious. We attempt to link these observations based on a pair of experiments performed by Yoshi Ando's research group. Lavrov *et al.* [93] used magnetic susceptibility measurements in underdoped LSCO and discovered a strong anisotropy in the in-plane susceptibility. They argue that this is due to an underlying magnetic anisotropy, such as one would expect for spin order due to stripes. In a fascinating second experiment, they apply a 14 Tesla field to twinned crystals of LSCO and discover that they are able to align twins to the extent that it appears that they are able to remove twins completely within the bulk (see Fig. 6.4). They argue that the in-plane anisotropy, due to stripes, causes the magnetic susceptibility of LSCO ($x = 0.01$) and that these are coupled or pinned to the crystal-axes thus making alignment with the magnetic field possible. This is the strongest link that shows coupling between magnetic and structural order. According to these experiments, not only are the twins coupled to the magnetic anisotropy, they are surprisingly mobile. Hence, they would have very low

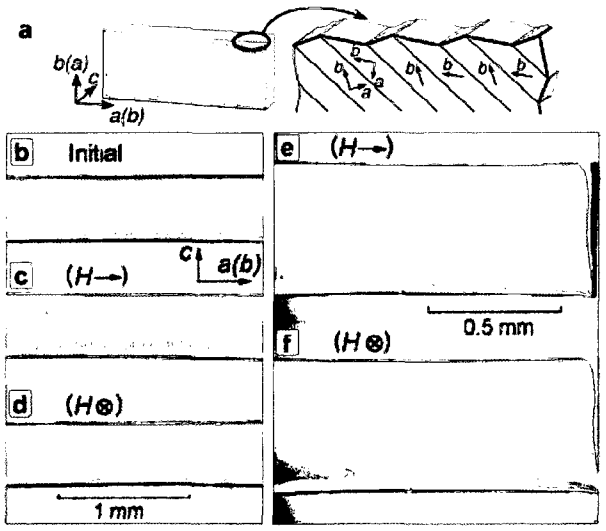

Figure 6.4: The results of a strong magnetic field aligning twins in LSCO. The effect is measured using a polarized-light microscope at room temperature. (a) Schematic of twin pattern that emerges below a temperature dependent tetragonal to orthorhombic transition. Red corresponds to the *ac* domains while blue corresponds to *bc*. (b) Twinning pattern before the application of field. The crystal initially had a larger fraction of *bc* (blue) domains. (c),(e) Application of 14 Tesla in the *ab* plane changes the domain structure favoring *ac* (red) domains. (d),(f) Application of 14 Tesla field perpendicular to *ab* plane completely removes twin boundaries, causing the crystal to be in one state aligned in the *bc* direction [94].

activation energies.

For higher doping, the magnitude of the noise peak in our experiments is far more sensitive to doping than the magnitude of the higher temperature noise, as shown in Fig. 5.12. Interestingly, the change in slope and increase of the magnitude of the higher temperature noise at low doping is in proximity to the phase transition from an orthorhombic structure to tetragonal structure. However, the exact relation between the structural change and the change in the noise could be quite complicated.

The increase in the amplitude of the noise peak as doping is decreased could be caused by two mechanisms; either there is an increase in the density of fluctuators or an increase in the coupling strength between the fluctuators and the resistance. Based on the putative connection between our noise and a collective electronic or-

der, there is strong evidence for the latter based on the work of Ando *et al.* [68] which shows that at lower doping, stripe-based transport anisotropy is largest (see Fig. 2.11). Aside from the increase in noise amplitude, we also nearly consistently see a deviation in Dutta-Horn near T_p. Furthermore, previous noise measurements have seen deviations in Dutta-Horn for YBCO [85] in the same range, near and below ~200 K , similar to where we show (see § 5.2) a significant deviation. The sign of the deviation corresponds to a gain of net noise magnitude, not just a shift of characteristic noise frequencies, as T decreases. Such an effect would be expected if the noise comes from the resistive anisotropy attributed to 'stripes' in the pseudogap regime, since that component of the anisotropy grows with decreasing temperature [68].

With respect to isotropy of fluctuations we find that the isotropy parameter gives $S \sim 0$. The slight dip in S that begins near 200 K is intriguing and may be related to the onset of the excess noise as well as all the characteristic changes that turn on near this temperature. The fact that $S \sim 0$ however, does not necessarily mean that the fluctuations are dyadic (uncorrelated); the value we measure could be due to a combination of scalar and traceless fluctuations that average out.

In the simplest picture of nematic order envisioned in [69, 70, 83] the noise is caused by rotations of the easy axis of stripe domains, giving intrinsically traceless contributions to the resistivity fluctuations. Our results show resistivity fluctuations that are far from scalar but neither are they traceless. Furthermore, the individual fluctuators show changes in scalar properties, entropy and energy, indicating that some state richer than a simple nematic is probably involved.

In summary, while noise from disordered collective states is a common phenomenon, the noise in these YBCO films is very unusual in that the onset is characterized by simple thermally activated kinetics, rather than by any sort of sharp transition or crossover. The onset temperature seems unrelated to other signatures of the onset of electronic correlations T^*, but has an activation energy suspiciously close to the

lower activation energy peak found for one oxygen diffusion process that is related to an increase in structural disorder (perhaps including twin boundaries) in YBCO [86]. These results would agree with a model in which stripe-like correlations are pinned by disorder, with the metastable states determined by many pinning sites. For a large component of the disorder that is mobile on the experimental frequency scale (i.e. fluctuating rapidly, as is expected for mobile stripes based on neutron scattering experiments), the resistance will average out over different stripe configurations. However, when nearly all the pinning sites are quasi-static and within our frequency range, one sees the expected quasi-equilibrium low-frequency resistance fluctuations that couple to the many configurations of this quenched disorder.

Our model is based on attempt to connect other experimental results that occur within the pseudogap and our results. Some of the possible directions for future inquiry, using our model as a hypothesis to be tested, will be discussed in the final chapter.

Chapter 7

Conclusions and Future Work

Using a series of electronic transport noise measurements in underdoped YBCO, we found a well defined temperature below which emerges an extra noise source with qualitatively distinct features. This low-frequency noise shows aging effects and individual fluctuators much larger than would be expected for any standard local defect noise mechanism. These features are expected for pictures in which some broken symmetry is partially pinned by disorder, giving large scale, quasi-static fluctuations. We presented a picture that links the strong dependence of the noise magnitude on doping and complicated magnetic field sensitivity with other electronic effects associated with the pseudogap observations; specifically, collective electronic fluctuations that one would expect from stripe order. While this link between resistance noise and fluctuating stripe order pinned to quasi-static domain motion is speculative, it does seem to fit the evidence that we described in the previous chapter.

Using the model developed in the previous chapter as a starting point, the future work on this project should serve as a test for this hypothesis. One of the first steps should be a systematic study of doping dependence, particulary for optimally and overdoped samples. If indeed the noise we observe is coupling to pseudogap related order, we would expect it to disappear, or at least be greatly reduced in the overdoped region. A further direction of study is to measure the noise in untwinned samples. According to our model, the stripe dynamics are pinned to sluggish dynamics of twins. Since the twins are supposed to be a large component of the disorder, in their absence, we would expect some change in the noise. We would not expect a complete loss of

low frequency stripe noise, however, since there may be other pinning sites. It would also be useful to study the noise as a function of sample dimensions, specifically by studying noise as a function of thickness and sample width. Similar to studies by Bei *et al.* [85], where they see an overall noise amplitude reduction as sample thickness is decreased, we would like to measure how each part of $S(f,T)$ scales with thickness. By measuring both above and below the onset of excess noise we could see if all or part of the temperature noise is decreasing. In order to test how universal this phenomenon is to the high-temperature superconductors, we would like to measure this noise in other cuprate materials. LBCO and LSCO would be ideal candidates. LBCO has static stripe order which may show many of the magnetic dependencies that we have seen in our noise. While LSCO does not have static stripes, it does have twin boundaries similar to YBCO and it is not unreasonable to expect similar noise features. Finally, one of the more perplexing results from our experiments is the complex magnetic sensitivity to different field orientations as well as magnetic memory effects. We would like to further characterize this magnetic behavior. In order to gain further detail about the magnetic sensitivity, we would like to perform a survey of both low and high field measurements on a variety of twinned and untwinned samples in various materials and dopings.

Appendix A

Fluctuation Isotropy Code

A.1 FreeFem++ Code for Isotropy Fluctuation Geometric Factor

```
1 //variables used to define the geometry
2 //-- solves for top left quadrant of isotropy geometry
3 // all distances are in microns
4 real dot=10; // radius of central area used in isotropy measurements
5 real rad=1.5; //radius of trenches that define pattern
6 real h0=(2*rad)/sqrt(2.) ;
7 // width of trench is 3um, left side=top side = 3/sqrt(2)
8 real h2=h0;
9 real L=50.; // length (distance out where we measure equipotential)
10 real h=L-h2; // height left side
11 real rad0=rad/sqrt(2.);
12 real b1=((dot/2.)+(rad/2.))/sqrt(2.);//
13 real diag=sqrt((L-b1-h0+rad0)*(L-b1-rad0));
14 real h1=b1+rad0; //
15
16 //defines 7 borders of space in which to create meshes
17 border a(t=0,L){x=t;y=0;}; // bottom: ..a
18 border b(t=0,L){x=L;y=t;}; // right: ..b
19 border top(t=0,h){x=L-t;y=L;}; // top
20 border d1(t=0,L-b1-h2+rad0){x=h2+t;
21     y=L+t/(L-b1-h2+rad0)*(b1+rad0-L);}; //diagonal1
22 border sc(t=pi/4,5*pi/4){x=(L-b1+rad0-h0/2)+rad*sin(t);
23     y=(b1+rad0-h0/2)+rad*cos(t);};//semi-circle
24 border d2(t=0,L-b1-h0+rad0){x=(L-b1-h0+rad0)-t;
25     y=t/(L-b1-h0+rad0)*(h-(b1+rad0-h0))+(b1+rad0-h0);}; //diagonal3
26 border d(t=h,0){x=0;y=t;}; // left: ..d
27 int n=5; // general density of meshes
28 mesh Th=buildmesh (a(10*n)+b(10*n)+top(10*n)
```

```
29     +d1(10*n)+sc(5*n)+d2(10*n)+d(10*n));
30     // builds mesh, with relative //density at each border
31
32 savemesh(Th,"Th.msh");
33 //plot(Th,ps="dTh.eps",wait=1);
34
35 fespace Vh(Th,P1); // P2 FE-space
36 Vh uh,vh, uh2, vh2; // unknown and test function.
37 problem Electro(uh,vh) = // definition of the problem
38 int2d(Th)( dx(uh)*dx(vh) + dy(uh)*dy(vh) ) // bilinear
39 + on(top,uh=1) // +1 Volt on top border
40 + on(a,uh=0); // 0 volt on bottom border
41
42 Electro; // solves the problem
43 plot(uh,ps="electroa.eps",wait=true); // plots potential
44
45 Vh Ex=dx(uh);
46 Vh Ey=dy(uh);
47 plot([Ex,Ey],ps="Efielda.eps",wait=true,fill=1,value=1);
48  // plots gradient of potential -- E field
49
50 problem Electrob(uh2,vh2) = // definition of the transverse problem
51 int2d(Th)( dx(uh2)*dx(vh2) + dy(uh2)*dy(vh2) ) // bilinear
52 + on(d,uh2=0) // 0 Volt on left
53 + on(b,uh2=1); // +1 volt on right
54
55 Electrob; // solves the problem
56 plot(uh2,ps="electrob.eps",wait=true,fill=1); //
57
58 Vh Ex2=dx(uh2);
59 Vh Ey2=dy(uh2);
60 plot([Ex2,Ey2],ps="Efieldb.eps",wait=true,fill=1,value=1);
61 // E field in transverse direction
62 // the following is the output
63 {
64   ofstream file("Potential.txt");
65   file << uh[] << endl;
66 }
67 {
68   ofstream file("Exa.txt");
69   file << Ex[] << endl;
70  }
71  {
72   ofstream file("Eya.txt");
73   file << Ey[] << endl;
```

```
74  }
75  {
76   ofstream file("Exb.txt");
77   file << Ex2[] << endl;
78  }
79  {
80   ofstream file("Eyb.txt");
81   file << Ey2[] << endl;
82  }
```

A.2 Matlab Code For Data Analysis of Isotropy Measurements

```
function y=PwBGSubtrDavid(RpA0B, R0ApB, RmA0B, R0AmB,
RpApB, RpAmB, RmAmB, RmApB, R0A0B, TrLength, SamplingRate, OutFile)


%=========================================================================
%Background Noise Statistics

s_BG=size(R0A0B);
FL_BG=s_BG(1)-1;
BG_MyDataA=reshape(R0A0B(2:s_BG(1),2:2), TrLength, FL_BG/TrLength);
BG_MyDataB=reshape(R0A0B(2:s_BG(1),3:3), TrLength, FL_BG/TrLength);

clear BGData;

Y_BGA=fft(BG_MyDataA); %FFT of the background data;
Y_BGB=fft(BG_MyDataB); %FFT of the background data;
Y_BGA=Y_BGA(1:TrLength/2,:);
Y_BGB=Y_BGB(1:TrLength/2,:);
Pyy_BGA = Y_BGA.* conj(Y_BGA)/(TrLength); %From FFT to power spectrum;
Pyy_BGB = Y_BGB.* conj(Y_BGB)/(TrLength); %From FFT to power spectrum;


clear BG_MyDataA BG_MyDataB;

k_BGA=(mean(transpose(Pyy_BGA)))'; %Calculation of average background PS
k_BGB=(mean(transpose(Pyy_BGB)))'; %Calculation of average background PS

l_bin=[4 7 13 25 49 97 193 385];  %Definition of octave lowest bin
for i=1:7
```

```
    OctSumBGA(i:i,:)=sum(Pyy_BGA(l_bin(i):l_bin(i+1)-1,:));
    OctSumBGB(i:i,:)=sum(Pyy_BGB(l_bin(i):l_bin(i+1)-1,:));
end;
OctSumBGA=OctSumBGA';
OctSumBGB=OctSumBGB';

MeanOctSumBGA=mean(OctSumBGA);
MeanOctSumBGB=mean(OctSumBGB);

clear Y_BGA Y_BGB Pyy_BGA Pyy_BGB;

Freq=SamplingRate/1024:SamplingRate/1024:SamplingRate/2;
Freq=Freq';
%=========================================================================
%Noise Statistics

sRpA0B=size(RpA0B);
sR0ApB=size(R0ApB);
sRmA0B=size(RmA0B);
sR0AmB=size(R0AmB);
sRpApB=size(RpApB);
sRpAmB=size(RpAmB);
sRmAmB=size(RmAmB);
sRmApB=size(RmApB);

%+Ia Ib=0 voltage measured accross A direction (same as current)
%+Ia Ib=0 voltage measured accross B direction
DpA0B_A=reshape(RpA0B(2:sRpA0B(1),2:2),1024,[]);
 DpA0B_B=reshape(RpA0B(2:sRpA0B(1),3:3),1024,[]);

 %Ia=0 +Ib voltage measured accross A direction
 %Ia=0 +Ib voltage measured accross B direction (same as current)
 D0ApB_A=reshape(R0ApB(2:sR0ApB(1),2:2),1024,[]);
 D0ApB_B=reshape(R0ApB(2:sR0ApB(1),3:3),1024,[]);

%-Ia Ib=0 voltage measured accross A direction (same as current)
%-Ia Ib=0 voltage measured accross B direction
DmA0B_A=reshape(RmA0B(2:sRmA0B(1),2:2),1024,[]);
DmA0B_B=reshape(RmA0B(2:sRmA0B(1),3:3),1024,[]);

%Ia=0 -Ib voltage measured accross A direction
%Ia=0 -Ib voltage measured accross B direction (same as current)
D0AmB_A=reshape(R0AmB(2:sR0AmB(1),2:2),1024,[]);
D0AmB_B=reshape(R0AmB(2:sR0AmB(1),3:3),1024,[]);
```

```
%+Ia +Ib voltage measured accross A direction
%+Ia +Ib voltage measured accross B direction
DpApB_A=reshape(RpApB(2:sRpApB(1),2:2),1024,[]);
DpApB_B=reshape(RpApB(2:sRpApB(1),3:3),1024,[]);

%+Ia -Ib voltage measured accross A direction
%+Ia -Ib voltage measured accross B direction
DpAmB_A=reshape(RpAmB(2:sRpAmB(1),2:2),1024,[]);
DpAmB_B=reshape(RpAmB(2:sRpAmB(1),3:3),1024,[]);

%-Ia -Ib voltage measured accross A direction
%-Ia -Ib voltage measured accross B direction
DmAmB_A=reshape(RmAmB(2:sRmAmB(1),2:2),1024,[]);
DmAmB_B=reshape(RmAmB(2:sRmAmB(1),3:3),1024,[]);

%-Ia +Ib voltage measured accross A direction
%-Ia +Ib voltage measured accross B direction
DmApB_A=reshape(RmApB(2:sRmApB(1),2:2),1024,[]);
DmApB_B=reshape(RmApB(2:sRmApB(1),3:3),1024,[]);


clear RpA0B R0ApB RpApB RpAmB RmAmB RmApB;


    YpA0B_A=fft(DpA0B_A);
    YpA0B_B=fft(DpA0B_B);
    Y0ApB_A=fft(D0ApB_A);
    Y0ApB_B=fft(D0ApB_B);
    YmA0B_A=fft(DmA0B_A);
    YmA0B_B=fft(DmA0B_B);
    Y0AmB_A=fft(D0AmB_A);
    Y0AmB_B=fft(D0AmB_B);
    YpApB_A=fft(DpApB_A);
    YpApB_B=fft(DpApB_B);
    YpAmB_A=fft(DpAmB_A);
    YpAmB_B=fft(DpAmB_B);
    YmAmB_A=fft(DmAmB_A);
    YmAmB_B=fft(DmAmB_B);
    YmApB_A=fft(DmApB_A);
    YmApB_B=fft(DmApB_B);

    top1_1=(real(YpApB_A.*conj(YpApB_B)))';
    top1_1=top1_1(:,1:TrLength/2)/(TrLength);
    top1_2=(real(YpAmB_A.*conj(YpAmB_B)))';
    top1_2=top1_2(:,1:TrLength/2)/(TrLength);
```

```
top1=(mean(top1_1)-mean(top1_2))/2;
top1=top1';

top2_1=(real(YpApB_A.*conj(YpApB_B)))';
top2_1=top2_1(:,1:TrLength/2)/(TrLength);
top2_2=(real(YmApB_A.*conj(YmApB_B)))';
top2_2=top2_2(:,1:TrLength/2)/(TrLength);
top2=(mean(top2_1)-mean(top2_2))/2;
top2=top2';

top3_1=(real(YmAmB_A.*conj(YmAmB_B)))';
top3_1=top3_1(:,1:TrLength/2)/(TrLength);
top3_2=(real(YpAmB_A.*conj(YpAmB_B)))';
top3_2=top3_2(:,1:TrLength/2)/(TrLength);
top3=(mean(top3_1)-mean(top3_2))/2;
top3=top3';

top4_1=(real(YmAmB_A.*conj(YmAmB_B)))';
top4_1=top4_1(:,1:TrLength/2)/(TrLength);
top4_2=(real(YmApB_A.*conj(YmApB_B)))';
top4_2=top4_2(:,1:TrLength/2)/(TrLength);
top4=(mean(top4_1)-mean(top4_2))/2;
top4=top4';

for i=1:7
    OStop1(i:i)=sum(top1(l_bin(i):l_bin(i+1)-1));
    OStop2(i:i)=sum(top2(l_bin(i):l_bin(i+1)-1));
    OStop3(i:i)=sum(top3(l_bin(i):l_bin(i+1)-1));
    OStop4(i:i)=sum(top4(l_bin(i):l_bin(i+1)-1));
end;


OSav_top=(OStop1+OStop2+OStop3+OStop4)/4;
OSav_top=OSav_top';

PYYpA0B_B=YpA0B_B.*conj(YpA0B_B);
PYYpA0B_B=PYYpA0B_B(1:TrLength/2,:)/(TrLength);
PYY0ApB_A=Y0ApB_A.*conj(Y0ApB_A);
PYY0ApB_A=PYY0ApB_A(1:TrLength/2,:)/(TrLength);
PYYmA0B_B=YmA0B_B.*conj(YmA0B_B);
PYYmA0B_B=PYYmA0B_B(1:TrLength/2,:)/(TrLength);
PYY0AmB_A=Y0AmB_A.*conj(Y0AmB_A);
PYY0AmB_A=PYY0AmB_A(1:TrLength/2,:)/(TrLength);

for i=1:7
```

```
OSbottom1(i:i,:)=sum(PYYpA0B_B(l_bin(i):l_bin(i+1)-1,:))-MeanOctSumBGB(i:i);
OSbottom2(i:i,:)=sum(PYY0ApB_A(l_bin(i):l_bin(i+1)-1,:))-MeanOctSumBGA(i:i);
OSbottom3(i:i,:)=sum(PYYmA0B_B(l_bin(i):l_bin(i+1)-1,:))-MeanOctSumBGB(i:i);
OSbottom4(i:i,:)=sum(PYY0AmB_A(l_bin(i):l_bin(i+1)-1,:))-MeanOctSumBGA(i:i);
    end;

    OSbottom1=OSbottom1';
    check=OSbottom1;
    MOSbottom1=(mean(OSbottom1))';
    OSbottom2=OSbottom2';
    MOSbottom2=(mean(OSbottom2))';
    OSbottom3=OSbottom3';
    MOSbottom3=(mean(OSbottom3))';
    OSbottom4=OSbottom4';
    MOSbottom4=(mean(OSbottom4))';

    OSav_bottom=(MOSbottom1+MOSbottom2+MOSbottom3+MOSbottom4)/4;
    %OSav_bottomN=sqrt(MOSbottom1.*MOSbottom2);

    AvRatio=OSav_top./OSav_bottom;
    %AvRatioN=OSav_top./OSav_bottomN;
    AvQ=AvRatio-1;
    %AvQN=AvRatioN-1;
    G=1.11;
    S=((AvQ-1)*(3+G))./((3*G-AvQ+1+AvQ*G));
    %SN=((AvQN-1)*(3+G))./((3*G-AvQN+1+AvQN*G));
    PYYpA0B_A=YpA0B_A.*conj(YpA0B_A);
    PYYpA0B_A=PYYpA0B_A(1:TrLength/2,:)/(TrLength);
    PYY0ApB_B=Y0ApB_B.*conj(Y0ApB_B);
    PYY0ApB_B=PYY0ApB_B(1:TrLength/2,:)/(TrLength);
    PYYmA0B_A=YmA0B_A.*conj(YmA0B_A);
    PYYmA0B_A=PYYmA0B_A(1:TrLength/2,:)/(TrLength);
    PYY0AmB_B=Y0AmB_B.*conj(Y0AmB_B);
    PYY0AmB_B=PYY0AmB_B(1:TrLength/2,:)/(TrLength);

    for i=1:7
OSAAp(i:i,:)=sum(PYYpA0B_A(l_bin(i):l_bin(i+1)-1,:))-MeanOctSumBGA(i:i);
OSwBGAAp(i:i,:)=sum(PYYpA0B_A(l_bin(i):l_bin(i+1)-1,:));
OSBBp(i:i,:)=sum(PYY0ApB_B(l_bin(i):l_bin(i+1)-1,:))-MeanOctSumBGB(i:i);
OSwBGBBp(i:i,:)=sum(PYY0ApB_B(l_bin(i):l_bin(i+1)-1,:));
OSAAm(i:i,:)=sum(PYYmA0B_A(l_bin(i):l_bin(i+1)-1,:))-MeanOctSumBGA(i:i);
OSwBGAAm(i:i,:)=sum(PYYmA0B_A(l_bin(i):l_bin(i+1)-1,:));
OSBBm(i:i,:)=sum(PYY0AmB_B(l_bin(i):l_bin(i+1)-1,:))-MeanOctSumBGB(i:i);
OSwBGBBm(i:i,:)=sum(PYY0AmB_B(l_bin(i):l_bin(i+1)-1,:));
    end;
```

```
OSAAp=OSAAp';
OSBBp=OSBBp';
OSwBGAAp=OSwBGAAp';
OSwBGBBp=OSwBGBBp';
OSAAm=OSAAm';
OSBBm=OSBBm';
OSwBGAAm=OSwBGAAm';
OSwBGBBm=OSwBGBBm';



sOSAAp=size(OSAAp);
sOSBBp=size(OSBBp);
sOSAAm=size(OSAAm);
sOSBBm=size(OSBBm);

%OctSumMAA=OctSumAA';
%OctSumMBB=OctSumBB';

FreqT=Freq(l_bin);
AvFreq=sqrt(FreqT(1:7).*FreqT(2:8));
fx=(log(AvFreq));
AlphaDataAAp=(OSAAp(:,2:6))';
AlphaDataBBp=(OSBBp(:,2:6))';
AlphaDataAAp=log(AlphaDataAAp);
AlphaDataBBp=log(AlphaDataBBp);
AlphaDataAAm=(OSAAm(:,2:6))';
AlphaDataBBm=(OSBBm(:,2:6))';
AlphaDataAAm=log(AlphaDataAAm);
AlphaDataBBm=log(AlphaDataBBm);


for i=1:sOSAAp(1)
    pAAp=polyfit(fx(2:6),AlphaDataAAp(:,i:i),1);
    alphaAAp(i)=pAAp(1);
end;

for i=1:sOSBBp(1)
    pBBp=polyfit(fx(2:6),AlphaDataBBp(:,i:i),1);
    alphaBBp(i)=pBBp(1);
end;

for i=1:sOSAAm(1)
    pAAm=polyfit(fx(2:6),AlphaDataAAm(:,i:i),1);
```

```
    alphaAAm(i)=pAAm(1);
end;

for i=1:sOSBBm(1)
    pBBm=polyfit(fx(2:6),AlphaDataBBm(:,i:i),1);
    alphaBBm(i)=pBBm(1);
end;
alphaAAp=alphaAAp';
alphaBBp=alphaBBp';
alphaAAm=alphaAAm';
alphaBBm=alphaBBm';

OSAA=(OSAAp+OSAAm)/2;
% OSAA=OSAAp;
OSBB=(OSBBp+OSBBm)/2;

resAA(:,1:sOSAAp(2))=OSAA;
resAA(:,sOSAAp(2)+2:2*sOSAAp(2)+1)=OSAAp;
resAA(:,2*sOSAAp(2)+2:2*sOSAAp(2)+2)=alphaAAp;

resBB(:,1:sOSBBp(2))=OSBB;
resBB(:,sOSBBp(2)+2:2*sOSBBp(2)+1)=OSBBp;
resBB(:,2*sOSBBp(2)+2:2*sOSBBp(2)+2)=alphaBBp;



Av(:,1:1)=AvFreq;
Av(:,2:2)=(mean(OSAA))';
Av(:,3:3)=(mean(OSAAp))';
Av(:,4:4)=(mean(OSAAm))';
Av(:,6:6)=(mean(OSBB))';
Av(:,7:7)=(mean(OSBBp))';
Av(:,8:8)=(mean(OSBBm))';
Av(:,10:10)=MOSbottom1;
Av(:,11:11)=MOSbottom2;
Av(:,12:12)=MOSbottom3;
Av(:,13:13)=MOSbottom4;

BGAll(:,2:2)=k_BGA;
BGAll(:,3:3)=k_BGB;
BGAll(1:7,4:4)=AvFreq;
BGAll(1:7,5:5)=MeanOctSumBGA;
BGAll(1:7,6:6)=MeanOctSumBGB;

topp(:,1:1)=OStop1';
```

```
topp(:,2:2)=OStop2';
topp(:,3:3)=OStop3';
topp(:,4:4)=OStop4';
topp(:,5:5)=OSav_top;

bot(:,1:1)=MOSbottom1;
bot(:,2:2)=MOSbottom2;
bot(:,3:3)=MOSbottom3;
bot(:,4:4)=MOSbottom4;
bot(:,5:5)=OSav_bottom;
%bot(:,4:4)=OSav_bottomN;


SM(:,1:1)=S;
%SM(:,2:2)=SN;


path1=strcat('C:\data\analysis\',OutFile,'NA_A.dat');
path2=strcat('C:\data\analysis\',OutFile,'NA_B.dat');
path3=strcat('C:\data\analysis\',OutFile,'Av_ALL.dat');
path4=strcat('C:\data\analysis\',OutFile,'BGALL.dat');
path5=strcat('C:\data\analysis\',OutFile,'NABGA.dat');
path6=strcat('C:\data\analysis\',OutFile,'NABGB.dat');
path7=strcat('C:\data\analysis\',OutFile,'top.dat');
path8=strcat('C:\data\analysis\',OutFile,'bot.dat');
path9=strcat('C:\data\analysis\',OutFile,'S.dat');
path10=strcat('C:\data\analysis\',OutFile,'check.dat');

save (path1, 'resAA', '-ASCII', '-TABS');
save (path2, 'resBB', '-ASCII', '-TABS');
save (path3, 'Av', '-ASCII', '-TABS');
save (path4, 'BGAll', '-ASCII', '-TABS');
save (path5, 'OctSumBGA', '-ASCII', '-TABS');
save (path6, 'OctSumBGB', '-ASCII', '-TABS');
save (path7, 'topp', '-ASCII', '-TABS');
save (path8, 'bot', '-ASCII', '-TABS');
save (path9, 'SM', '-ASCII', '-TABS');
save (path10, 'check', '-ASCII', '-TABS');


clear all;
```

References

[1] K. Onnes, Commun. Phys. Lab. Univ. Leiden **124c**, 1 (1911).

[2] W. Meissner and R. Ochsenfeld, Naturwissenschaften **21**, 787 (1933).

[3] J. Bardeen, L. N. Cooper, and J. R. Schrieffer, Physical Review **106**, 162 (1957).

[4] J. Bardeen, L. N. Cooper, and J. R. Schrieffer, Physical Review **108**, 1175 (1957).

[5] W. L. McMillan, Physical Review **167**, 331 (1968).

[6] J. G. Bednorz *et al.*, Z. Phys. **64**, 189 (1986).

[7] J. D. Jorgensen *et al.*, Physica C **153-155**, 578 (1990).

[8] J. Waldram, *Superconductivity of Metals and Cuprates* (IOP Publishing Ltd., Bristol, 1996).

[9] J. R. Kirtley *et al.*, Nature Physics **2**, 190 (2006).

[10] S. W. Tozer *et al.*, Phys. Rev. Lett. **59**, 1768 (1987).

[11] N. F. Mott, Proc. Phys. Soc., London, Sect. A **62**, 416 (1949).

[12] D. Vaknin *et al.*, Phys. Rev. Lett. **58**, 2802 (1987).

[13] P. A. Lee, N. Nagaosa, and X. Wen, Rev. Mod. Phys. **78**, 17 (2006).

[14] M. Vojta, arXiv: 0901.3145 [cond-mat.supr-con] (2009).

[15] A. Damascelli, Z. Hussain, and Z. X. Shen, Rev. Mod. Phys. **75**, 473 (2003).

[16] G. Xiao *et al.*, Nature **332**, 238 (1988).

[17] D. J. C. Walker *et al.*, Phys. Rev. B **51**, 9375 (1995).

[18] T. R. Chien, Z. Z. Wang, and N. P. Ong, Phys. Rev. Lett. **67**, 2088 (1991).

[19] C. E. Gough *et al.*, Nature **326**, 855 (1987).

[20] D. A. Wollman *et al.*, Phys. Rev. Lett. **71**, 2134 (1993).

[21] C. C. Tsuei *et al.*, Phys. Rev. Lett. **73**, 593 (1994).

[22] O. Fischer *et al.*, Rev. Mod. Phys. **79**, 353 (2007).

[23] W. W. Warren *et al.*, Phys. Rev. Lett. **62**, 1193 (1989).

[24] R. E. Walstedt *et al.*, Phys. Rev. B **41**, 9574 (1990).

[25] M.-H. Julien *et al.*, Phys. Rev. Lett. **76**, 4238 (1996).

[26] P. Carretta, Physica C: Superconductivity **292**, 286 (1997).

[27] Y. Ando *et al.*, Phys. Rev. Lett. **93**, 267001 (2004).

[28] A. P. Mackenzie, S. R. Julian, D. C. Sinclair, and C. T. Lin, Phys. Rev. B **53**, 5848 (1996).

[29] T. R. Thurston *et al.*, Phys. Rev. B **40**, 4585 (1989).

[30] J. W. Loram, K. A. Mirza, J. R. Cooper, and W. Y. Liang, Phys. Rev. Lett. **71**, 1740 (1993).

[31] X. K. Chen *et al.*, Phys. Rev. B **56**, R513 (1997).

[32] A. Loeser *et al.*, Science **273**, 325 (1996).

[33] T. Timusk and B. Statt, Rep. Prog. Phys. **62**, 61 (1999).

[34] P. W. Anderson, Science **235**, 1196 (1987).

[35] V. J. Emery, S. A. Kivelson, and O. Zachar, Phys. Rev. B **56**, 6120 (1997).

[36] M. Randeria, N. Trivedi, A. Moreo, and R. T. Scalettar, Phys. Rev. Lett. **69**, 2001 (1992).

[37] A. Paramekanti, M. Randeria, and N. Trivedi, Phys. Rev. Lett. **87**, 217002 (2001).

[38] S. A. Kivelson *et al.*, Rev. Mod. Phys. **75**, 1201 (2003).

[39] M. Norman *et al.*, Nature **392**, 157 (1998).

[40] M. R. Norman, D. Pines, and C. Kallin, Adv. Phys. **54**, 715 (2005).

[41] Z. A. Xu *et al.*, Nature **406**, 486 (2000).

[42] K. Behnia, J. Phys.: Condens. Matter **21**, 113101 (2009).

[43] C. M. Varma, Phys. Rev. B **55**, 14554 (1997).

[44] S. Chakravarty, R. B. Laughlin, D. K. Morr, and C. Nayak, Phys. Rev. B **63**, 094503 (2001).

[45] A. J. Millis, Science **314**, 1888 (2006).

[46] T. Valla *et al.*, Science **314**, 1914 (2006).

[47] K. Tanaka *et al.*, Science **314**, 1910 (2006).

[48] M. L. Tacon *et al.*, Nature Physics **2**, 537 (2006).

[49] M. C. Boyer *et al.*, Nature Physics **3**, 802 (2007).

[50] K. Chatterjee *et al.*, Nature Physics **4**, 108 (2008).

[51] J. Zaanen, Science **286**, 251 (1999).

[52] E. Dagotto and T. M. Rice, Science **271**, 618 (1996).

[53] J. M. Tranquada *et al.*, Nature **375**, 561 (1995).

[54] J. M. Tranquada *et al.*, Phys. Rev. B **54**, 7489 (1996).

[55] P. Abbamonte *et al.*, Nature Phys. **1**, 155 (2005).

[56] J. M. Tranquada, in *Handbook of High-Temperature Superconductivity: Theory and Experiment*, edited by J. R. Schrieffer and J. S. Brooks (Springer, Amsterdam, 2007), Chap. 6.

[57] H. A. Mook *et al.*, Nature **395**, 580 (1998).

[58] S. M. Hayden *et al.*, Nature **429**, 531 (2004).

[59] J. M. Tranquada *et al.*, Nature **429**, 534 (2004).

[60] V. Hinkov *et al.*, Nature **430**, 650 (2004).

[61] V. Hinkov *et al.*, Nature Phys. **3**, 780 (2007).

[62] V. Hinkov *et al.*, Science **319**, 597 (2008).

[63] S. A. Kivelson, E. Fradkin, and V. J. Emery, Nature **393**, 550 (1998).

[64] J. E. Hoffman *et al.*, Science **295**, 466 (2002).

[65] M. Vershinin *et al.*, Science **303**, 1995 (2004).

[66] K. McElroy *et al.*, Nature **422**, 592 (2003).

[67] C. Howald *et al.*, Phys. Rev. B **67**, 014533 (2003).

[68] Y. Ando, K. Segawa, S. Komiya, and A. N. Lavrov, Phys. Rev. Lett **88**, 137005 (2002).

[69] J. A. Bonetti, Ph.D. thesis, UIUC, 2002.

[70] J. A. Bonetti, D. S. Caplan, D. J. Van Harlingen, and M. B. Weissman, Phys. Rev. Lett. **93**, 087002 (2004).

[71] H. A. Mook, P. Dai, and F. Doğan, Phys. Rev. Lett. **88**, 097004 (2002).

[72] B. Lake *et al.*, Nature **415**, 299 (2002).

[73] J. H. Scofield, J. V. Mantese, and W. W. Webb, Phys. Rev. B **34**, 723 (1986).

[74] N. E. Israeloff *et al.*, Phys. Rev. Lett. **60**, 152 (1988).

[75] R. P. Michel *et al.*, Phys. Rev. B **44**, 7413 (1991).

[76] P. Dutta and P. M. Horn, Rev. Mod. Phys. **53**, 497 (1981).

[77] M. B. Weissman, Rev. Mod. Phys. **60**, 537 (1988).

[78] R. D. Black, W. M. Snow, and M. B. Weissman, Phys. Rev. B **25**, 2955 (1982).

[79] M. B. Weissman, R. D. Black, and W. M. Snow, J. App. Phys. **53**, 6276 (1982).

[80] R. D. Black, Ph.D. thesis, UIUC, 1984.

[81] M. Rajeswari *et al.*, Journal of Superconductivity **9**, 307 (1996).

[82] D. S. Caplan *et al.*, To be submitted (2009).

[83] E. W. Carlson, K. A. Dahmen, E. Fradkin, and S. A. Kivelson, Phys. Rev. Lett. **96**, 097003 (2006).

[84] A. A. Abrikosov, Physica C **222**, 191 (1994).

[85] Y. Bei *et al.*, Phys. Rev. B **61**, 1495 (2000).

[86] J. R. LaGraff and D. A. Payne, Phys. Rev. B **47**, 3380 (1993).

[87] G. Cannelli *et al.*, Phys. Rev. B **45**, 931 (1992).

[88] G. Zheng and J. Zhang, Supercond. Sci. Technol. **15**, 1398 (2002).

[89] B. Fauqué *et al.*, Phys. Rev. Lett. **96**, 197001 (2006).

[90] H. A. Mook *et al.*, Phys. Rev. B **78**, 020506 (2008).

[91] J. Xia *et al.*, Phys. Rev. Lett. **100**, 127002 (2008).

[92] J. E. Sonier *et al.*, arXiv:0906.1584v1 [cond-mat.supr-con] (2009).

[93] A. N. Lavrov, Y. Ando, S. Komiya, and I. Tsukada, Phys. Rev. Lett. **87**, 017007 (2001).

[94] A. N. Lavrov, S. Komiya, and Y. Ando, Nature **418**, 385 (2001).

Author's Biography

David S. Caplan was born in Toronto, Ontario and raised in Hamilton, Ontario. He graduated from the University of British Columbia in 2002 with a B.Sc. in Honours Physics and a minor in English Literature. Part of his undergraduate career was completed while on exchange at the Universita Degli Studi Dell'Aquila, in L'Aquila, Italy.

As an undergraduate, David worked in a variety of physics research laboratories. In the summer of 1999 he developed beam-line models for a muon decay experiment supervised by Dr. Mike Hasinoff at TRIUMF (Tri-University Meson Facility) in Vancouver, Canada. In 2000 he worked with Dr. Aephraim Steinberg at the laser cooling and quantum optics lab at the University of Toronto. The subsequent summer he helped in the set-up of Dr. Jan Kycias low temperature lab at the University of Waterloo.

In the fall of 2002, David began his graduate studies at the University of Illinois at Urbana-Champaign where in 2005 he earned an M.S. in Physics and in 2007 he earned an M.S. in Finance. David joined the Dale Van Harlingen research group at the University of Illinois at Urbana-Champaign in beginning of 2003 when he began to study transport noise in underdoped high temperature superconductors.